# Anexo A. Artículo aceptado con cambios referente a la gestión de microrredes inteligentes

*Applied Energy (2010): APEN-S-1000048*

# Intelligent Microgrid Scheduling Controlled by Virtual Power Producer for Laboratory Purposes

H.M. Khodr [a] *, J.P. Soares[a], H. Morais[a], N. El Halabi[b], M. García-Gracia[b], Zita A. Vale[a], and Carlos Ramos[a]

[a] *GECAD – Knowledge Engineering and Decision-Support Research Center of the Polytechnic Institute of Porto (ISEP/IPP), Rua Dr. António Bernardino de Almeida 431, 4200-072 Porto, Portugal*

[b] *CIRCE, Research Center of Consumption and Energy Resource, C/Maria de Luna 3, 50018, Zaragoza, Spain*

## Abstract

In the energy management of the operation of a small power system, the scheduling of the generation units is a crucial problem. Applying right timing can maximize the performance of the energy supply. In this paper the optimal operation of a wind turbine, a solar unit, a fuel cell and a storage battery problem is formulated as a mixed-integer linear programming model (MILP) and solved by a deterministic optimization technique CPLEX-based implemented in General Algebraic Modeling Systems (GAMS). This problem has also been solved by two meta-heuristics optimization techniques that are the Genetic Algorithm (GA) and Evolutionary Particle Swarm Optimization (EPSO) for comparison purpose.

A Virtual Power Producer (VPP) can optimally operate the generation units, assuring the best functioning of equipments taking into account the maintenance, operation and the generation measurement and control. A central control at the power system allows a VPP to manage the optimal generation and their load control considering all the involved costs. The application of methodology to a real case study of the laboratory equipments, demonstrates the effectiveness of this method to solve the optimal dispatch of the DC microgrid. The problem has been solved satisfactorily by three optimization techniques demonstrating the robustness of the proposed model.

***Keywords***: Optimization techniques, Renewable energy park, Scheduling, Virtual power producer, Microgrids.

## Nomenclature

| | |
|---|---|
| $C_W$ | Wind energy cost coefficient (Eur/kWh) |
| $C_{Pv}$ | Photovoltaic energy cost coefficient (Eur/kWh) |
| $C_{Fc}$ | Fuel Cell energy cost coefficient (Eur/kWh) |
| $C_{Sc}$ | Battery charge energy cost coefficient (Eur/kWh) |
| $C_{Sd}$ | Battery discharge energy cost coefficient (Eur/kWh) |
| $C_{Ue}$ | Undelivered energy cost coefficient (Eur/kWh) |
| $C_{Ege}$ | Excess generated energy cost coefficient (Eur/kWh) |
| $P_W$ | Wind power generated (kW) |
| $P_v$ | Photovoltaic power generated (kW) |
| $P_{Fc}$ | Fuel cell power generated (kW) |
| $P_{Sc}$ | Storage battery power charge (kW) |
| $P_{Sd}$ | Storage battery power discharge (kW) |
| $P_{Ue}$ | Undelivered power (kW) |
| $P_{Ege}$ | Excess generated power (kW) |

* Corresponding author: H. M. Khodr is with GECAD – Knowledge Engineering and Decision-Support Research Center of the Polytechnic Institute of Porto (ISEP/IPP), Rua Dr. António Bernardino de Almeida, 431, 4200-072 Porto, Portugal.
E-mail: hmk@isep.ipp.pt

| | |
|---|---|
| $Load$ | Load power (kW) |
| $t$ | Time slice (hour) |
| $X$ | Binary variable corresponding to battery charging |
| $Y$ | Binary variable corresponding to battery discharging |
| $Ps$ | Storage battery power state |
| $P_{wmax}$ | Wind power generation capacity limit |
| $P_{vmax}$ | Photovoltaic generation capacity power limit |
| $\tau$ | Learning parameter |
| $w_i+1$ | Strategic parameters of particle $i$ |
| $b_i$ | Best point found by particle i in its past life |
| $bG$ | Best overall found by the swarm of particles |
| $X_i$ | Location of particle $i$ at current generation |
| $v_i$ | Velocity of particle $i$ for the next movement |
| $X_{i+1}$ | Location of particle $i$ after movement |
| $w_i.inertia$ | Particle Inertia term |
| $w_i.memory$ | Particle Memory term |
| $w_i.coop$ | Particle Cooperation or information exchange term |

## 1. Introduction

The last years have seen a huge reorganization of the traditional distribution networks towards active networks characterized by a high penetration of Distributed Generation (DG) units, based on technologies such as internal combustion engines, small and micro gas turbines, fuel cells, photovoltaic and wind plants.

The European Community indeed is promoting different initiatives to support the research in this field with a specific platform [1] and different calls within the FP7 framework program. The interest in these systems is motivated by the possibility to implement, on a large scale renewable energy, sources to limit green house gas emissions, also to reduce the transmission and distribution active power losses, and to delay or even prevent the construction of new energy infrastructures. The coordination of all these generating and loading units is a challenging issue that demands distributed intelligence which is referred to Smart Grids. In literature, few articles proposed operational solutions for microgrids because interdisciplinary knowledge is requiered.

In [2], an optimization algorithm able to individuate the subdivision of a given distribution network into an optimized number of sustainable microgrid is proposed. The method provides the best configuration of microgrids in an existing distribution system: the optimal arrangement is the one that maximizes the sum of the savings in both the cost of energy purchasing and the cost of service interruptions.

In [3], a control strategy for inverters based on DGs and a protection scheme are carried out and the coordination between them is proposed to control both voltage and frequency during islanded operation.

In [4] the issue of the autonomous control of microgrids is treated. Finally, in [5] several schemes for sharing power between generators in microgrids are compared and the minimization of fuel use in a microgrid with a variety of power sources is then discussed.

Keeping the balance between load and generation is the basic rule of all power systems. In the autonomous supply systems, as spacecrafts, airplanes or small islands, the critical amount of fuel and specific schedule of the generation capability give the scheduling problem special importance.

In the power system the daily load curve can be well forecasted. The forecast could be based on statistical, analytical or technological models. Any power system contains several elements that can be characterized as

follows:

- Load–The power system contains controlled and uncontrolled loads. The time curve can be well forecasted.
- Generator–The generators have many constraints that are minimal/maximal capacity limit, fuel amount consumption (total generated energy) and speedup ratio.
- Storage–A large amount of electricity cannot be stored economically. Only small systems use super capacitors and batteries, the greater systems contain pumped water storage, pressurized air, hydrogen generator, etc. The storage units have double characteristics: these are loads with limited capabilities, and later they may turn into generators. Due to the losses of transformation, the storage would never reaches 100% of efficiency.

Nowadays there is an upward tendency for using small isolated power systems, against central power producing system when regarding rural and distant places.

In this type of system the most important producers are the renewable energy sources (e.g, photovoltaic panels (PV), fuel cells, wind turbine etc.) in combination with diesel generators. These small power producing networks need a distributed and autonomous generation control.

Interest in small isolated power systems is also attractive for power utility companies; since they can help improving the power quality and power supply flexibility. Also, they can provide spinning reserve and reduce the transmission and distribution costs, and can be used to feed the customers in the event of an outage in the primary substation [6].

This paper deals with an optimal management of a microgrid working under isolated conditions and controlled by VPP for Laboratory purpose. This control can be handled via Internet (IP), where the microgrid becomes intelligent grid. However, it may be connected to the power distribution grid. The problem described is managed hour by hour by the microgrid central controller located at one of the generation buses. This problem is formulated as a mixed-integer linear programming model and solved by a deterministic optimization technique based on CPLEX [7], implemented in General Algebraic Modeling Systems (GAMS) [7], and it has been also solved by two meta-heuristic optimization techniques that are the Genetic Algorithm (GA) and Evolutionary Particle Swarm Optimization (EPSO) for comparison of results purpose point of view.

This paper is organized as follows: Section 2 deals with the Virtual Power Producer and its operation. In Section 3 the real case of Microgrid Laboratory is presented with convenient details. Section 4 presents the mathematical formulation of the problem under study. Section 5 explains all the optimization method used to solve the problem. Section 6 presents the Test Case and the discussion of the obtained results. Finally, in Section 7 the conclusions are duly drawn.

## 2. Virtual Power Producer Operation

The aggregation of DG plants leads to a new concept: the Virtual Power Producer (VPP). VPPs are multi-technology and multi-site heterogeneous entities. In the scope of a VPP, producers can assure that their generators are optimally operated. At the same time, VPPs will be able to achieve a more robust generation profile, raising the value of non-dispatched generation technologies [8].

The VPP can also operate in isolated networks. In this type of installation the VPP can handle the system management and equipment functioning responsibility. VPP can reduce maintenance and operation costs of the isolated system and increase its efficiency. The system management is made remotely, providing the possibility of controlling the aggregated producer's generation that is connected to the network and at the same time all the

isolated power system (generation and consumption). It is possible to manage several isolated grids at the same time. This type of management has many particular specifications, involving some adjustments to the VPP. One of the differences is the aggregation goal. The "normal" VPP has as primary goal of combining the generation of aggregated producers to sell the biggest quantity of energy in the market, to remunerate the producers and to get its own profits. When VPP is managing isolated grids the most important goal is to deliver the necessary energy to assure the optimal function of loads. Therefore, it is necessary to manage the reserves and operation of controllable generation units (fuel cells and micro turbines).

Other important aspect that VPP has to consider in the isolated microgrid operation is the need to control the generation and the consumption. Since system is isolated, sometimes, VPP has to disconnect some loads to maintain the system balance when the generation is not enough. The VPP can develop Demand Response (DR) strategies to advise the users about a wrong electric energy usage or simply overload.

In isolated microgrid operation mode, the VPP has control of all the system, therefore it gots voltage and frequency control methods and mechanisms that permit to adjust these parameters to obtain an adequate quality service to the consumers demands.

The existence of many isolated grids, that are geographically near and that are managed by the same VPP, can provide an interconnection of these systems which increase resources, dimension and stability for all systems.

The associated costs of these interconnections are proportional to the distance between grids, being an important restrain to this type of application. These interactions have to be done at Low Voltage level (LV) to maintain a good voltage level and to reduce the distribution active power losses.

## 3. Laboratory Equipment

In the Microgrid Laboratory exists a small renewable system that integrates a wind turbine, photovoltaic panels and a fuel cell. The test system is implemented at the roof, see Figure1.

Fig. 1. Microgrid Laboratory renewable system

The equipments of generation are similar to [9] with the following characteristics:

- Photovoltaic panel(s) - type: DS 40; Nominal power: 40W; Expected production of 4 panels 150 W peak
- Wind turbine - type: Air-X 401; Nominal power: 400 W at 11.5 m/s; Daily production (day and night) approx. 800Wh
- Fuel cell - type: Flexiva; Nominal power: 80 W
- Load - Practically lighting bulbs; Nominal power: 20 – 100 W (controllable)
- Storage - Storage maximum charging capacity: 200 W; Storage maximal discharging capacity: 50 W

Many of them generate power in the form of direct current (e.g. PV, fuel cells) or in the form of alternate current at a different frequency from the required 50 Hz (e.g. wind generators, micro-turbine). Therefore, the system containing these sources requires a power electronic interface. The system is represented on Figs. 2 and 3.

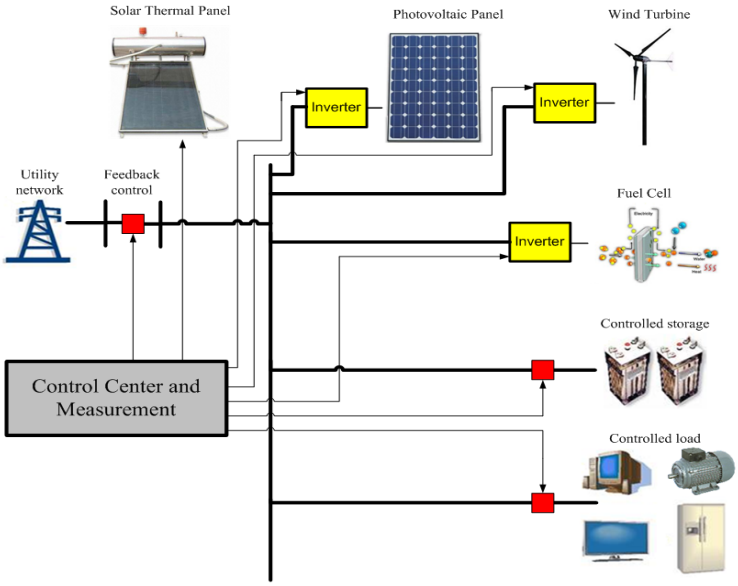


Fig. 2. Control of Microgrid Laboratory renewable system

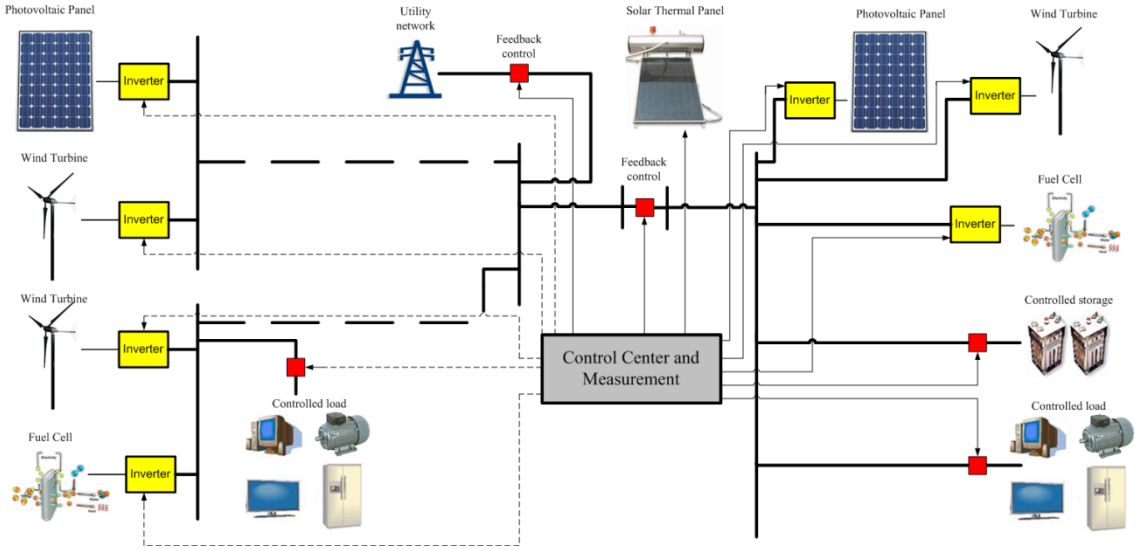


Fig. 3. Virtual micro-grid control

The system can be operated connected to grid or in isolated system. In both situations, the control of all equipment is done with a centralized system of measurement and control. With this control system, it is possible to measure the generated energy by the wind turbine, photovoltaic panels, fuel cell, storage discharging and the energy consumed by the load. When implementing the central control, it is possible to regulate the fuel cell, the storage and the load for balancing the system according to the defined strategy [10].

It is also possible compare the forecast values of wind turbine and photovoltaic panels generation with the real values. This possibility improves the management of renewable energy resources.

The generation capability of the different units will be on-line monitored, and remotely switched by the

scheduler.

When unbalance between active power generation and active power load demand is detected, the frequency deviates from its nominal value. Therefore, the isolated system should be able to maintain frequency in an acceptable operating range achieve power quality standards [11].

In a further extension, the remote switches will be realized on IP base, so the physical microgrid will be extended to virtual microgrid.

## 4. Problem Formulation

The technical economical power dispatching consists in the identification of the optimal set points of the generating units in an electrical system. Usually, the objective is to minimize the production cost of these units, subjected to all the technical constraints.

The problem formulation of the Laboratory system is developed as a VPP operation in an isolated grid. However, it may be connected to the distribution network. Figure 4 presents the scheme that can be used in the power balance formulation.

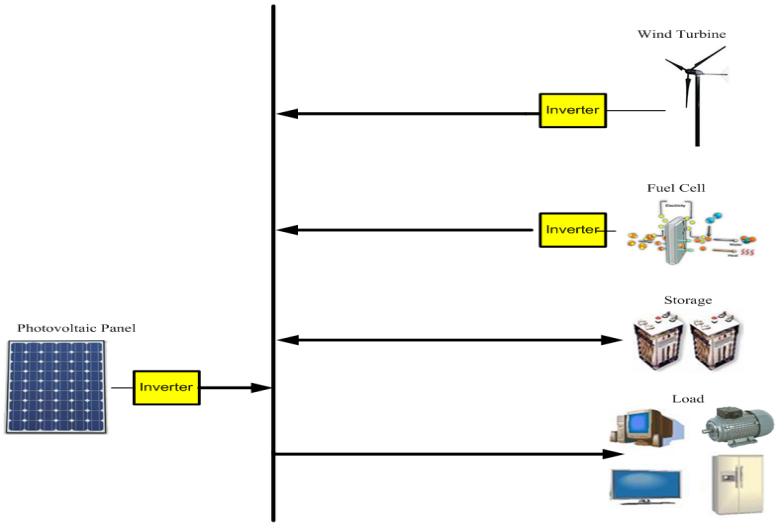


Fig.4. Microgrid Laboratory operated as an isolated system

In order to determine the optimal generated power by wind, photovoltaic, fuel cell and the storage battery charging and discharging, the optimal operation is formulated taking into account the following considerations:

- The wind power generation strongly depends on the weather. The generation capability can be estimated in advance for a 24 hours period. The wind energy is dispatched during the mentioned period due to the low generation cost;
- The photovoltaic generation can be well forecasted, too;
- The fuel cell has limited output for a long time, but the total generated energy is determined by the amount of the hydrogen fuel;
- The storage discharging is limited for maximal discharging capacity and existing storage energy;
- The loads are forecasted considering several aspects, however the most of the loads can be controlled between limits (this is the DSM - Demand Side Management);
- To system balance, the VPP can settle terms of reserve. For example the VPP can limit the minimum reserve to the 10 % of load forecast. This reserve can be assured by storage and fuel cell.

The main objective is to carry out an optimal dispatch taking into account all the aforementioned considerations.

The expected result will be the following priorities: 1st - wind, 2nd – photovoltaics, 3rd - Fuel cell (if it is necessary). The surplus energy is used for charging the storage battery capacity. The different units have different costs, as well. The wind and solar energy are cheaper, or with low cost. The storage energy has being limited; the hydrogen based fuel cells have expensive cost and limited capacity. It is only the emergency reserve.

This continuous constrained portfolio problem is solved by CPLEX in GAMS platform, Genetic algorithm (GA) and Evolutionary particle swarm optimization (EPSO) as can be seen next.

The optimal schedule of the demand and generation units can be made for five minutes, one hour, and one day or for one week. Thus, it depends on the load forecasting, for wind and photovoltaic energy generation forecast.

The problem constraints have been elaborated considering the five different operation modes:

1. There is a surplus energy to store (for more details see Fig.5).

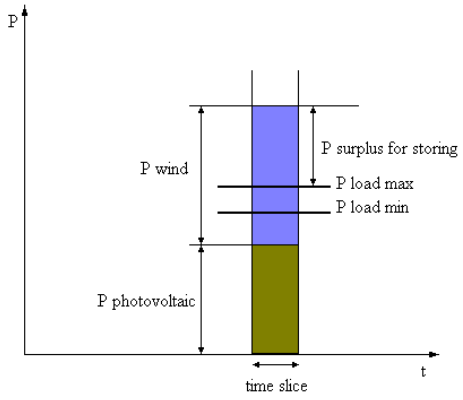


Fig. 5. Surplus of primary energy

2. The primary generation is not enough therefore the battery is discharged. In this case a 25% is considered.
3. In case of the lack of primary generation (no wind and/or sunshine) the battery and Fuel Cell come into operation (see Fig.6).

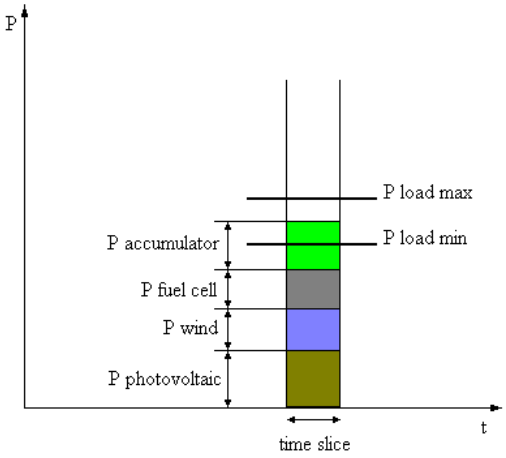


Fig. 6. The storage and the fuel cell are in operation

4. In case of the lack of energy storage, only Fuel Cell comes into operation.
5. In unsatisfactory energy generation case the load must be shed.

The main propose is to find the minimal marginal cost for a 24 hour period. However it can be extended to one week, one month or one year.

The objective function is stated as follows:

$$Min\ f = \sum_{t=1}^{24} C_w(t) \cdot P_w(t) + C_{Pv}(t) \cdot P_{Pv}(t) + C_{Fc}(t) \cdot P_{Fc}(t) + C_{Sc}(t) \cdot P_{Sc}(t) - C_{Sd}(t) \cdot P_{Sd}(t) + C_{Ue}(t) \cdot P_{Ue}(t) - C_{Exe}(t) \cdot P_{Exe}(t) \quad (1)$$

Subjected to the following technical constraints:

1. First Kirchhoff Law or Power Balance

$$\sum_{t=1}^{24} P_w(t) + P_v(t) + P_{Fc}(t) + P_{Sd}(t) + P_{Ue}(t) = \sum_{t=1}^{24} Load(t) + P_{Sc}(t) + P_{Exe}(t) \quad (2)$$

2. Wind generation limits in each period "*t*"

$$P_w(t) \leq P_{Wmax}(t); \quad t = 1, \dots, 24 \quad (3)$$

3. Photovoltaic generation limits in each period "*t*"

$$P_v(t) \leq P_{Vmax}(t); \quad t = 1, \dots, 24 \quad (4)$$

4. Fuel Cell limits in each period "*t*"

$$P_{Fc}(t) \leq 0.08; \quad t = 1, \dots, 24 \quad (5)$$

5. Storage battery limits in each period "*t*"

$$P_S(t) \leq 0.20; \quad t = 1, \dots, 24 \quad (6)$$

6. Storage battery maximal discharge limits in each period "*t*"

$$P_{Sd}(t) \leq 0.05 \cdot X(t); \quad t = 1, \dots, 24; \quad X = 0.1 \quad (7)$$

7. Storage battery maximal charge limits in each period "*t*"

$$P_{Sc}(t) \leq 0.20 \cdot Y(t); \quad t = 1, \dots, 24; \quad Y = 0.1 \quad (8)$$

8. The battery cannot charge and discharge at the same time in each time slice "*t*"

$$X(t) + Y(t) \leq 1; \quad t = 1, \dots, 24; \quad X, Y = 0,1 \quad (9)$$

9. Storage battery maximal discharge limits in each period "*t*" considering the battery state storage in period *t-1*

$$P_{Sd}(t) - P_S(t-1) \leq 0; \quad t = 1, \dots, 24 \quad (10)$$

10. Storage battery maximal charge limits in each period "*t*" considering the battery state storage in period *t-1*

$$P_{Sc}(t) + P_S(t-1) \leq 0.20; \quad t = 1, \dots, 24 \quad (11)$$

11. Balance state of the battery

$$P_S(t) = P_S(t-1) - P_{Sd}(t) + P_{Sc}(t); \quad t = 1, \dots, 24 \quad (12)$$

12. Initial state of the battery

$$P_S(0) = 0.10 \quad (13)$$

For the succeeding time slices the constraints are the same. The existent storage energy ($P_S$) is updated between time slices. If considered a large number of time slices, it is possible to minimize the operation costs and optimize the storage management.

The Distribution Network has not been taken into account due to its small dimension. However, its inclusion in this mathematical model is very easy. In this particular case the active power losses is a squared function of the current. This function can be linearized in the objective function and constraint of the flow limit on the lines can be included. Therefore, the solution methods proposed to solve the Mixed Integer Linear Problem is still valid.

## 5. Mathematical Solution Methods

The optimal dispatch problem formulated in the Section 4 is a linear model with two types of variables that are continuous and binaries. The nature of the formulated problem is combinatorial. As a consequence, several solution techniques have been proposed to solve the unit commitment problem such as heuristics [12]-[14], dynamic programming [15]-[17], mixed-integer linear programming [18], [19], Lagrangian relaxation [20], simulated annealing [21] and evolution-inspired approaches [22]-[24] can be adopted to solve the intelligent microgrid scheduling. In this paper, the MILP and the evolution inspired approaches GA and EPSO have been chosen for solving the optimal dispatch of renewable energy microgrid optimal management problem.

### *A) Mixed Integer Linear Programming (MILP)*

The MILP optimization technique has been chosen for solving the optimal dispatch of renewable energy park problem. The main reason for it is the convergence guarantee to the optimal solution in a finite number of steps [25] while providing a flexible and accurate modeling framework. In addition, during the search of the problem tree, information on the proximity to the optimal solution is available. Efficient mixed-integer linear programming such as the branch-and-cut algorithm based on GAMS platform under CPLEX name has been used in this paper.

### *B) Genetic Algorithm (GA)*

The Genetic Algorithms (GA) are part of the evolutionary algorithms family which are models inspired in the Nature. GA´s are usually considered as function optimizers [26].

In this paper the Genetic Algorithm Optimization Toolbox (GAOT) for MATLAB 5 has been adapted for solving the optimization problem of the optimal dispatch of a small renewable energy park at the Laboratory level. GAOT implements simulated evolution in the MATLAB environment using binary or real representations [27]. This implementation is very flexible in the genetic operators, selection function, termination functions as well as evolution function that can be used. The implementation is described in [27] and adopted in this work.

The GA works with a set of (codified solutions) that constitutes a population. Such population is able to evolve by application of the process of selection, mutation, reproduction and crossover. The strongest individuals (solutions) survive during the optimization process or generations. An initial population (also known as start population) has been generated randomly. The select operation creates an intermediate population that picks up the best individuals among the initial population by means of fitness evaluation function (cost). To obtain an evolved population is necessary to apply some operators (crossover and mutation) which becomes the new generation. For selecting the best individuals in the population was used roulette [28] and normalized geometric distribution selection. The Crossover is an operator used by genetic algorithms to generate new individuals (solutions) through picking points randomly and switching their segments. Thus, arithmetic crossover takes two parents *P1, P2* and performs an interpolation along the line formed by these parents. The number of crossover operations defined in this case is 2 for each generation. The mutation operator process used is the boundary mutation that consists of changing one of the parent's values randomly and so changes its upper or lower bound. The number of boundary mutations defined in this case is 24.

The flowchart of the GA algorithm is depicted in figure 7.

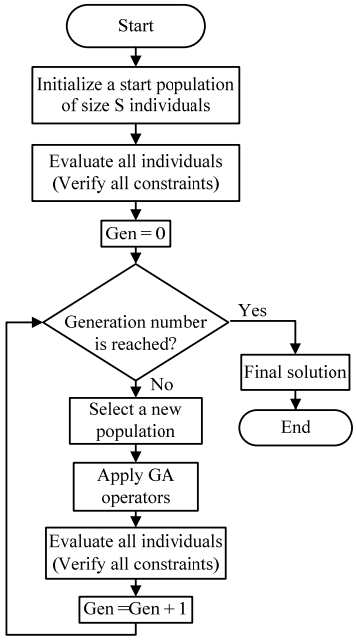


Fig. 7. Genetic Algorithm process flowchart

*C) Evolutionary Particle Swarm Optimization (EPSO)*

Conversely of the GA the classic Particle Swarm Optimization (PSO) has no selection and mutation operator [29], [30]. The movement rule of PSO is defined by three strategic parameters (see Figure 8): inertia, memory and cooperation [31], [32].

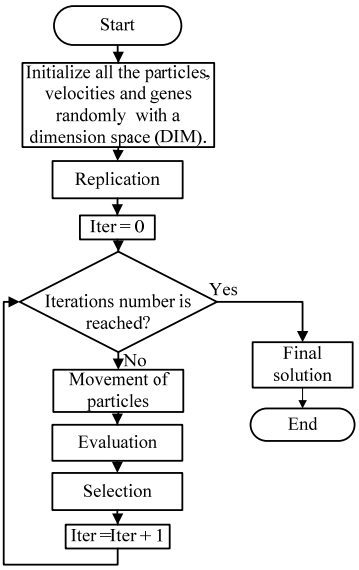


Fig. 8. Evolutionary Particle Swarm Optimization process flowchart

On the other hand, Evolutionary Particle Swarm Optimization (EPSO) introduces a new approach: mutation of the strategic parameters and selection by stochastic tournament of particles passing to the next generation. Given a population as a set of particles, the general of EPSO algorithm can be explained as follows:

1. Replication: Each particle is replicated one (r = 1) time.
2. Mutation: The strategic parameters $w$ of each particle, are mutated according to:

$$w_{t+1} = w_t + [random(N(0,1)) \cdot \tau] \quad (1)$$

In this paper the Gaussian mutation to the particle's weight was used where τ is the learning parameter, externally fixed. Note that the Strategic parameters are randomly initialized between 0 and 1.

3. Reproduction: Each particle generates 1 descendent according to the movement equation:

$$v_{t+1} = v_t \cdot inertia(vi) + w_t \cdot memory(b_t - X_t) + w_t \cdot coop(bG_t - X_t) \quad (2)$$

and

$$bG_{t-1} = bG + w_t \cdot deviation\ N(0,1) \quad (3)$$

Finally, the basic particle movement rule is:

$$X_{t+1} = X_t + v_{t+1} \quad (4)$$

4. Evaluation: Each particle has its fitness value, according to its current position in search space.
5. Selection: By stochastic tournament, the best particle of each group of *r+1* descendents (population + *r* replicas) of each individual of previous generation is selected to form the new generation.

The EPSO algorithm is organized as shown in figure 9.

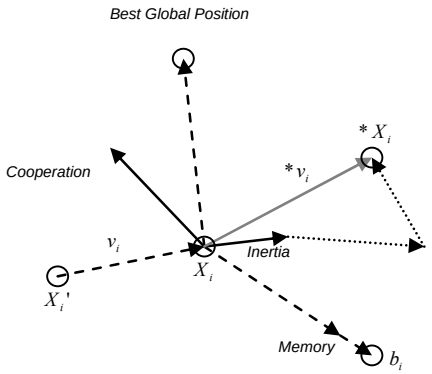


Fig. 9 Spatial representation of EPSO movement rule

## 6. Test Case

A real test case has been performed to illustrate the generality and the effectiveness of the proposed methodology. This study case corresponds to Laboratory microgrid Renewable Equipment (see Fig.1). The generation capacity and load used are shown Table 1.

The optimization problem of Laboratory equipment has been analyzed for the 24 hours period sequential time. In order to schedule the generation units, a cost of each generation technology is established. The considered prices are: Wind energy 0.4 Eur/kWh; photovoltaic 0.4 Eur/kWh; fuel cell 0.9 Eur/kWh; storage discharging 0.6 Eur/kWh; storage charging 0.4 Eur/kWh; undelivered power is 1.5 Eur/kWh and the excess energy is 0 Eur/kWh.

Some important results as well as the optimal renewable energy dispatch have been obtained taking into account the marginal cost of each generation technology.

Figure10 presents the optimal dispatch obtained by solver CPLEX in GAMS platform. In this case, (see Figure11) the battery charges only in the intervals 2 and 4 respectively. All values are given in W for more appreciation in Tables and Figures.

Table 1

Generation capacity and load used in the test case

| Hour | $P_W$(W) | $P_V$(W) | $P_{Fc}$(W) | $P_{SC}$(W) | $P_{SD}$(W) | Load (W) |
|---|---|---|---|---|---|---|
| 1 | 130 | 0 | | | | 160 |
| 2 | 150 | 0 | | | | 140 |
| 3 | 140 | 0 | | | | 150 |
| 4 | 160 | 0 | | | | 120 |
| 5 | 100 | 0 | | | | 110 |
| 6 | 120 | 5 | | | | 100 |
| 7 | 150 | 10 | | | | 170 |
| 8 | 180 | 30 | | | | 180 |
| 9 | 170 | 60 | | | | 200 |
| 10 | 160 | 100 | | | | 220 |
| 11 | 120 | 130 | | | | 230 |
| 12 | 130 | 140 | ≤80 | ≤200 | ≤50 | 240 |
| 13 | 150 | 150 | | | | 240 |
| 14 | 176 | 140 | | | | 230 |
| 15 | 185 | 130 | | | | 220 |
| 16 | 120 | 100 | | | | 210 |
| 17 | 130 | 60 | | | | 210 |
| 18 | 140 | 30 | | | | 220 |
| 19 | 170 | 10 | | | | 230 |
| 20 | 190 | 5 | | | | 240 |
| 21 | 120 | 0 | | | | 250 |
| 22 | 170 | 0 | | | | 200 |
| 23 | 130 | 0 | | | | 190 |
| 24 | 150 | 0 | | | | 180 |

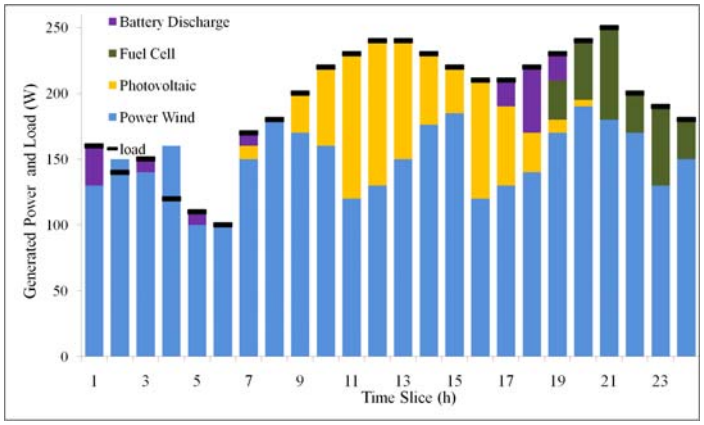


Fig. 10. Hourly generated power obtained by MILP

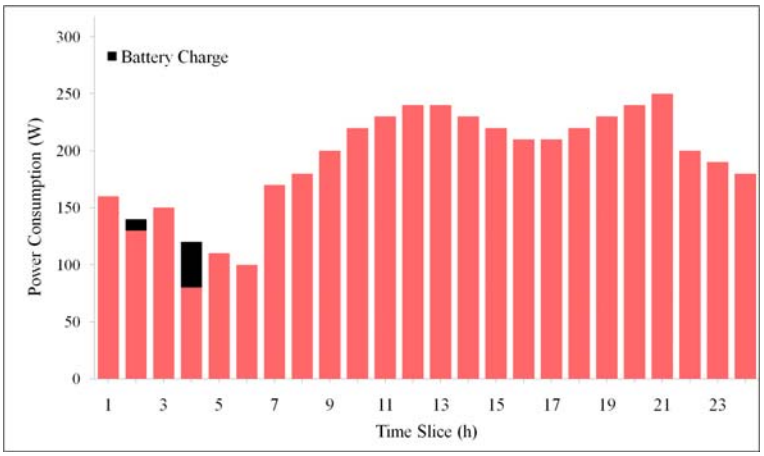


Fig.11. Hourly power consumption obtained by MILP

Genetic Algorithm (GA) and Evolutionary Particle Swarm Optimization techniques (EPSO) have also been applied to solve the optimal renewable energy park dispatch. The dispatch results of these two meta-heuristic techniques are different as can be seen on Figs. 12 and 13. In this case, the battery charges in the intervals 4, 6, 7, 8, 9, 10, 13, 14, 16, 18, 19, 22 for the GA and in the intervals 3, 5, 7, 8, 9, 10, 11, 13, 14, 19 and 24 for the EPSO respectively. All values can be seen on Figs. 14 and 15.

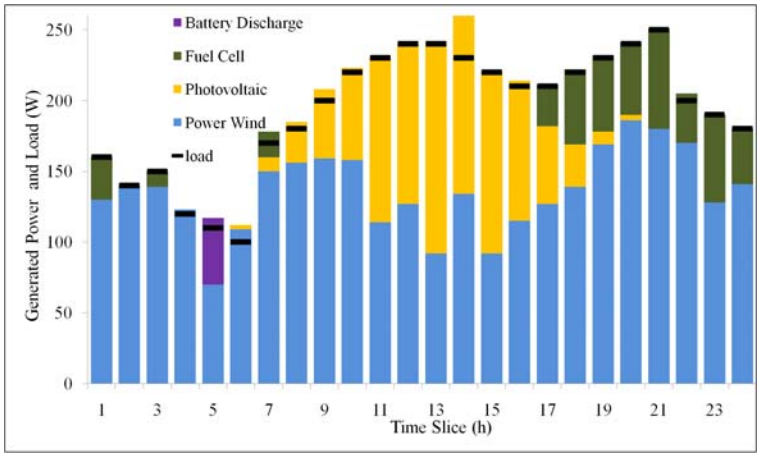


Fig. 12. Hourly generated power obtained by GA

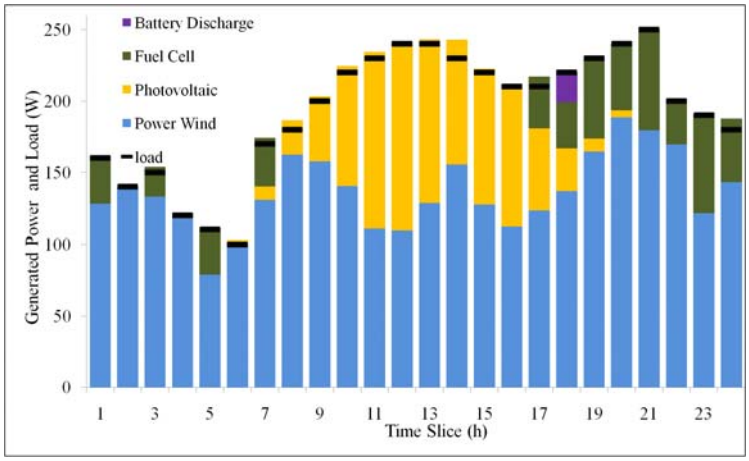


Fig. 13. Hourly generated power obtained by EPSO

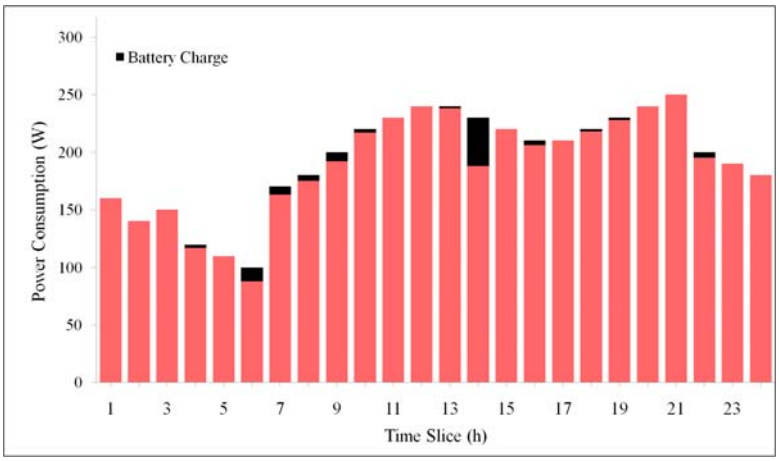


Fig. 14 Hourly power consumption obtained by GA

Before applying these algorithms to the dispatch problem, some tests were carried out in order to determine the best values for the parameters that control the GA and EPSO.

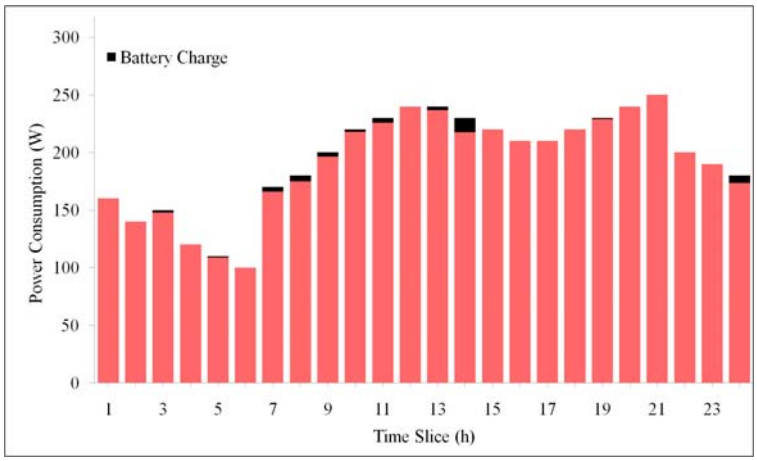


Fig. 15. Hourly power consumption obtained by EPSO

The optimal dispatch problem was studied from the point of view of results and computation times. The suitable parameters for GA and EPSO can be seen in the Tables 2 and 3, respectively. The performance of the GA and EPSO algorithms are depicted in Figs. 16 and 17, respectively. The comparison results from CPU execution time point of view can be seen in Table 4.

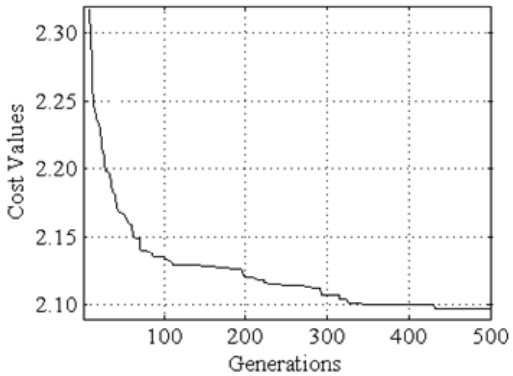


Fig. 16. Evolution of objective function obtained by GA

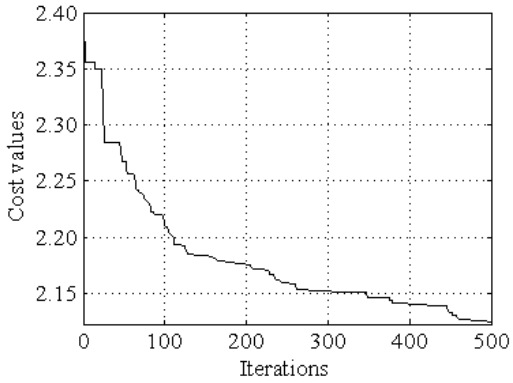


Fig. 17. Evolution of objective function obtained by EPSO

Table 2

Tuning Parameters Genetic Algorithm

| Attribute | Description | Used value |
|---|---|---|
| $\varepsilon$ | Epsilon indicates the threshold for two fitness to find the best solution | $10^{-10}$ |
| Crossover operator | Arithmetic Crossover | 2 crossover operations per generation |
| Mutation perator | Boundary Mutation | 24 mutations per generation |
| Select Operator | Normalized geometric distribution | Probability of 1.00 |
| Select Operator 2 | Roulette method | - |
| Initial population | Population size | 100 |
| Number of generations | Number of generations applied to start population | 500 |

Table 3

Tuning Parameters

Evolutionary Particle Swarm Optimization

| Attribute | Description | Used value |
|---|---|---|
| Number of particles | Number of particles | 40 |
| Search space | Dimension of values for each particle | 120 |
| Number of iterations | Number of iterations applied to swarm | 500 |
| $\tau$ | Tau indicates the mutation factor value | 0.7 |
| Mutation method | Gaussian mutation | $w_{i,j} = w_{i,j} + \text{Random}(0,1) \cdot \tau$ |

Table 4

Computational Performance MILP, GA and EPSO

| Algorithm | Objective Function Value | Number of Iterations or generations | Computational time (S) |
|---|---|---|---|
| MILP | 2.0185 | 10000 | 2 |
| GA | 2.0960 | 500 | 30 |
| EPSO | 2.1240 | 100 | 5 |

GA and EPSO have been chosen since it has already proven to be successful in solving many problems in power system operation and scheduling [30]-[31], [33]-[34]. The algorithm has been successfully implemented using a high-performance computation library developed in GECAD/ISEP, Portugal.

For the application of the methodology a digital program in GAMS platform has been developed. Other two meta-heuristic optimization techniques have also been developed and applied to solve the problem. All cases have been tested on a PC compatible with 4 processor Intel Xeon X5450, 3.0-GHz, 4GB of random-access-memory (RAM) and Windows Server 2008 Operating System.

Table 5 shows in an easier way the results obtained by the three optimization techniques. This table is a summary of optimal dispatch of the renewable energy park treated in this work.

Table 5

Optimal Dispatch Results Obtained by MILP, GA and EPSO Algorithms

| HOUR | $P_W$ | | | $P_V$ | | | $P_{FC}$ | | | $P_{SC}$ | | | $P_{SD}$ | | | LOAD |
|---|---|---|---|---|---|---|---|---|---|---|---|---|---|---|---|---|
| | MILP | GA | EPSO | MILP | GA | EPSO | MILP | GA | EPSO | MILP | GA | EPSO | MILP | GA | EPSO | |
| 1 | 130 | 130 | 130 | 0 | 0 | 0 | 0 | 30 | 32 | 0 | 0 | 0 | 30 | 0 | 0 | 160 |
| 2 | 150 | 140 | 150 | 0 | 0 | 0 | 0 | 0 | 0 | 10 | 0 | 0 | 0 | 0 | 0 | 140 |
| 3 | 140 | 139 | 140 | 0 | 0 | 0 | 0 | 11 | 21 | 0 | 0 | 2 | 10 | 0 | 0 | 150 |
| 4 | 160 | 123 | 160 | 0 | 0 | 0 | 0 | 0 | 0 | 40 | 3 | 0 | 0 | 0 | 0 | 120 |
| 5 | 100 | 70 | 100 | 0 | 0 | 0 | 0 | 0 | 33 | 0 | 0 | 33 | 10 | 47 | 0 | 110 |
| 6 | 100 | 109 | 120 | 0 | 3 | 5 | 0 | 0 | 0 | 0 | 12 | 0 | 0 | 0 | 0 | 100 |
| 7 | 150 | 150 | 150 | 10 | 10 | 10 | 0 | 18 | 34 | 0 | 7 | 4 | 10 | 0 | 0 | 170 |
| 8 | 180 | 156 | 180 | 0 | 29 | 30 | 0 | 0 | 0 | 0 | 5 | 5 | 0 | 0 | 0 | 180 |
| 9 | 170 | 159 | 170 | 30 | 49 | 60 | 0 | 0 | 0 | 0 | 8 | 3 | 0 | 0 | 0 | 200 |
| 10 | 160 | 158 | 160 | 60 | 65 | 100 | 0 | 0 | 0 | 0 | 3 | 2 | 0 | 0 | 0 | 220 |
| 11 | 120 | 114 | 120 | 110 | 116 | 32 | 0 | 0 | 0 | 0 | 0 | 4 | 0 | 0 | 0 | 230 |
| 12 | 130 | 127 | 130 | 110 | 113 | 76 | 0 | 0 | 0 | 0 | 0 | 0 | 0 | 0 | 0 | 240 |
| 13 | 150 | 92 | 150 | 90 | 150 | 110 | 0 | 0 | 0 | 0 | 2 | 3 | 0 | 0 | 0 | 240 |
| 14 | 176 | 134 | 176 | 54 | 138 | 37 | 0 | 0 | 0 | 0 | 42 | 12 | 0 | 0 | 0 | 230 |
| 15 | 185 | 92 | 185 | 35 | 128 | 29 | 0 | 0 | 0 | 0 | 0 | 0 | 0 | 0 | 0 | 220 |
| 16 | 120 | 115 | 120 | 90 | 99 | 13 | 0 | 0 | 0 | 0 | 4 | 0 | 0 | 0 | 0 | 210 |
| 17 | 130 | 127 | 130 | 60 | 55 | 60 | 0 | 29 | 36 | 0 | 0 | 0 | 20 | 0 | 0 | 210 |
| 18 | 140 | 139 | 140 | 30 | 30 | 30 | 0 | 53 | 32 | 0 | 2 | 0 | 50 | 0 | 21 | 220 |
| 19 | 170 | 169 | 170 | 10 | 9 | 10 | 30 | 54 | 58 | 0 | 2 | 1 | 20 | 0 | 0 | 230 |
| 20 | 190 | 186 | 190 | 5 | 4 | 5 | 45 | 51 | 47 | 0 | 0 | 0 | 0 | 0 | 0 | 240 |
| 21 | 180 | 180 | 180 | 0 | 0 | 0 | 70 | 71 | 71 | 0 | 0 | 0 | 0 | 0 | 0 | 250 |
| 22 | 170 | 170 | 170 | 0 | 0 | 0 | 30 | 35 | 31 | 0 | 5 | 0 | 0 | 0 | 0 | 200 |
| 23 | 130 | 128 | 130 | 0 | 0 | 0 | 60 | 62 | 57 | 0 | 0 | 0 | 0 | 0 | 2 | 190 |
| 24 | 150 | 141 | 150 | 0 | 0 | 0 | 30 | 39 | 45 | 0 | 0 | 6 | 0 | 0 | 0 | 180 |

For a depth comparison of the results obtained by the different optimization technique that are MILP, GA and EPSO, the authors proceed to present all the results in figures format. For instance, the wind power resulted by the application of the three optimization technique has been drawn in the same figure as shown in Figure 18. It is

important to note that the wind power is a continuous and positive variable, in this case all the optimization techniques have generally the same tendency regarding to the obtained results.

## 7. Conclusions

In this paper an optimal operation of an isolated system by a VPP is presented and discussed. The main goal is to decide the best VPP management strategy to minimize the generation costs of wind energy, photovoltaic energy, fuel cell energy and optimize storage charging and discharging time subjected to all the operation technical constraints.

The dispatch has been formulated as a mixed integer linear programming problem and solved by three optimization techniques that have been developed and tested to a real case study presented and discussed in this work. Performance of each technique has been studied demonstrating that the MILP is the most adequate technique to solve this type of problem, handling effectively the binary problem variables.

The application of the methodology to a real case presented in the microgrid Laboratory, demonstrates the effectiveness and the robustness of the proposed model. It is also verified that the proposed method has a very low execution time for solving a mixed integer linear programming problem. The proposed model can help the planner engineer to minimize the operation cost of the generations units taking into account the reliability expressed in the undelivered energy cost.

## Acknowledgments

The authors would like to acknowledge the Portuguese Science and Technology Foundation (FCT), the European Fund for Regional Development (FEDER), the Operational Program for Science Technology and Innovation (POCTI), the Information Society Operational Program (POSI), the Operational Program Science and Innovation (POCI), the Operational Program for the Knowledge Society (POSC) and the Program of Projects in all Scientific Areas (PTDC) for their support to R&D Projects and GECAD Unit.

## References

[1] European Commission, “European SmartGrids technology platform: Vision and strategy for Europe’s electricity networks of the future” (April) (2006). [online]. Available: http://ec.europa.eu/research/energy/pdf/smartgrids_en.pdf; http://www.smartgrids.eu

[2] E. Ghiani, S. Mocci, F. Pilo, “Optimal Reconfiguration of Distribution Networks According to the Microgrid Paradigm.”, International Conference on Future Power Systems, 2005, (November) (2005).

[3] H. H. Zeineldin, E. F. El-Saadany, M. M. A. Salama, “Distributed Generation Micro-Grid Operation: Control and Protection”, Power Systems Conference: Advanced Metering, Protection, Control, Communication, and Distributed Resources, 2006, (March) (2006).

[4] P. Piagi, R. H. Lasseter, “Autonomous control of Microgrids”, IEEE Power Engineering Society General Meeting, 2006, (June) (2006).

[5] A. Carlos, T. Hernandez-Aramburo, C. Green, N. Mugniot, “Fuel Consumption Minimization of a Microgrid”, IEEE Trans. on Indus. App., vol. 41, n. 3, (2005) 673 – 682.

[6] W. El-Khattam, K. Bhattacharya, Y. Hegazy, Member, M. M. A. Salama, “Optimal Investment Planning for Distributed Generation in a Competitive Electricity Market”, IEEE Trans. on Power Syst., vol. 19, No.3, (August) (2004).

[7] GAMS Development Corporation, GAMS-The Solver Manuals, GAMS User Notes. Washington, DC, (January) (2001).

[8] H. Morais, M. Cardoso, L. Castanheira, Z. Vale, I. Praça, "A Decision-Support Simulation Tool for Virtual Power Producers", International Conference on Future Power Systems, (2005).

[9] P. Kádár, "Energy on the roof", in 3rd Romanian-Hungarian Joint Symposium on Applied Computational Intelligence,Timisoara, Romania, SACI Proceedings, (May(25-26)) (2006) 343-352.

[10] H. Ferenc, "Magyarország els folyamatosan hálózatra termel mini naper_mve", in Elektrotechnika, Hungarian, 7-8, (2004) 232-233.

[11] S. Roland, "A napelem cellák vizsgálatának kutatási eredményei", in Elektrotechnika, Hungarian, 2, 8-9 (2006).

[12] F. N. Lee, "Short-term thermal unit commitment—A new method," IEEE Trans. on Power Syst., vol. 3, no. 2, (May) (1988) 421–428.

[13] C. Li, R. B. Johnson, and A. J. Svoboda, "A new unit commitment method," IEEE Trans. on Power Syst., vol. 12, no. 1, (February) (1997) 113–119.

[14] T. Senjyu, K. Shimabukuro, K. Uezato, and T. Funabashi, "A fast technique for unit commitment problem by extended priority list," IEEE Trans. on Power Syst., vol. 18, no. 2, (May) (2003) 882–888.

[15] W. L. Snyder, H. D. Powell, and J. C. Rayburn, "Dynamic-programming approach to unit commitment," IEEE Trans. on Power Syst., vol. 2, no. 2, (May) (1987) 339–350.

[16] W. J. Hobbs, G. Hermon, S. Warner, and G. B. Sheblé, "An enhanced dynamic programming approach for unit commitment," IEEE Trans. on Power Syst., vol. 3, no. 3, (August) (1988) 1201–1205.

[17] Z. Ouyang and S.M. Shahidehpour, "An intelligent dynamic-programming for unit commitment application," IEEE Trans. on Power Syst., vol. 6, no. 3, (August) (1991) 1203–1209.

[18] T. S. Dillon, K. W. Edwin, H. D. Kochs, and R. J. Tand, "Integer programming approach to the problem of optimal unit commitment with probabilistic reserve determination," IEEE Trans. on Power Apparatus and Syst., vol. PAS-97, no. 6, (November-December) (1978) 2154–2166.

[19] J. Medina, V. H. Quintana, and A. J. Conejo, "A clipping-off interior point technique for medium-term hydro-thermal coordination," IEEE Trans. on Power Syst., vol. 14, no. 1, (February) (1999) 266–273.

[20] W. Ongsakul and N. Petcharaks, "Unit commitment by enhanced adaptive Lagrangian relaxation," IEEE Trans. on Power Syst., vol. 19, no.1, (February) (2004) 620–628.

[21] G. K. Purushothama and L. Jenkins, "Simulated annealing with local search—A hybrid algorithm for unit commitment," IEEE Trans. on Power Syst., vol. 18, no. 1, (February) (2003) 273–278.

[22] J. M. Arroyo and A. J. Conejo, "A parallel repair genetic algorithm to solve the unit commitment problem," IEEE Trans. on Power Syst., vol. 17, no. 4, (November 2002) 1216–1224.

[23] C. C. A. Rajan and M. R. Mohan, "An evolutionary programming-based tabu search method for solving the unit commitment problem," IEEE Transa. on Power Syst., vol. 19, no. 1, (February) (2004) 577–585.

[24] I. G. Damousis, A. G. Bakirtzis, and P. S. Dokopoulos, "A solution to the unit commitment problem using integer-coded genetic algorithm," IEEE Trans. on Power Syst. vol. 19, no. 2, (May) (2004) 1165–1172.

[25] G. L. Nemhauser and L. A. Wolsey, Integer and Combinatorial Optimization. New York: Wiley-Interscience, (1999).

[26] D. E. Goldberg, "Genetic Algorithms in Search, Optimization and Machine Learning," Kluwer Academic Publishers, Boston, MA, (1989).

[27] C. Houck, J. Joines, M. Kay, "A Genetic Algorithm for Function Optimization: A MatLab Implementation", NCSU-IE TR 95-09, (1995).

[28] "Roulette wheel selection", available online: http://www.edc.ncl.ac.uk/highlight/rhjanuary2007g02.php/.

[29] K.T. Chaturvedi, M. Pandit, L. Srivastava, "Self-organizing hierarchical particle swarm optimization for nonconvex economic dispatch," IEEE Trans. on Power Syst., vol. 23, no.3, (August) (2008), 1079-1087.

[30] J.K. Wu, J.Q. Zhu, G.T. Chen, et al., "A Hybrid Method for Optimal Scheduling of Short-Term Electric Power Generation of Cascaded Hydroelectric Plants Based on Particle Swarm Optimization and Chance-Constrained Programming," IEEE Trans. on Power Syst., vol. 23, no. 4, (November) (2008), 1570-1579.

[31] C.M. Huang, F.L. Wang, “An RBF network with OLS and EPSO algorithms for real-time power dispatch,” IEEE Trans. on Power Syst., vol. 22, no.1, (February) (2007) 96-104.

[32] T.Y. Lee, “Optimal spinning reserve for a wind-thermal power system using EIPSO,” IEEE Trans. on Power Syst., vol. 22, no. 4, (November) (2007) 1612-1621.

[33] N. Amjady, H. Nasiri-Rad, “Economic dispatch using an efficient real-coded genetic algorithm,” IET Generation, Transmission & Distribution, vol. 3, no. 3, (March) (2009) 266 278.

[34] E. Gil, J. Bustos, H. Rudnick, “Short-term hydrothermal generation scheduling model using a genetic algorithm,” IEEE Trans. on Power Syst., vol. 18, no.4, (November) (2003) 1256 – 1264.

Vitae

**H. M. Khodr** received the Ph.D., M.Sc., and Engineer degrees in electrical engineering from the José Antonio Echeverría Higher Polytechnic Institute (ISPJAE), Havana, Cuba, in 1997 and 1993, respectively.
He is a former Associate Professor of electrical engineering at Universidad Simón Bolívar, Caracas, Venezuela. He was a Researcher at INESC Porto, Porto, Portugal. Presently, he is a Researcher at GECAD, Porto. He has participated in a number of projects performed for the local industries. His current research activities are concentrated on planning, operation, and economics of electrical distribution and industrial power systems; power quality; grounding systems; and optimization.

**João P. Soares** received the Engineer degree in Computer Science from the Polytechnic Institute of Porto (ISEP/IPP), Portugal in 2008. Currently he is attending a Master degree on Power Systems Engineering. He is an Assistant Researcher at GECAD–Knowledge Engineering and Decision-Support Research Center of the Engineering Institute of Porto–Polytechnic Institute of Porto (ISEP/IPP) granted by Fundação para a Ciência e a Tecnologia (FCT). His current research activities are concentrated in future energy distribution networks.

**Hugo Morais** received the B.Sc. degree in 2005 from the Polytechnic Institute of Porto, Porto, Portugal. He is also a PhD student with the University of Trás-os-Montes e Alto Douro, Vila Real, Portugal and his research interests include distributed generation and future power systems.

**N. El Halabi** received the Electrical Engineering degree in 2006 from Universidad Simón Bolívar, Venezuela. He is currently performing the Ph.D. in Renewable Energy at Universidad de Zaragoza, Spain. His research interests are Power system protection, integration and planning of hybrid power systems.

Miguel García-Gracia was born in Saint-Brieuc, France on April 23, 1963. He received his B.S. (1986), M.Sc. (1989), and Ph.D. (1996) degrees from the University of Zaragoza. He is presently Lecturer of Electrical Engineering and Area Director of Electric Power System at CIRCE. His main research interests are in the field of power system, power system protection, electrical energy system, renewable energy integration, lightning protections and dielectrics.

**Zita A. Vale** received the diploma in electrical engineering in 1986 and the Ph.D. degree in 1993, both from the University of Porto, Porto, Portugal.
She is a Coordinator Professor of power systems at the Engineering Institute of Porto—Polytechnic Institute of Porto (ISEP/IPP). She coordinates the Intelligent Energy Systems research line of GECAD, Porto. Her main research interests concern artificial intelligence (AI) applications to power system operation and control, electricity markets, and distributed generation. She is involved in several R&D projects concerning the application of AI and decision-support techniques to engineering problems.

**Carlos Ramos** received the graduation degree and the Ph.D. degree in electrical engineering from the University of Porto, Porto, Portugal, in 1986 and 1993, respectively.
He is a Coordinator Professor of computer engineering at the Engineering Institute of Porto—Polytechnic Institute of Porto (ISEP/IPP). His main R&D interests are artificial intelligence and decision-support systems.

# Anexo b. Artículo publicado referente a mejorar del comportamiento de las protecciones de distancia basadas en el algoritmo DEA ante la distorsión armónica en la red

Electric Power Systems Research 80 (2010) 582–591

Contents lists available at ScienceDirect

Electric Power Systems Research

journal homepage: www.elsevier.com/locate/epsr

# Improvement of DEA performance against harmonic distortion

M. García-Gracia[a,*], N. El Halabi[a], A. Montañés[b], H.M. Khodr[c], M. Villén[a]

[a] CIRCE, Research Center of Consumption and Energy Resource, C/Maria de Luna 3, 50018, Zaragoza, Spain
[b] Department of Electrical Engineering, University of Zaragoza, Spain
[c] GECAD – Knowledge Engineering and Decision-Support Research Center of the Polytechnic Institute of Porto (ISEP/IPP), Rua Dr. António Bernardino de Almeida 431, 4200-072 Porto, Portugal

ARTICLE INFO

*Article history:*
Received 3 February 2009
Received in revised form 24 July 2009
Accepted 24 October 2009
Available online 3 December 2009

*Keywords:*
Distance protection algorithm
Relaying system
Power system

ABSTRACT

This paper presents a filtering application to improve the behavior of the Differential Equation Algorithm (DEA) against harmonic distortion in transmission and distribution power systems. The proposed filter is based on Fast Fourier Transform (FFT) techniques during steady-state conditions. The voltage and current continuous-time equations are also considered, in fault conditions, to estimate the fundamental component waveforms of voltage and current. Simulations results show the singularities problems of DEA algorithm against harmonic distortion and the accurate operation achieved within 0.32 cycles using this filtering application.



## 1. Introduction

The basic requirement of a distance protection algorithm is the capability of high speed and selective isolation of faulted sections in the power system. Fourier analysis techniques are the most widely used tools in signal processing for distance relaying [1]. However, the time these methods need for operation is in the range of at least one and a half cycles. Protection algorithms based on traveling waves principle [2–4] offer the fastest operation time after fault inception, but put too high demands on current and voltage sampling time for accurate operation [4,5]. Unlike these algorithms, the Differential Equation Algorithm (DEA) [5–9] has an operating time below 0.32 cycles with less sample time requirements than traveling wave techniques. Thus, a relay based on the DEA is suitable since high speed operation is achieved including fault detection, estimation of fault location, fault classification and tripping decision within the operation time.

In [9] the behavior of the DEA algorithm is analyzed under different situations in a power distribution system without considering harmonic distortion and fault resistance, resulting in an efficient algorithm for fault detection and location.

However, the increasing application of electronic power facilities in the industrial environment bears to a significant harmonic distortion in the waveforms of voltages and currents [10]. This harmonic distortion in conjunction with the fault resistance and the transient components contained in the waveforms of voltages and currents during the fault period, introduces important measuring errors in the DEA algorithm [8]. These uncertainties implicit in the measured data must be removed to avoid misoperations and power disruption. This emphasizes the need to analyze the behavior of DEA in a power system with harmonic distortion aiming to develop suitable filtering methods to enhance the accuracy of the algorithm.

Some authors have proposed different filtering applications for harmonic waveforms. In [1] a mimic phasor estimator is proposed by using discrete Fourier Transform, where the filtered waveform is established in at least 0.5 cycles, but it is based on an iterative adaptive scheme for voltage and current phasors where convergence depends on variation of fault parameters. Otherwise, [8] proposes a medium post-filtering for DEA algorithm that rejects singularities problems due to harmonic distortion; however it demands an additional time in this stage before an accurate convergence to the fault distance. In [11] a recursive algorithm based on minimization of the absolute error in the waveform estimation is presented, where convergence time is in the range of 2.5 cycles and it is applied to study symmetrical components in unbalanced power systems. Unlike digital filters, several active filters have been proposed [12–15] to mitigate harmonic current effect over the power quality of the power system. These active filters offer a selective elimination of harmonic components, however under fault conditions, the accuracy of harmonic elimination is reduced and the filtered fundamental waveform may be misleading for DEA algorithm.

The method introduced in this paper takes the presumption that the peak value relation between the fundamental frequency component and the harmonic components remains similar in both prefault and fault state. Under this scope, a straightforward filter-

* Corresponding author. Tel.: +34 976761923; fax: +34 976762226.
*E-mail address:* mggracia@unizar.es (M. García-Gracia).

0378-7796/$ – see front matter © 2009 Elsevier B.V. All rights reserved.
doi:10.1016/j.epsr.2009.10.012

ing application is proposed for estimating fundamental waveforms of voltages and currents by means of continuous-time equations taking into account the information of prefault state to accelerate the estimation of the waveforms. Then, using the differential equation that describes an electric circuit, the algorithm determines the inductance and resistance seen by the relay.

The proposed algorithm provides capability for fast tripping decisions within 0.32 cycles, taking into account both accuracy and security. Extensive simulations and comparative studies of the proposed algorithm with the conventional DEA and Fourier techniques are reported and discussed.

## 2. The Differential Equation Algorithm

### 2.1. Presumptions and general equations in continuous time

Here is presented a summarized derivation of the DEA. A suitable reference for detailed derivation of DEA, considering mutual coupling effect, is [9]. The derivation of the equations for this algorithm requires the following presumptions:

- voltage and current transformers are ideal in the frequency range from 50 to 500 Hz
- the line is perfectly transposed
- shunt capacitance is neglected

The DEA algorithm is based on the differential equation that describes an electric circuit. Therefore, under fault conditions, the protected line is modeled as follows:

$$\begin{bmatrix} u_a \\ u_b \\ u_c \end{bmatrix} = k_r R_1 \begin{bmatrix} l_a \\ i_b \\ i_c \end{bmatrix} + k_l L_1 \frac{d}{dt} \begin{bmatrix} i_a \\ i_b \\ i_c \end{bmatrix} \quad (1)$$

where, $u_a, u_b, u_c$ and $i_a, i_b, i_c$ are the phase quantities of voltages and currents, respectively. The parameters $k_r$ and $k_l$ are the relative line length for the resistive part and the inductive part, respectively. For a fault on the protected line, both should be bounded between 0 and 1. In an ideal case, $k_r$ and $k_l$ should be similar. The arrays $R$ and $L$ are the resistance and the inductance array for the whole line, respectively.

Through the presumption of perfect transposition mentioned above, the following expressions are obtained:

$$R = \begin{pmatrix} R_s & R_m & R_m \\ R_m & R_s & R_m \\ R_m & R_m & R_s \end{pmatrix}; \quad L = \begin{pmatrix} L_s & L_m & L_m \\ L_m & L_s & L_m \\ L_m & L_m & L_s \end{pmatrix} \quad (2)$$

where the subscripts $s$ and $m$ are used for self and mutual parameters, respectively. The relation between these parameters is:

$$\begin{aligned} L_1 &= L_s - L_m \\ R_1 &= R_s - R_m \\ L_0 &= L_s + 2L_m \\ R_0 &= R_s + 2R_m \end{aligned} \quad (3)$$

being the subscripts 0 and 1 the zero and positive sequence, respectively. Subtracting self and mutual parameters in (3) gives:

$$\begin{aligned} L_0 - L_1 &= 3L_m \\ R_0 - R_1 &= 3R_m \end{aligned} \quad (4)$$

Using (4), and considering that the zero sequence current is:

$$i_0 = \frac{(i_a + i_b + i_c)}{3} \quad (5)$$

Eq. (1) can be rewritten as follows:

$$\begin{bmatrix} u_a \\ u_b \\ u_c \end{bmatrix} = k_r R_1 \begin{bmatrix} i_a \\ i_b \\ i_c \end{bmatrix} + k_l L_1 \frac{d}{dt} \begin{bmatrix} i_a \\ i_b \\ i_c \end{bmatrix} + k_r (R_0 - R_1) \begin{bmatrix} i_0 \\ i_0 \\ i_0 \end{bmatrix} + k_r (L_0 - L_1) \frac{d}{dt} \begin{bmatrix} i_0 \\ i_0 \\ i_0 \end{bmatrix} \quad (6)$$

and expressed in a general form as follows:

$$u = k_r i_r + k_l L_1 \frac{di_l}{dt} \quad (7)$$

being the derivation of variables $u$, $i_r$ and $i_l$ different for each type of fault (three phases, double phase to ground and SLG) [8].

### 2.2. Single line to ground faults

Considering a SLG fault on phase $a$ at a relative distance $k$ of the total length of the protected line, the voltage of the faulty phase is given by:

$$u_a = k_r [R_1 i_a + (R_0 - R_1) i_0] + k_l \left[ L_1 \frac{di_a}{dt} + (L_0 - L_1) \frac{di_0}{dt} \right] \quad (8)$$

Eq. (8) can be expressed as the general form (7), considering the following variables:

$$\begin{aligned} u &= u_a \\ i_r &= R_1 i_a + (R_0 - R_1) i_0 \\ i_l &= L_1 . i_a + (L_0 - L_1) i_0 \end{aligned} \quad (9)$$

### 2.3. Double phase to ground fault

For a double phase to ground fault between phases $a$ and $b$, the equation is:

$$(u_a - u_b) = k_r R_1 (i_a - i_b) + k_l L_1 \frac{d}{dt} (i_a - i_b) \quad (10)$$

Expressing (10) as the general form (7) leads to the following considerations:

$$\begin{aligned} u &= u_a - u_b \\ i_r &= R_1 (i_a - i_b) \\ i_l &= L_1 (i_a - i_b) \end{aligned} \quad (11)$$

### 2.4. Three phase fault

Assuming a symmetrical fault at a distance $k$ of the protected line, the general Eq. (1) is rewritten as:

$$\begin{bmatrix} u_a \\ u_b \\ u_c \end{bmatrix} = k_r R_1 \cdot \begin{bmatrix} i_a \\ i_b \\ i_c \end{bmatrix} + k_l L_1 \cdot \frac{d}{dt} \begin{bmatrix} i_a \\ i_b \\ i_c \end{bmatrix} \quad (12)$$

Since it is a symmetrical fault, that is $i_0 = 0$, the network can be treated as a single phase system. Any phase can be used to determine the values of $k_r$ and $k_l$. Using two sets of samples of voltage and current of the phase $a$, the equations that allow the values of $k_r$ and $k_l$ to be obtained are:

$$\begin{bmatrix} u_{a_n} \\ u_{a_{n+1}} \end{bmatrix} = \begin{bmatrix} R_1 i_{a_n} & L_1 \frac{di_{a_n}}{dt} \\ R_1 i_{a_{n+1}} & L_1 \frac{di_{a_{n+1}}}{dt} \end{bmatrix} \begin{bmatrix} k_r \\ k_l \end{bmatrix} \quad (13)$$

### 2.5. Solution of the continuous-time equations in discrete-time

The solutions of (8), (10) and (13) are expressed in reference [5] in discrete-time domain. The two unknown parameters $k_r$ and $k_l$

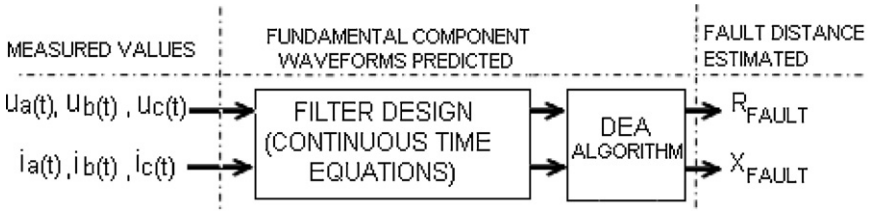


**Fig. 1.** Overview of the model with filtering application.

can be estimated by differentiating (7) as follows:

$$\begin{bmatrix} u \\ \frac{du}{dt} \end{bmatrix} = \begin{bmatrix} i_r & L_l \frac{di_l}{dt} \\ \frac{di_r}{dt} & L_l \frac{d^2 i_l}{dt^2} \end{bmatrix} \begin{bmatrix} k_r \\ k_l \end{bmatrix} \tag{14}$$

Subsequently, by using three continuous samples of $i$ and $u$, fault distance is given by:

$$k_{rn} = \frac{(i_{\ln} - i_{l(n-1)})(u_{(n-1)} + u_{(n-2)}) - (i_{l(n-1)} - i_{l(n-2)})(u_n + u_{(n-1)})}{\Delta T} \tag{15}$$

$$k_{\ln} = \left(\frac{\sigma}{2}\right) \times \frac{-(i_{rn} - i_{r(n-1)})(u_{(n-1)} + u_{(n-2)}) + (i_{r(n-1)} - i_{r(n-2)})(u_n + u_{(n-1)})}{\Delta T} \tag{16}$$

where $\sigma$ is the frequence sampling of the protective device, $n$ the index of time and $\Delta T$ the determinant of the inverse of the matrix in (14) expressed as follows:

$$\Delta T = (i_{r(n-1)} + i_{r(n-2)})(i_{\ln} - i_{l(n-1)}) - (i_{rn} + i_{r(n-1)})(i_{l(n-1)} + i_{l(n-2)}) \tag{17}$$

### 2.6. Singularities problems present in DEA against harmonic distortion

As (17) is a discrete-time signal, it has implicit a repetitive perturbation at a constant period which introduces a periodic frequency deformation. Therefore, when the determinant (17) gets values near to zero, $k_r$ and $k_l$ result in a mathematical indetermination. This indetermination is proportionally incremented the higher the frequency components that appear in the current waveform are. Such is the case of harmonic distortion in the power system. Consequently, if the sampling time fits with the frequency deformation, it results in an extremely poor estimation of the fault distance. Moreover, the inverse proportionality between fault resistance and fault current makes the numerical differentiation in (15) and (16) become closer to the zero axis. Thus, poor estimation and lack of convergence are expected to be obtained by DEA algorithm due to the fault resistance.

To deal with these additional factors that decrease the accuracy of DEA algorithm, it is necessary to introduce a filtering application as shown in Fig. 1. The proposed filter is based on continuous-time equations (22) and (28) of voltage and current, respectively, as it is explained in Section 5.

## 3. Power system test case simulation

### 3.1. Power system modeled

The power system shown in Fig. 2 has been considered for this study. The simulation has been done using PSCAD-EMTDC package [16,17] and with a sampling time of at least 50 kHz.

This power system consists in a 45 kV system that feeds a load of 1.5 MW and 0.53 Mvar through line 1 of 7.7 km and a load of 3.93 MW and 2.58 Mvar through line 2 (7.7 km). These loads are also connected to bus 2, through lines 3 and 4, both of 9.4 km. The electrical network connected to bus 1 and bus 2 is represented by its Thévenin equivalents, which are given by:

$$Z_{th1} = 4.25/84.4^\circ\ \Omega \quad Z_{th2} = 8.46/-20.57^\circ\ \Omega$$
$$U_{th1} = 49.49/84.4^\circ\ \text{V} \quad U_{th2} = 44.74/-23.3^\circ\ \text{V}$$

subscript *th*1 and *th*2 makes reference to the positive and negative Thévenin equivalents, respectively.

Sequence data of the lines 1 and 2, modeled with mutual coupling, are the following:

$$R_1 = 1.314\,\Omega \quad R_0 = 2.650\,\Omega$$
$$L_1 = 0.0092\,\text{H} \quad L_0 = 0.0354\,\text{H}$$

The THD in voltage waveform (THDV) is generated according to [18] with a maximum value of 5.5% in steady-state conditions, resulting a THD in the current waveform (THDI) of 3.3%. The objectives of the current limits are to limit the maximum individual frequency voltage harmonic to 3% of the fundamental and THDV to 5% for systems without a major parallel resonance at one of the injected harmonic frequencies [18]. The value of each harmonic component of the voltage waveform is shown in Table 1. The planning levels are specified by the electrical utility for all the voltage levels as internal quality objectives. According to reference [19], the THDV limit expected in HV systems must be lower than 3% and for LV and MV systems must be within 6%.

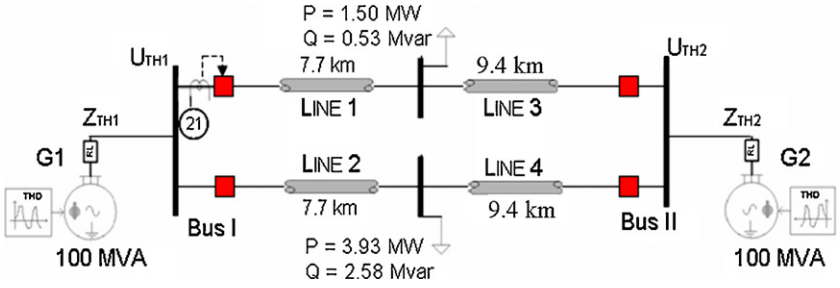


**Fig. 2.** Power system modeled for analyze the behavior of the DEA algorithm.

**Table 1**
Harmonic distortion of the applied voltage waveform in the simulated power system.

| Frequency (Hz) | Harmonic number | Fundamental voltage percent (%) |
|---|---|---|
| 60 | 1 | 100 |
| 120 | 2 | 1.5 |
| 180 | 3 | 2.0 |
| 240 | 4 | 1.5 |
| 300 | 5 | 2.0 |
| 420 | 7 | 2.0 |
| 540 | 9 | 1.5 |
| 660 | 11 | 1.5 |
| 780 | 13 | 1.5 |
| 1020 | 17 | 1.0 |
| 1140 | 19 | 1.0 |

### 3.2. Behavior of the DEA algorithm against harmonic distortion

Fig. 3 shows the reactance estimated by DEA when a SLG fault occurs at instant $t = 0.087$ s and at 25% of the protected line length, without considering harmonic distortion and fault resistance. Otherwise, Fig. 4 depicts the reactance estimated for the same fault, considering harmonic distortion and fault resistance. The value is assumed stable when its variation is within ±0.001 pu.

As it can be seen in Fig. 4, it is difficult to determine the fault distance since its value is in an intermittent state. This is because a periodic deformation takes place in the determinant expressed in (17) when there is harmonic distortion.

Fig. 5 shows the determinant for the fault case where no harmonic distortion was included. Otherwise, Fig. 6 shows the determinant in case of harmonic distortion. Note that a periodic deformation with a $T_{DEF}$ period can be appreciated. In the time $\Delta t_1$ appears the maximum disturbance which leads to a highly uncertain and misleading estimated value.

## 4. Filtering application for DEA algorithm

### 4.1. Description of the filter design

The fundamental presumption considered for the filter design is that the peak value relation between the fundamental frequency component and the harmonic waveform remains equal in both prefault and fault state. In steady-state conditions, the filter determines the peak value and phase angle of the waveforms of voltage and current, applying a Fast Fourier Transform (FFT) [20]. These quantities are computed and refreshed every cycle.

### 4.2. Waveform estimated for voltage fundamental component

The voltage waveform with harmonic distortion is expressed by the following continuous-time equation:

$$u(t) = U_{peak\_1} \sin(\omega t - \phi_1) + \sum_{h=2}^{50} U_{peak\_h} \sin(h\omega t - \phi_h) \quad (18)$$

where $\omega$ is the fundamental frequency, $U_{peak\_1}$ and $\phi_1$ are the amplitude and phase angle of the fundamental voltage waveform,

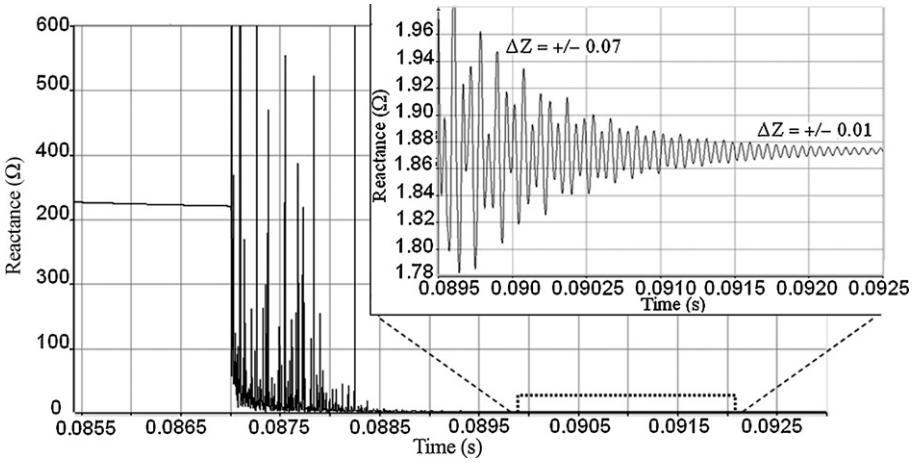


**Fig. 3.** Reactance estimated by DEA without considering harmonic distortion, fault is at 25% of line length.

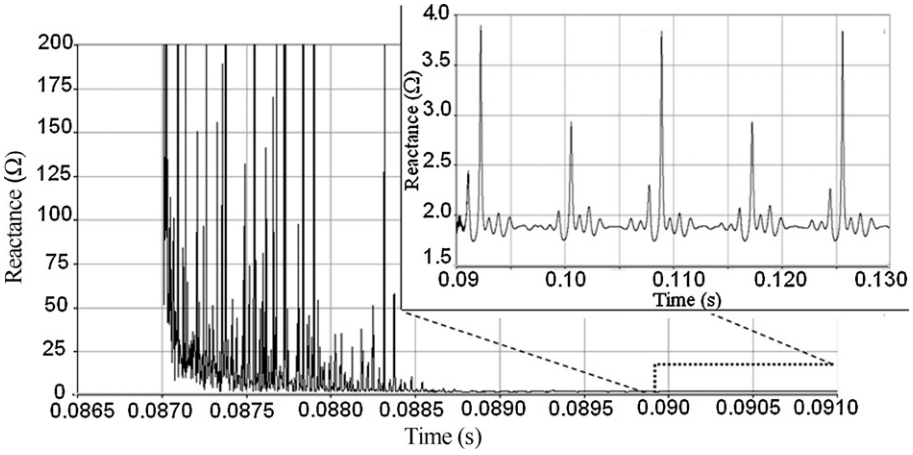


**Fig. 4.** Reactance estimated by DEA considering harmonic distortion, fault is at 25% of line length.

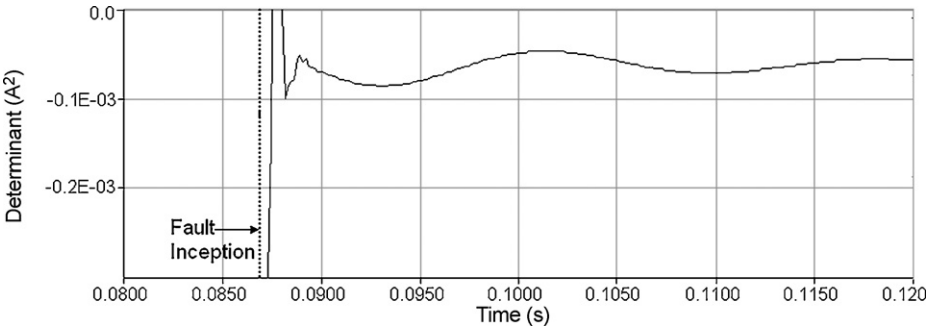


**Fig. 5.** Determinant of DEA without including harmonic distortion.

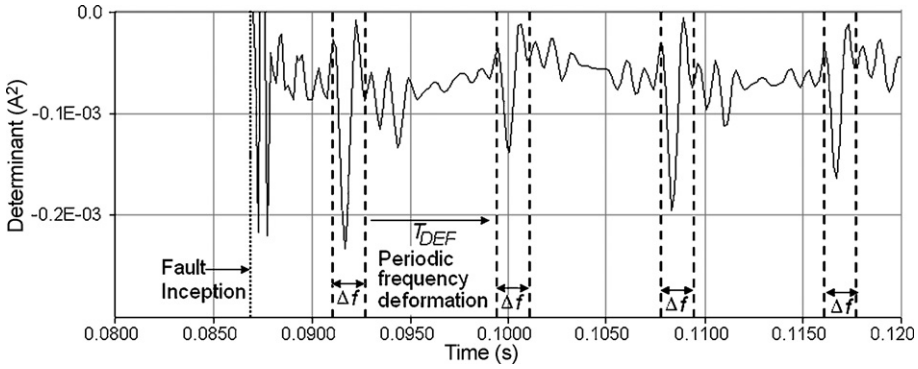


**Fig. 6.** Determinant of DEA including harmonic distortion, periodic frequency deformation is appreciates and fault is at 25% of line length.

respectively, and $U_{peak\_h}$ and $\phi_h$ are the amplitude and phase angle belonging to the $h$-th harmonic component. It is assumed that the highest number of harmonic component in study is the order 50. The effective magnitude $U_{effec}$ of the voltage waveform $u(t)$ given by (18) is determined as:

$$U_{effect} = \frac{U_{peak}}{\sqrt{2}} = \sqrt{\sum_{h=1}^{50}\left(\frac{U_{peak\_h}}{\sqrt{2}}\right)^2} \tag{19}$$

Using (19), a relation factor $F^u$ is determined to relate the peak value of each component, $U_{peak\_h}$, with the apparent peak value, $U_{peak}$, of the voltage waveform. These relation factors $F^u$ are calculated by:

$$F^u = \begin{bmatrix} F_1^u \\ \vdots \\ F_{50}^u \end{bmatrix} = \begin{bmatrix} U_{peak\_1} \\ \vdots \\ U_{peak\_50} \end{bmatrix} \frac{1}{U_{peak}} \tag{20}$$

According to the presumption considered, after fault inception, these relation factors are similar to those computed one cycle earlier. Thus, using (20) the peak voltage value during fault conditions $U_{peak}^f$ can be estimated from the voltage waveform $u^f(t)$ as follows:

$$u^f(t) = F_1^u U_{peak}^f \sin(\omega t - \phi_1^f) + \sum_{h=2}^{50} F_h^u U_{peak}^f \sin(h\omega t - \phi_h^f) \tag{21}$$

Being the peak value $U_{peak}^f$ of the voltage waveform $u^f(t)$ an unknown parameter. For voltage waveforms, the changes that experiment the phase angle after fault inception are negligible. Therefore, $\phi_1^f$ can be assumed similar to the prefault value of $\phi_1$. Hence, $U_{peak}^f$ is determined as follows:

$$U_{peak}^f = \frac{u^f(t)}{F_1^u \sin(\omega t - \phi_1) + \sum_{h=2}^{50} F_h^u \sin(h\omega t - \phi_h)} \tag{22}$$

Therefore, the output of the proposed filter represents the fundamental voltage waveform of (18) and is it expressed by the

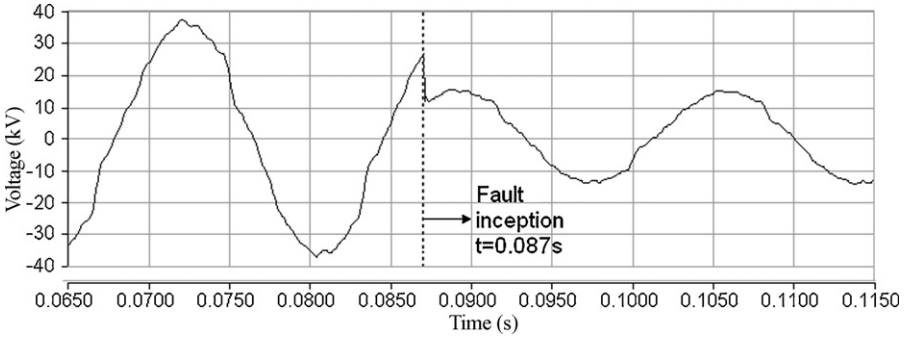


**Fig. 7.** Voltage waveform at bus 1 of the power system modeled, fault is at 25% of line length.

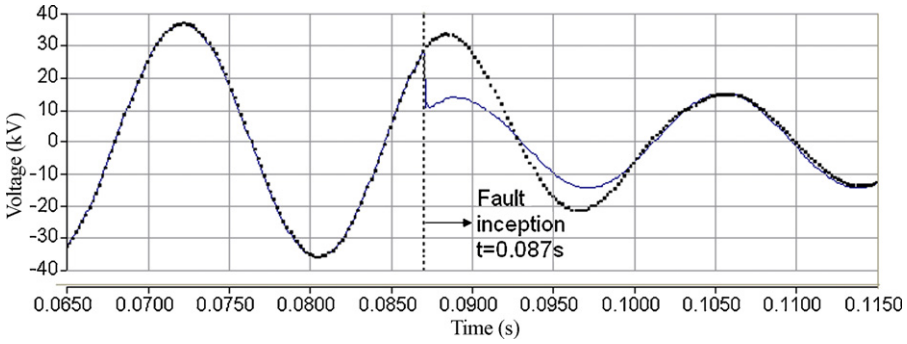


**Fig. 8.** Voltage fundamental component waveform computed by the filter proposed (solid line) and FFT (points).

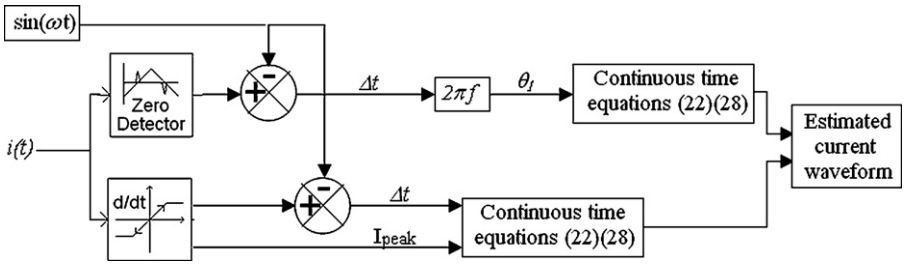


**Fig. 9.** Block diagram of the control system modeled for estimating current fundamental component waveform.

following continuous-time equation:

$$u_{filter\_out}(t) = F_1^u U_{peak}^f \sin(\omega t + \phi_1^f) \tag{23}$$

where $u_{filter\_out}(t)$ is the filtered voltage waveform generated by the proposed filter to be processed by the DEA algorithm.

Fig. 7 shows the voltage waveform at bus 1 of the power system shown in Fig. 2. A SLG fault is applied at 25% of line length and at instant $t = 0.087$ s, considering a fault resistance of 0.01 Ω. Fig. 8 depicts the voltage fundamental component waveform computed by the proposed filter (solid line) and by FFT (points). The performance of the proposed filter leads to an estimated voltage waveform 0.68 cycles faster than the FFT and with a magnitude error of less than 0.1%.

### 4.3. Waveform estimated for current fundamental component

After fault inception, a phase jump in current waveform is possible. Therefore, the current waveform can change in phase position with respect to prefault conditions. Hence, correct estimation of magnitude and phase are important to improve the performance of numerical differentiation in (15) and (16). In steady-state conditions, the parameters of the current waveform are determined in the same way as in (19) and (20). This is:

$$i(t) = I_{peak\_1} \sin(\omega t - \theta_1) + \sum_{h=2}^{50} I_{peak\_h} \sin(h\omega t - \theta_h) \tag{24}$$

where, $\theta_1$ and $\theta_h$ are the phase angles related to the fundamental and $h$-th current harmonic component, respectively. The apparent peak value $I_{peak}$ of current waveform in steady-state conditions is determined by the following expression:

$$I_{effec} = \frac{I_{peak}}{\sqrt{2}} = \sqrt{\sum_{h=1}^{50} \left(\frac{I_{peak\_h}}{\sqrt{2}}\right)^2} \tag{25}$$

Then relation factor $F^c$ is calculated for the current waveform as follows:

$$F^c = \begin{bmatrix} F_1^c \\ \vdots \\ F_{50}^c \end{bmatrix} = \begin{bmatrix} I_{peak\_1} \\ \vdots \\ I_{peak\_50} \end{bmatrix} \cdot \frac{1}{I_{peak}} \tag{26}$$

As $\theta_h$ and $I_{peak}$ changes when fault occurs, they are considered unknown parameters. Therefore, a control system has been implemented to determine these parameters. The task of this algorithm is to detect the zero crossing or differential sign variations of the measured current waveform. The control system considered is shown in Fig. 9, where the reference signal is based on a fundamental component sinewave without angle phase.

The instantaneous current $i^f(t)$ during fault conditions can be expressed as:

$$i^f(t) = F_1^c I_{peak}^f \sin(\omega t - \theta_1^f) + \sum_{h=2}^{50} F_h^c I_{peak}^f \sin(h\omega t - \theta_h^f) \tag{27}$$

Expanding (27), the following expression is obtained:

$$i^f(t) = I_{peak}^f F_1^c(\cos(\theta_1^f)\sin(\omega t) - \sin(\theta_1^f)\cos(\omega t)) + I_{peak}^f \sum_{h=2}^{50} F_h^c(\cos(\theta_h^f)\sin(h\omega t) - \sin(\theta_h^f)\cos(h\omega t)) \tag{28}$$

A suitable way for solving (28) is considering 50 samples in different instants of time and solving for $\theta_h^f$ by using linear programming algorithms.

However, for power systems with a THDI lower than 7%, it is observed that fundamental harmonic contribution to faults is higher than the contribution of the rest of harmonics. This is $F_1^c \gg F_h^c$ for $h = 2, 3, \ldots, 50$. Thus, harmonic contribution to faults can be considered relatively negligible in comparison with the fundamental harmonic. This presumption simplifies broadly the solution of (28) by assuming that in fault conditions $\theta_1^f \cong \theta^f$, where $\theta^f$ is the phase angle of the measured current waveform during fault conditions.

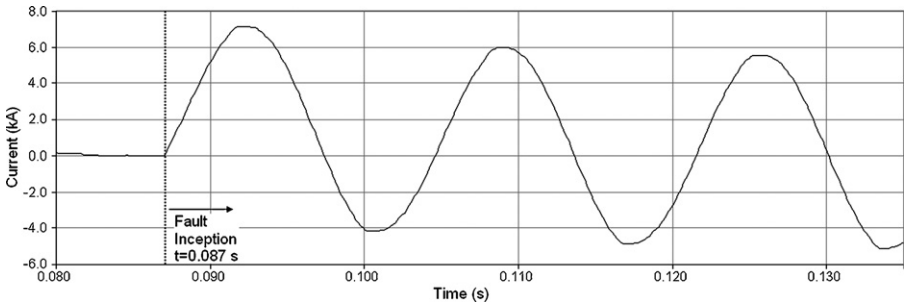


**Fig. 10.** Current waveform at bus 1 of the power system modeled, fault is at 25% of line length.

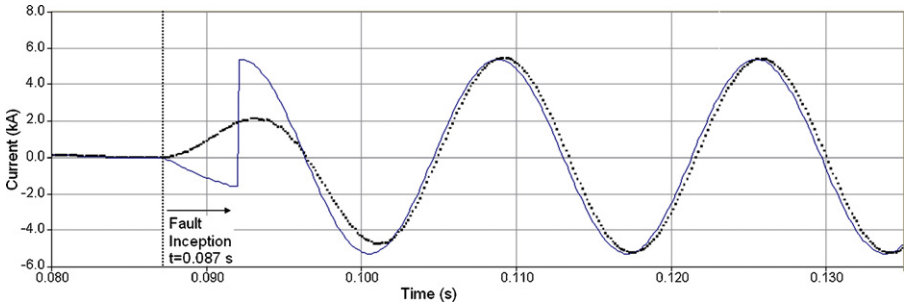


**Fig. 11.** Current fundamental component waveform computed by the filter design (solid line) and FFT (points).

The presumption used ($\theta_1 \cong \theta^f$) has been checked for several THDI. For the cases when THDI of the power system is greater than 10% or during the energization of power transformers and transmission lines, the presumption considered becomes pointless and misleading for accurate operation. To avoid misoperation of the algorithm during these events, a harmonic blocking function must be included in order to operate using conventional Fourier algorithms.

Subsequently, when the algorithm detects a zero crossing, the phase angle, $\theta^f$, will be the difference between the reference signal ($\sin \omega t$) and the current waveform measured. Therefore, the peak value is estimated by means of (28) as follows:

$$I^f_{peak} = \frac{i^f(t)}{F^c_1(\cos(\theta^f_1)\sin(\omega t) - \sin(\theta^f_1)\cos(\omega t))} \tag{29}$$

Otherwise, if the waveform reaches its peak value before the detection of a zero crossing, the magnitude $I^f_{peak}$ is computed. Then, $I^f_{peak}$ is a known parameter and the phase angle $\theta^f_1$ is estimated from (28) by considering two samples at instants $t$ and $t + \Delta t$, and solving for $\theta^f_1$ as follows:

$$\theta^f_1 = \arcsin\left(\frac{1}{F^c_1 \cdot I^f_{peak}} \cdot \frac{\tan(\omega t)}{\sin(\omega(t+\Delta t)) - \cos(\omega(t+\Delta t)) \cdot \tan(\omega(t+\Delta t))} \cdot \left(i^f(t+\Delta t) - \frac{\sin(\omega(t+\Delta t))}{\sin(\omega t)} \cdot i^f(t)\right)\right) \tag{30}$$

Since cancellation of the DC component is not possible for all faults by the auxiliaries CT [21], the algorithm gets from a memory stack the measurement of the last 0.25 cycles. Next, the peak detection is compared with the last 1/4 measurements to subtract the DC component effect.

Once determined both parameters $\theta^f_1$ and $I^f_{peak}$, the proposed filter generates the estimated current waveform expressed as:

$$i_{filter\_out}(t) = F^c_1 I^f_{peak} \sin(\omega t - \theta^f_1) \tag{31}$$

where $i_{filter\_out}(t)$ is the filtered current waveform generated by the proposed filter to be processed by the DEA algorithm.

In Fig. 10, the measured current waveform at bus 1 of the power system modeled is shown. Fault is at 25% of line length without considering fault resistance. Fig. 11 shows the current waveform computed by the proposed filter (solid line) and by FFT (points). The performance of the proposed filter points to an estimated waveform at least 0.54 cycles faster than the FFT and with a magnitude and phase angle difference of less than 0.5%.

## 5. Results and discussion

The behavior of DEA algorithm using the proposed filtering application is analyzed by comparing the simulation results with both theoretical values and conventional DEA algorithm. The lowest accurate performance of DEA algorithm is appreciated in SLG faults. Thus, the behavior of the algorithm using this filtering application is presented by analyzing the accuracy, time response and influence of the fault inception angle against SLG faults on the power system of Fig. 2. For double phase and three phase faults, the DEA seems less affected by harmonic distortion. Nonetheless, errors in the estimation are still considerable and therefore are reduced by using the filtering application.

### 5.1. Accuracy of the algorithm

The accuracy of the DEA algorithm with the proposed filter incorporated is simulated and analyzed for different faults applied at different lengths of the protected line. Moreover, fault resistance takes values of 0, 5 and 10 Ω for each simulation. Table 2 shows the results of fault distance estimated by the DEA algorithm considering an inception angle of 60°. The waveforms of voltage and current estimated by the filter improve the convergence time of the DEA algorithm. Also, the values of impedance and distance estimated are more accurate.

**Table 2**
Errors in the estimated fault distance varying fault location and resistance.

| Fault distance (%) | Fault resistance (Ω) | Filter-DEA algorithm | | DEA algorithm | |
|---|---|---|---|---|---|
| | | Error (%) | Distance (pu) | Error (%) | Distance (pu) |
| 25 | 0 | 0.638 | 0.2564 | 1.97 | 0.2697 |
| | 5 | 0.657 | 0.2434 | 20.44 | 0.4544 |
| | 10 | 0.331 | 0.2533 | 60.38 | 0.8538 |
| 50 | 0 | 0.221 | 0.5022 | 3.83 | 0.5383 |
| | 5 | 0.567 | 0.4943 | 30.36 | 0.8036 |
| | 10 | 4.775 | 0.5478 | 82.25 | 1.3225 |
| 75 | 0 | 1.145 | 0.7615 | 7.14 | 0.8214 |
| | 5 | 0.999 | 0.7400 | 43.09 | 1.1809 |
| | 10 | 14.808 | 0.8981 | 109.85 | 1.8485 |
| 100 | 0 | 2.408 | 1.0241 | 12.41 | 1.1241 |
| | 5 | 5.377 | 1.0538 | 59.40 | 1.5940 |
| | 10 | 8.091 | 0.9191 | 81.30 | 1.8130 |


**Fig. 12.** Comparison of the distance errors by DEA using filtering application (solid lines) and without (dashed lines) for 5 and 10 Ω fault resistance simulation.

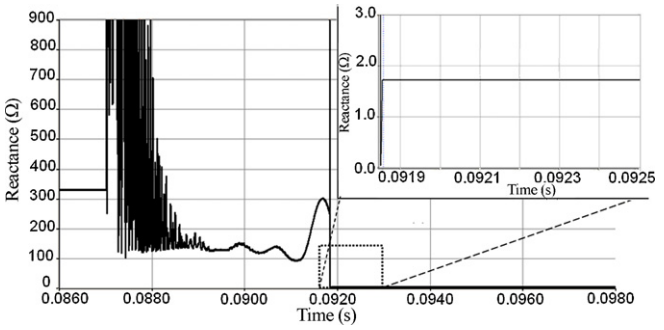


**Fig. 13.** Behavior of DEA algorithm with filtering application considering harmonic distortion, fault is at 25% of line length.

As it can be appreciate in Fig. 12, for a fault with 5 and 10 Ω fault resistances, the distance error using the proposed filter is reduced in a 56% in comparison with the DEA without filter.

### 5.2. Response time of the algorithm

Fig. 13 shows the convergence behavior of DEA algorithm with the proposed filter for a SLG fault at instant $t = 0.087$ s. The algorithm converges to a non-variation value even considering fault resistance. This is because the determinant (17) remains constant once fundamental waveforms of current and voltage are estimated. Thus, response time is slightly faster than DEA without filter because of the time required for convergence.

Fig. 14 shows the convergence time of the DEA algorithm with and without the proposed filter for SLG faults in the protected line. The DEA algorithm without the proposed filter has higher response time because of the DC component that introduces more oscillations during the value estimation.

The response time of Fourier techniques algorithms [22] is close to 46 ms with 5% of error in the estimated value. Under this scope, DEA algorithm offers a fast and accurate protection for faults with low fault resistance.

**Table 3**
Errors in the estimated fault distance varying fault location, resistance and inception angle.

| Fault distance (%) | Fault resistance (Ω) | Filter-DEA algorithm | | | | | |
|---|---|---|---|---|---|---|---|
| | | 30° | | 60° | | 90° | |
| | | Distance error (%) | Response time (%) | Distance error (%) | Response time (%) | Distance error (%) | Response time (%) |
| 25 | 0 | 0.62 | 0.0053 | 0.638 | 0.0067 | 1.25 | 0.0078 |
| | 5 | 1.55 | 0.0043 | 0.657 | 0.004 | 0.33 | 0.0057 |
| | 10 | 2.08 | 0.0033 | 0.331 | 0.004 | 2.05 | 0.0057 |
| 50 | 0 | 3.78 | 0.0052 | 0.221 | 0.0062 | 1.13 | 0.0078 |
| | 5 | 4.11 | 0.0045 | 0.567 | 0.005 | 0.85 | 0.007 |
| | 10 | 5.79 | 0.0041 | 4.775 | 0.0041 | 2.98 | 0.007 |
| 75 | 0 | 4.26 | 0.0052 | 1.145 | 0.0062 | 4.03 | 0.008 |
| | 5 | 7.13 | 0.0042 | 0.999 | 0.0048 | −3.07 | 0.007 |
| | 10 | 10.44 | 0.004 | 14.808 | 0.0048 | 7.35 | 0.007 |
| 100 | 0 | 6.17 | 0.005 | 2.408 | 0.005 | 2.96 | 0.005 |
| | 5 | 4.44 | 0.0048 | 5.377 | 0.0042 | 9.79 | 0.0042 |
| | 10 | 16.67 | 0.0049 | 8.091 | 0.0034 | 11.34 | 0.0034 |

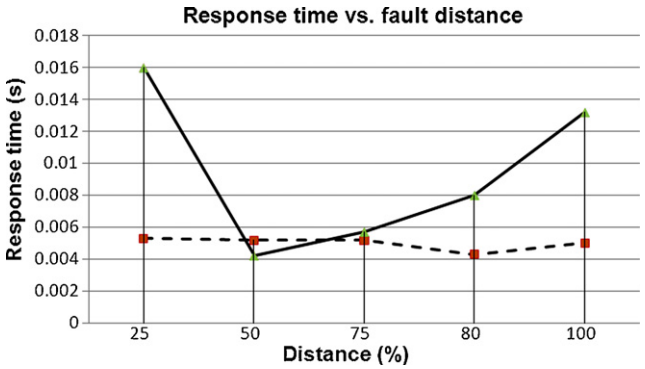


**Fig. 14.** Response time of DEA with filtering application (dashed line) and without (solid line) against SLG faults.

### 5.3. Influence of the fault inception angle in the response of the algorithms

Table 3 shows the errors obtained in the computation of the distance for different fault inception angles. The fault angles considered are 30°, 60°and 90° of the voltage wave for phase a. The fault distance is 50% of the total length. In this table it is observed that the accuracy and response time of the algorithm varies lightly against fault inception angle variations.

## 6. Conclusion

When harmonic distortion and fault resistance exist, the behavior of DEA algorithm without filter is uncertain and misleading for fault distance estimating.

The proposed filter based on continuous-time equations is suitable to improve DEA performance in estimating fault distance considering harmonic distortion and fault resistance. The convergence times are within 0.32 cycles. The theoretical limitation presented by the proposed filter is the accuracy of the algorithm against faults with high fault resistance and with high harmonic distortion.

Applying filtering techniques to achieve voltage and current fundamental waveforms enables DEA to achieve a non-variable convergence value for improving accuracy in fault distance estimation.

## Acknowledgment

The authors would like to thank the Spanish Ministry of Science and Innovation for their support throughout this research under the CICYT program contract number ENE2007-6803.

## Appendix A. List of symbols

$u_a, u_b, u_c$ voltage phases quantities (V)
$i_a, i_b, i_c$ current phases quantities (A)
$k_r, k_l$ relative line length of resistive and inductive part, respectively
$R$ resistance matrix for a transmission line (Ω)
$L$ inductance matrix for a transmission line (H)
$R_1$, $R_2$, $R_0$ resistance of positive, negative and zero sequence, respectively (Ω)
$L_1$, $L_2$, $L_0$ inductance of positive, negative and zero sequence, respectively (H)
$R_s, R_m$ self and mutual resistance for a transmission line (Ω)
$L_s, L_m$ self and mutual inductance for a transmission line (H)
$n$ index of time of the sample
$\sigma$ frequency sampling of the protective device (Hz)
$i_r, i_l$ resistive and inductive current, respectively (A)
$U_{th1}$, $U_{th2}$ Thévenin equivalent voltages of positive and negative sequences, respectively (V)
$Z_{th1}, Z_{th2}$ Thévenin equivalent impedances of positive and negative sequences, respectively (Ω)
$HV$ high voltage systems
$THD$ total harmonic distortion
$THDI$ total harmonic distortion in current waveform
$THDV$ total harmonic distortion in voltage waveform
$h$ subscript for the harmonic component order.
$U_{peak\_h}$ peak voltage of the $h$-th voltage harmonic component (V)
$U_{effec}$ effective voltage (V)
$I_{effec}$ effective current (A)
$U^f_{peak}$ peak voltage estimated during fault (V)
$u^f(t)$ voltage value during fault condition
$I_{peak\_h}$ peak current of the $h$-th current harmonic component (A)
$F^u_h$ relation factor between peak voltage of the $h$-th voltage harmonic component and the effective voltage in steady state
$F^c_h$ relation factor between peak current of the $h$-th current harmonic component and the effective current in steady state
$u_{filter\_out}(t)$ filtered voltage waveform generated by the proposed filter
$i_{filter\_out}(t)$ filtered current waveform generated by the proposed filter

## References

[1] C.-S. Yu, A discrete Fourier transform-based adaptive mimic phasor estimator for distance relaying applications, IEEE Transactions on Power Delivery 21 (4) (2006) 3387–3395.
[2] A.H. Osman, O.P. Malik, Transmission line distance protection based on wavelet transform, IEEE Transactions on Power Delivery 19 (2) (2004) 515–523.
[3] M. Silva, M. Oleskovicz, D.V. Coury, A fault locator for transmission lines using traveling waves and wavelet transform theory, in: Proceedings of the Eighth IEE International Conference on Developments in Power System Protection, IEE, vol. 1, 2004, pp. 212–215.
[4] D. Chanda, N.K. Kishore, A.K. Sinka, A wavelet multiresolution analysis for location of faults on transmission lines, International Journal of Electrical Power & Energy Systems 25 (1) (2003) 59–69.
[5] M. Akke, J.S. Thorp, Some improvements in the three-phase differential equation algorithm for fast transmission line protection, IEEE Transactions on Power Delivery 13 (1) (1998) 66–72.
[6] L.F. Santos, P.M. Silveira, Evaluation of numerical distance protection algorithms for series compensated transmission lines, in: Proceedings of the Transmission & Distribution Conference and Exposition, TDC '06, Latin America, IEEE/PES, 15–18 August, 2006, pp. 1–6.
[7] E. Rosoxllowskia, J. Iżykowskia, B. Kasztennya, M.M. Sahab, A new distance relaying algorithm based on complex differential equation for symmetrical components, Electric Power Systems Research 40 (3) (1997) 175–180.
[8] M. Akke, J.S. Thorp, Improved estimates from the differential equation algorithm by median post-filtering, Developments in power system protection, Proceedings of the Sixth International Conference on Developments in Power System Protection, Publication No. 434, 25–27 March (1997), pp. 235–238.
[9] M. García-Gracia, W. Osal, M.P. Comech, Line protection based on the differential equation algorithm using mutual coupling, Electric Power Systems Research 77 (5–6) (2007) 566–573.
[10] Hsiung Cheng Lin, Intelligent neural network-based fast power system harmonic detection, IEEE Transactions on Industrial Electronics 54 (1) (2007) 43–52.
[11] W.M. Al-Hasawi, K.M. El-Naggar, New digital filter for unbalance distorted current and voltage estimation in power systems, Electric Power Systems Research 78 (7) (2008) 1290–1301.
[12] L. Qian, D. Cartes, Q. Zhang, Three-phase harmonic selective active filter using multiple adaptive feed forward cancellation method, in: Proceedings of the 5th International Power Electronics and Motion Control Conference, vol. 2, 14–16 August, 2006, pp. 1–5.
[13] K. Kennedy, G. Lightbody, R. Yacamini, M. Murray, J. Kennedy, Development of a network-wide harmonic control scheme using an active filter, IEEE Transactions on Power Delivery 22 (3) (2007) 1847–1856.
[14] R. Mahanty, A.K. Kapoor, Quasi-passive filter for harmonic filtering, Electric Power Systems Research 78 (8) (2008) 1456–1465.

[15] M.M. Begovic, P.M. Djuric, S. Dunlap, A.G. Phadke, Frequency tracking in power networks in the presence of harmonics power delivery, IEEE Transactions on Power Delivery 8 (2) (1993) 480–486.
[16] PSCAD v4.2, Manitoba HVDC Research Centre, 2006.
[17] H.W. Dommel, Digital computer solution of electromagnetic transients in single-and multiphase networks, IEEE Transactions on Power Apparatus and Systems PAS-4 (1969) 388–399.
[18] IEEE Recommend Practices and Requirements for Harmonic Control in Electrical Power Systems, IEEE Std. 519-1992, 1992, pp. 55–88.
[19] International Electrotechnical Commission, Assessment of emission limits for distorting loads in MV and HV power systems, Technical Report IEC 61000-3-7 - Electromagnetic Compatibility (EMC), Part 3, Section 6, 2006, pp. 12–59.
[20] P. Duhamel, M. Vetterli, Fast Fourier transforms: a tutorial review and a state of the art, Signal Processing 19 (1990) 259–299.
[21] J. Barry, I.F. Morrison, Digital calculation of impedance for transmission line protection, IEEE Transactions on Power Apparatus and Systems PAS-90 (1971) 270–276.
[22] D. D'Amore, A. Ferrero, A simplified algorithm for digital distance protection based on Fourier techniques, IEEE Transactions on Power Delivery 4 (1) (1989) 157–164.

*Miguel García-Gracia* was born in Saint-Brieuc, France on April 23, 1963. He received his B.S. (1986), M.Sc. (1989), and Ph.D. (1996) degrees from the University of Zaragoza. He is presently Lecturer of Electrical Engineering and Area Director of Electric Power System at Circe. His main research interests are in the field of power system, power system protection, electrical energy system, renewable energy integration, lightning protections and dielectrics.

*N. El Halabi* received the Electrical Engineering degree in 2006 from Universidad Simón Bolívar, Venezuela. He is currently performing the Ph.D. in Renewable Energy at Universidad de Zaragoza, Spain. His research interests are Power system protection, integration and planning of hybrid power systems.

*Antonio Montañés* received his M.S. (2003) degree from the University of Zaragoza. He is presently Lecturer of Electrical Engineering, University of Zaragoza. His fields of interest include protective relaying, and fault location in transmission line, and he is presently continuing his work towards a PhD in the area of fault location in distribution systems.

*H.M. Khodr* received the Ph.D., M.Sc., and Engineer degrees in electrical engineering from the José Antonio Echeverría Higher Polytechnic Institute (ISPJAE), Havana, Cuba, in 1997 and 1993, respectively. He is a former Associate Professor of electrical engineering at Universidad Simón Bolívar, Caracas, Venezuela. He was a Researcher at INESC Porto, Porto, Portugal. Presently, he is a Researcher at GECAD, Porto. He has participated in a number of projects performed for the local industries. His current research activities are concentrated on planning, operation, and economics of electrical distribution and industrial power systems; electricity market; grounding systems; and optimization.

*M. Villén* received her B.S. (2002) and M.Sc. (2008) degrees in Industrial Engineering from the University of Zaragoza. She is currently performing the Ph.D. in Electric Power Systems at the University of Zaragoza. Her research interests are modeling Electrical machines and Relaying systems.

# Anexo C. Artículos aceptados con cambios relacionados con la implementación en los algoritmos de distancia del esquema adaptativo basado en el salto de fase en la corriente

# Adaptive Distance Relaying Scheme Based on Current Phase Jump Correction Factor

M. García-Gracia, N. El Halabi, S. Martín Arroyo and H.M. Khodr, *Member, IEEE*

***Abstract*— This paper proposes an adaptive distance relaying scheme based on the current phase jump behavior during fault conditions to improve the apparent impedance estimated by the relay. For a nonpilot protection scheme, the measured impedance is affected by error due to the combined effects of fault resistance and prefault load. An experimental relation between the current phase jump introduced with fault inception and the X/R ratio seen by the distance protection is deduced. The phase jump correction factor obtained is an exponential function of the *X/R* ratio of the line. This factor is applied to the apparent impedance measured by the relay and it allows mitigating the adverse effect of prefault power. The adaptive scheme improves significantly the accuracy in estimation of the resistive fault location. The application of this scheme does not require communication links from the remote end of line and is applicable to all types of fault.**

***Index Terms*—Adaptive scheme, distance protection, impedance locus, fault resistance, prefault load, current phase jump.**

## I. Introduction

NONPILOT distance relays remain susceptible to malfunction under a wide range of power system operating conditions. This is because protection function is provided with voltage and current signals only from one end of the protected circuit, and is expected to assess the location of a fault on the basis of these locally derived signals [1].

Many parameters such as ground fault resistance, prefault system conditions, mutual effects of parallel lines and shunt capacitance influences exert an important influence on the distance measurement process, and not surprisingly, several sources of error are present when estimating the impedance seen at the relay location [2]. These limitations of nonpilot distance relays have been acknowledged for a long time [3], [4] and lead the traditional distance relaying approach to experience underreach and overreach problems.

Adaptive protection concept became an attractive possibility due to the advancement of computers, communication systems and software developments. The adaptive protection is defined as a protection philosophy that modifies the preferred protective response in order to make them more attuned to prevailing power system conditions [5].

This work was supported in part by the Ministry of Science and Innovation of Spain under CYCIT Grant ENE2007-6803.

M. García-Gracia, N. El Halabi and S. Martín are with Energy and Resource Consumption Investigation Centre (CIRCE), Zaragoza, 50018, Spain (phone: +34 976 761923; fax: +34 976 762226; e-mail: nabileh@unizar.es).

H.M. Khodr is with the GECAD-Polytechnic Institute of Porto (ISEP/IPP), Porto 4200-072, Portugal (e-mail: hmk@isep.ipp.pt).

In particular, adaptive methods applied in distance relaying have been focused mainly to improve fault location and response time by mitigating the adverse effect of frequency variation, fault resistance, dc component, X/R source ratio, mutual couplings and prefault power condition over the apparent impedance estimated by the relay.

In [6] an adaptive concept based on processing harmonic data from voltage waveform is presented to improve fault distance location, while [7] presents a recursive Fourier filtering technique to remove the decaying dc offset component from fault signals for accelerating the response of the relay. Likewise [8] develops an adaptive discrete Fourier transform-based mimic filter to approximate the decaying dc time constant from voltage and current measurement to achieve higher accuracy on the estimated impedance.

Other adaptive concepts are oriented to use a compensating factor that modifies the characteristic of the distance protection to improve the estimated apparent impedance and to increment security in high speed distance protection [9]-[11]. Latest adaptive concepts are being based on neural and agent technologies [11]-[14] to increment the accuracy of apparent impedance estimation.

These adaptive techniques achieve significant improvement in the accuracy, security and dependability of the distance protection algorithm. However, most of them require an intensively learning pattern for different training sets corresponding to different parameters of the power system.

This paper presents an adaptive distance relaying scheme based on the current phase jump data during fault conditions to determine a correction factor applied to the apparent impedance seen by the relay. The correction factor used is found to be an exponential function of the *X/R* ratio of the line. This is an experimental relation between the current phase jump introduced with fault inception and the *X/R* ratio seen by the distance protection. The factor is applied to the apparent impedance in order to increase the accuracy in the estimation of the apparent impedance measured by the relay.

To verify the proposed adaptive scheme, detailed analyses of the apparent impedance seen by the relay have been performed, taking into account mutual coupling, prefault condition, fault resistance, fault angle inception and *X/R* ratio.

The algorithm presented modifies the *X/R* ratio seen by the relay according to the current phase jump once fault occurs. Then, by means of the jump corrective factor, *JCF*, determined by an empirical *X/R* ratio vs. current phase jump curve, the algorithm mitigates the adverse effect of fault resistance over the apparent impedance locus and calculates an improved fault location within the protected line. The

application of this scheme does not require communication links with the remote terminal of the protected line.

Simulations have been performed for single line to ground faults and evaluated with both adaptive schemes based of Discrete Fast Fourier Transform (DFFT) algorithm [7], [8] and neural network [11] to highlight the effectiveness and accuracy achieved by the new proposed adaptive scheme.

## II. Influence of Prefault Power Condition on the Apparent Impedance Seen by the Relay

In order to obtain a brief understanding of the influence of system load on fault currents and voltages, it is helpful to perform a fault study on the system shown at Fig. 1 for a single line to ground (SLG) fault. The effective voltage and current phasors at a relay location during healthy system load conditions are denoted by $V_L$, $I_L$ respectively. The ratio of these two signals gives the corresponding load apparent impedance seen from the relay location in stable conditions and is denoted as $Z_{LL}=V_L/I_L$.

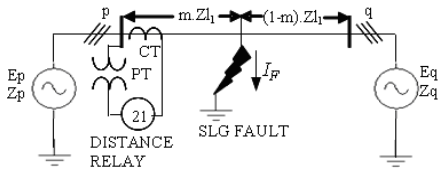


Fig. 1. System arrangement for a SLG fault study case.

Following a SLG fault inception at phase *a* and solving the equivalent sequence networks circuit leads to an evaluation of the fault current $I_r$ seen by the relay at phase *a*. The influence of prefault load current $I_L$ is taken into account using the superposition theorem. Therefore, the fault current $I_r$ is represented by two terms [3] as follows

$$I_r = \psi \cdot I_F + I_L \tag{1}$$

being $I_F$ the total current at the fault point, and is determined as follows

$$I_F = \frac{V_L - I_L \cdot m \cdot Zl_1}{\psi \cdot Z_F + 2 \cdot C_1 \cdot Z_{p1} + C_0 \cdot Z_{p0}} \tag{2}$$

where $Z_{p1}$ and $Z_{p0}$ are the positive and zero sequence equivalent source impedance of bus *p*, respectively, $Zl_1$ is the positive sequence impedance of the line and *m* is the distance to fault. $Z_F$ is the apparent impedance of the fault path and is equivalent to

$$Z_F = m \cdot Zl_1 + \frac{3 \cdot R_F}{\psi} \tag{3}$$

being $R_F$ the fault resistance.

The factors $\psi$, $C_1$ and $C_0$ are constants for a given system arrangement and denote the distribution factor expressions. The derivation of these factors and of $I_F$ is shown in *Appendix A*.

Then, the voltage equation at the relay location for phase *a* is

$$V_r = m \cdot Zl_1 \cdot (\psi \cdot I_F + I_L) + 3 \cdot R_F \cdot I_F \tag{4}$$

Thus, using voltage and current signals ($V_r$, $I_r$ respectively), the apparent impedance seen by the relay is $Z_r$. The latter impedance can be expressed as a function of $Z_{LL}$ and $R_F$ [3] as follows

$$Z_r = \frac{V_r}{I_r} = Z_{LL} \cdot \frac{3 \cdot R_F + m \cdot Zl_1 \cdot (2 \cdot C_1 + \xi / Z_{LL})}{3 \cdot R_F + 2 \cdot C_1 \cdot Z_{LL} + \xi} \tag{5}$$

where $\xi$ is constant for a given system arrangement and represents the following simplified impedance

$$\xi = 2 \cdot C_1 \cdot Z_{p1} + C_0 \cdot \left( \frac{Zl_0}{Zl_1} + Z_{p0} \right) \tag{6}$$

For a better comprehension of the effect of prefault load in the performance of $Z_r$ it results suitable to represent the locus of a complex variable in an R-X diagram for different prefault load conditions. At [3] a detailed procedure for the construction of this diagram is presented, where prefault load current is considered and the corresponding fault location (as viewed by the relay) is represented by the radius of the circular locus obtained from the argument of (5).

In the R-X diagram shown in Fig. 2, $Z_X$ represents apparent impedance $Z_r$ evaluated at the fault point, considering $R_F$=0. The locus of the apparent impedance for varying $R_F$ represents a circle arc linking the fault location point $Z_X$ and the load point $Z_{LL}$, where the center lies above the segment $\overline{Z_X Z_{LL\_1}}$ for $\theta_F > 0$ ($\theta_F$ inductive) and below the segment $\overline{Z_X Z_{LL\_2}}$ for $\theta_F < 0$ ($\theta_F$ capacitive).

In Fig. 2, $\varphi_l$ denotes the apparent impedance angle of the line, subscripts *1* and *2* refer to the capacitive (exporting power) and inductive (importing power) condition of $\theta_F$, respectively, $\theta_{LL}$ is the load apparent impedance angle and *CN* is the center of the circle for each condition. Note that under exporting power condition of bus *p*, the link path between the fault point and the load point is represented by *P1* and under importing condition by *P2*.

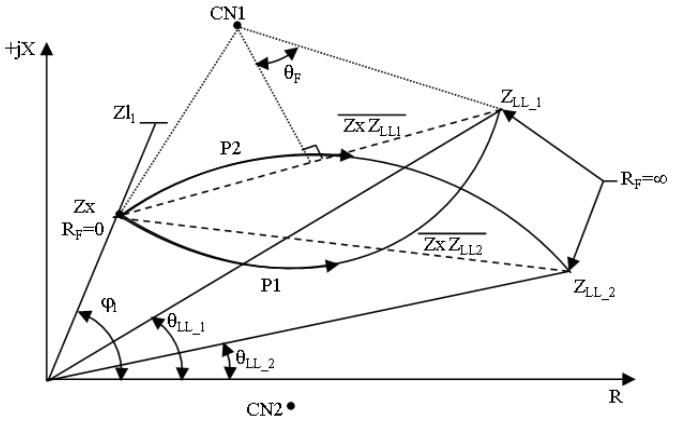


Fig. 2. Locus of measured impedance $Z_r$ for varying $R_F$. P1 represents the path for $\theta_F$ inductive and P2 the pat for $\theta_F$ capacitive.

Thus, the effect of importing power at the relay location is to cause an increase in the apparent impedance estimated by the relay, and results in further underreaching of the protection. An export power condition causes an overreaching tendency which results in a miscoordination between distance protection zones [3], [11].

## III. Relation of Current Phase Jump with Fault Location

The second term in (3) represents the error component in measured impedance due to the combined effects of fault resistance and prefault load and it could only be determined if both system arrangement and fault path impedance are known parameters. However, when considering the operation of distance relays, the current and voltage magnitudes of the receiving terminals are unknown parameters for a nonpilot protection scheme.

Therefore, the magnitude and phase of the total current at fault path $I_F$, shown in Fig. 3, are unknown and the potential rise due to the fault resistance is not considered by the measurement units of the relays for a correct estimation of the apparent impedance to fault. This leads to an error in distance measurement whenever fault resistance is present. The phase and magnitude difference between the components of fault current at the relay location $I^p{}_r$ and the total current in the fault path are shown in Fig. 3.

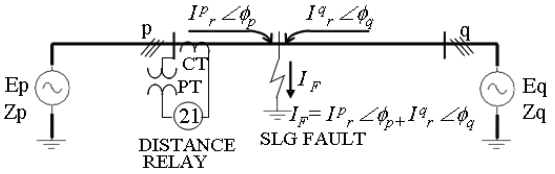


Fig. 3. Magnitude and phase difference between the component of fault current at the relay location and the total current in the fault path.

However, the performance of the current waveform, more precisely, the current phase jump introduced with fault inception is related to the *X/R* ratio seen by the distance protection during fault condition. This study proposes a correction factor based on the current phase jump behavior during fault conditions to mitigate the error component of (3).

The scheme is applicable for all types of fault, and the degree of compensation remains constant for all fault locations within the protected circuit since *X/R* is a constant for a particular line.

The voltage $v_r(t)$ at the relay location, once fault occurs, is of the form

$$v_r(t) = V_m \cdot \sin(\omega t) \tag{7}$$

where the phase jump expected is within 0.2º ~ 0.5º and is considered negligible (Fig. 4). However, the phase jump is significant for the fault current waveform seen by the relay $i_r(t)$, which is given by

$$i_r(t) = I_m \cdot \sin(\omega t - \phi) \tag{8}$$

being $\phi$ the arc tangent of *X/R* seen by the relay during fault condition.

Under prefault conditions, the current waveform $i_L(t)$ is represented by

$$i_L(t) = I_m \cdot \sin(\omega t - \phi_L) \tag{9}$$

where $\phi_L$ is the arc tangent of *X/R* seen by the relay during prefault condition.

Then the phase jump in the current waveform $\Delta\phi$, shown in Fig. 4, is given by

$$\Delta\phi = \arg\left(i_r(t) - i_L(t)\right) = \phi - \phi_L \tag{10}$$

and it is proportional to the argument of the difference between $Z_r$ and $Z_{LL}$, as follows

$$\Delta\phi = \arg\left(Z_r - Z_{LL}\right) \tag{11}$$

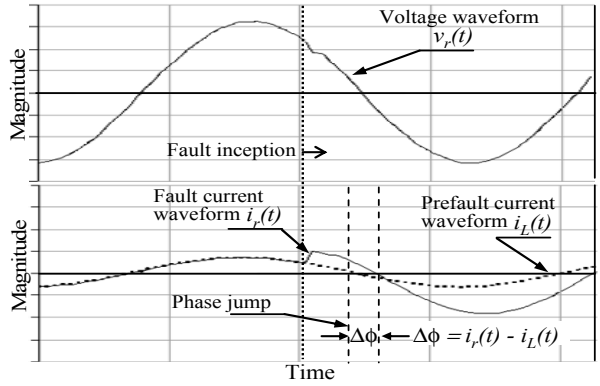


Fig. 4. Phase jump in the current waveform (solid line) with fault inception in comparison with the prefault current waveform (pointed line) and voltage waveform.

Substituting (5) in (11)

$$\Delta\phi = \arg\left( \frac{Z_{LL} \cdot \left( 2 \cdot C_1 \cdot \left(m \cdot Zl_1 - Z_{LL}\right) + \xi \cdot \left( \frac{m \cdot Zl_1}{Z_{LL}} - 1 \right) \right)}{3 \cdot R_F + 2 \cdot C_1 \cdot Z_{LL} + \xi} \right) \tag{12}$$

and simplifying this latter expression the following relation is obtained

$$\Delta\phi = \arg\left( Z_{LL} \cdot \frac{\left(2 \cdot C_1 \cdot Z_{LL} + \xi\right) \cdot \left( \frac{m \cdot Zl_1}{Z_{LL}} - 1 \right)}{3 \cdot R_F + 2 \cdot C_1 \cdot Z_{LL} + \xi} \right) \tag{13}$$

As load impedance is much greater than line impedance, i.e. $Z_{LL} >> m \cdot Zl_1$, the ratio $m \cdot Zl_1 / Z_{LL}$ tends to zero and expression (13) becomes

$$\Delta\phi = 180\,^\circ + \arg\left(Z_{LL}\right) + \arg\left( \frac{\left(2 \cdot C_1 \cdot Z_{LL} + \xi\right)}{3 \cdot R_F + 2 \cdot C_1 \cdot Z_{LL} + \xi} \right) \tag{14}$$

Eq. (14) shows that $\Delta\phi$ contains data of both the effect of prefault conditions ($Z_{LL}$) and fault resistance ($R_F$).

## IV. Power System Simulations

The power system considered for this study is shown in Fig. 5. The simulation has been done using PSCAD/EMTDC package [15], with a sampling time of 10 kHz.

The nominal voltage of this power network is 45 kV with two loads of 3.93+j2.58 MVA and 1.5+j0.5 MVA connected through two double circuits; lines *L1, L2* of 20 km and *L3, L4* with 30 km.

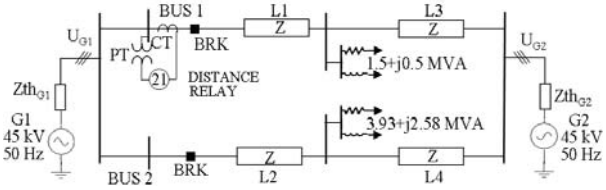


Fig. 5. Power system modeled for simulations.

Lines *L1* and *L2* are identical with mutual coupling, both

modeled by a PI circuit section. Likewise, lines *L3* and *L4* are also identical and with mutual coupling between both. The electrical networks connected to *G1* and *G2* are represented by their Thévenin equivalents, which are given by

$Zth_{G1}$= 4.2556 \ 84.44° Ω  $Zth_{G2}$ = 8.4677 \ 73.90° Ω

where $Zth_{G1}$ and $Zth_{G2}$ represent the equivalent source impedance of *G1* and *G2,* respectively. The Thévenin voltage magnitude of *G1* varies between 0.9 and 1.1 p.u. with respect to the nominal voltage of *G2*, while the voltage phase of *G1* varies ±10º respect to *G2*. These parameters variations are performed to simulate different states of power condition at the distance relay location point in *bus 1*.

The sequence data of the lines *L1*, *L2, L3* and *L4* are the following

$Rl_1$ = 0.35 Ω/km  $Rl_0$ = 0.4947 Ω/km

$Xl_1$ = 0.3987 Ω/km  $Xl_0$ = 1.4866 Ω/km

$Rl_{M0}$ = 0.1445 Ω/km  $Xl_{M0}$ = 0.9809 Ω/km

The equivalent network *G1* has been modeled with harmonic distortion. The total harmonic distortion in voltage waveform (THDV) is generated according to [16] with a maximum value of 5.5% in steady-state.

Extensive simulations have been performed varying the fault resistance, fault angle inception, prefault power conditions, type of conductor (*X/R* line ratio), THDV of *G1*, and fault location *m* within line *L1*.

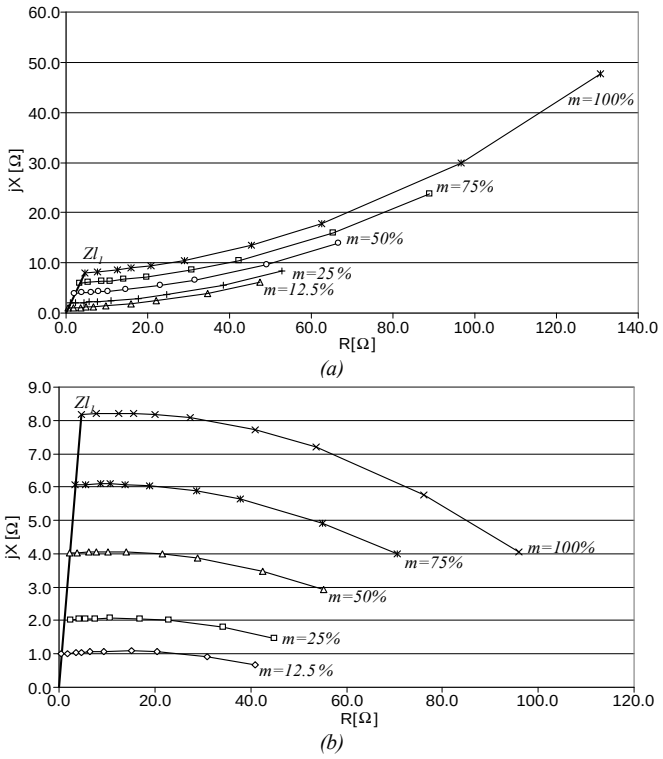


Fig. 6. Apparent impedance seen by the distance relay for SLG faults at different location, *m*, of line *L1* and varying $R_F$ from 0.001 to 75Ω with prefault condition of: *a) bus 1* importing power, and *b) bus 1 ex*porting power.

In Fig. 6 is represented the apparent impedance seen by the distance relay for SLG faults applied at different points of line length, *m*, and for a varying fault resistance between 0.001 and 75 Ω. For importing power prefault condition, the Thévenin voltage of *G1* is 45.40 kV∠40º and for *G2* is 44.75 kV∠45º and corresponds to Fig. 6.*a*. While for exporting power prefault condition, the Thévenin voltage of *G1* is 45.40 kV∠50º and for *G2* is 44.75 kV∠45º and corresponds to Fig. 6.*b*. The protection device is located on *bus 1*.

## V. Implementation of the Proposed Adaptive Scheme

The proposed adaptive scheme has been implemented to a distance algorithm based on DFFT. As shown in Fig. 7, the measured values of voltage and current are passed through an anti-aliasing filter represented by a 2nd order Butterwoth filter [17].

The filtered signals are introduced to the DFFT algorithm to determine the fundamental phasor of both voltage and current signals. A fault detector is implemented to select the prefault value of the current $I_L$. This data is refreshed every half-cycle. Once the fault detector operates, the phase jump is calculated by using (10) taking into account both signals $I_r$ and $I_L$.

The current phase jump result in an exponential relation with the *X/R* ratio seen by the relay during fault condition. Therefore the correction factor curve is represented by the following general form

$$X/R_F = A \cdot e^{B \cdot \Delta\phi} \tag{15}$$

where $X/R_F$ is the ratio seen by the relay during fault condition, and *A* and *B* are coefficients determined by the $Xl/Rl_1$ ratio of the protected line and which varies according to the power condition of the relay location (importing or exporting power).

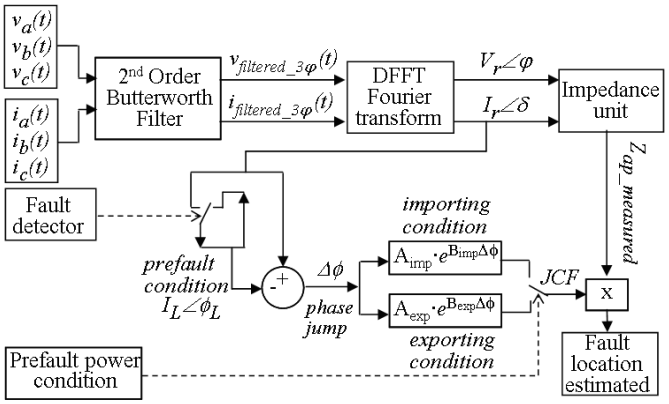


Fig. 7. Adaptive protection scheme using current jump phase correction factor implemented in a DFFT distance algorithm.

Then, depending of the prefault power condition, the jump corrective factor *JCF* is determined by calculating the difference between (15) and the *X/R* ratio obtained by the impedance measurement unit of the relay as follows

$$JCF = \frac{X/R_{measured} - X/R_F}{X/R_F} \tag{16}$$

Finally, the *JCF* is applied to the apparent impedance $Z_{ap\_measured}$ to improve the accuracy of the fault point location and mitigate the adverse effect on impedance estimation of high fault resistance and prefault power condition.

As shown at Fig. 8.*a*, the correction factor curve $X/R_F$ ratio

vs. the current phase jump $\Delta\phi$ is located between the curves obtained for $X/R_F$ ratio seen by the relay against faults at both 10% and 100% of total line length, which ensures an error coefficient within 5% of the actual value. Fig. 8.*b* shows the improvement introduced by the proposed *JCF* scheme to mitigate the adverse effect of importing power condition and fault resistance over the apparent impedance seen by the relay.

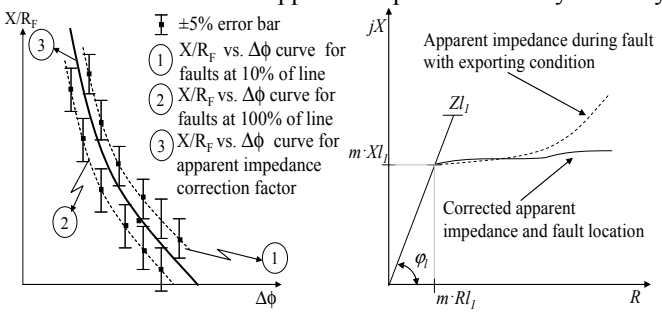


Fig. 8. Influence of *JCF* over the apparent impedance seen by the relay; *a)* Location of $X/R_F$ vs. $\Delta\phi$ curve for correction factor determination, *b)* corrected apparent impedance seen by the relay during faults with importing power condition.

The coefficients $A_{imp}$, $A_{exp}$ and $B_{imp}$, $B_{exp}$ (subscript *imp* and *exp* denote importing and exporting power condition, respectively) save a linear proportionality with the $Xl/Rl_1$ ratio of the line as follows (*Appendix B*)

$$A_{imp} = 0.1124 \cdot {Xl}/{Rl_1} + 3.8859 \quad (17)$$

$$B_{imp} = 0.4826 \cdot {Xl}/{Rl_1} - 3.5287 \quad (18)$$

$$A_{\exp} = -1.7299 \cdot {Xl}/{Rl_1} + 1.2063\text{E}5 \quad (19)$$

$$B_{\exp} = -0.0011 \cdot {Xl}/{Rl_1} - 2.6982 \quad (20)$$

In Fig. 9, the linear proportionality between these coefficients and the $Xl/Rl_1$ ratio is shown. In Fig. 9.*a*, the coefficient $A_{exp}$ is multiplied by $10^5$.

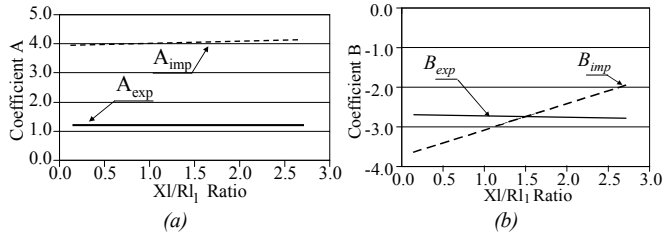


Fig. 9. Determination of (a) coefficient A and (b) coefficient B through the line $Xl/Rl_1$ ratio for importing power condition (dashed line) and exporting power condition (solid line).

## VI. Simulation of the Proposed Adaptive Scheme

For the study case described in Fig. 5, the line $Xl/Rl_1$ ratio is 1.1390. Therefore, the correction factor curve is given by:

- Importing power prefault condition:

$$X/R_F = 4.0142 \cdot e^{-2.9791 \cdot \Delta\phi} \quad (21)$$

- Exporting power prefault condition:

$$X/R_F = 1.2063\text{E}5 \cdot e^{-2.6994 \cdot \Delta\phi} \quad (22)$$

The curves of *JCF* obtained from the $Xl/Rl_1$ ratio of line *L1* during importing and exporting power prefault condition are illustrated in Figs. 10.*a* and 10.*b*, respectively.

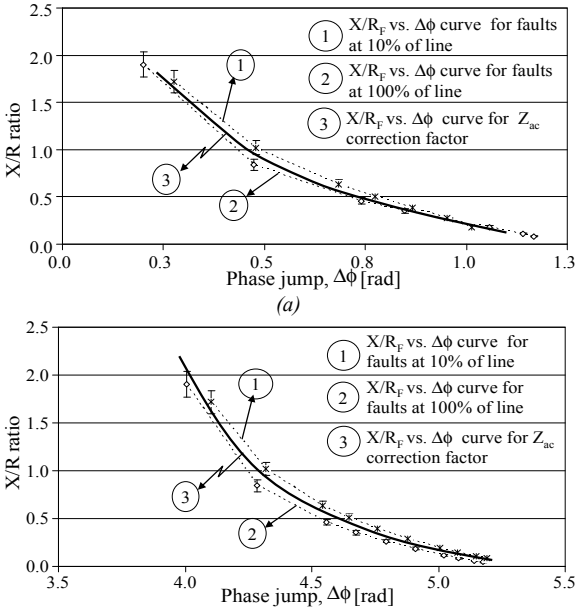


Fig. 10. Location of $X/R_F$ vs. $\Delta\phi$ curve for correction factor determination for: *a) bus 1* importing power, and *b) bus 1 e*xporting power.

As shown in these figures, the curves of *JCF* obtained from the $Xl/Rl_1$ ratio of line *L1* have approximately a ±5% of error margin respect the $X/R_F$ ratio curves seen by the relay for faults at both 10% and 100% of line length with a varying fault resistance up to 75 Ω.

The results obtained from implementing this adaptive scheme in distance algorithm are tabulated in Table I and the apparent impedance locus are shown in Figs. 11.*a* and 11.*b* for importing and exporting power, respectively.

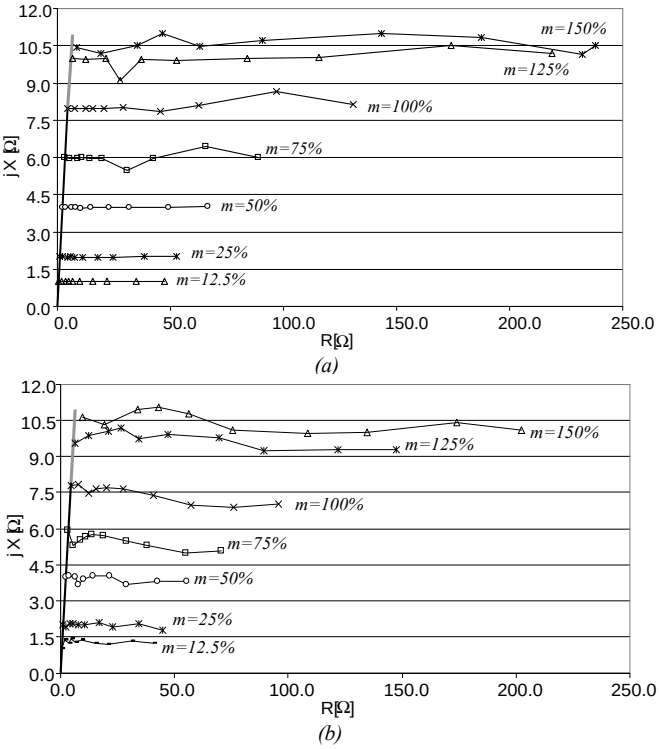


Fig. 11. Apparent impedance seen by the distance relay for SLG faults at different *m*, of line *L1* and varying $R_F$ from 0.001 to 75Ω with prefault condition of: *a) bus 1* importing power, and *b) bus 1 e*xporting power.

The relative error in fault point location, ε%, is determined as follows [18]

$$\varepsilon\% = \left| \frac{m_r - m}{m} \right| \cdot 100 \quad (23)$$

where $m_r$ is the fault point location estimated by the relay.

Considering fault resistances greater than 25 Ω, the improvement achieved in the fault location is at least 60.98% (for importing power condition) in comparison to the DFFT algorithm results. Even when the incidence of fault is in the remote line *L3*, the corrective factor performs an accurate estimation of the fault point location.

TABLE I
ERROR IN FAULT POINT LOCATION USING FFT DISTANCE ALGORITHM WITH THE PROPOSED ADAPTIVE SCHEME FOR 1.1390 XL/RL1 LINE RATIO

| Fault location (*m*) | Fault resistance [Ω] | Error in fault location, ε% | | | |
|---|---|---|---|---|---|
| | | DFFT distance algorithm | | DFFT distance algorithm+*JCF* | |
| | | Importing power | Exporting power | Importing power | Exporting power |
| 25% | 0.001 | 0.29 % | 0.29% | 0.00 % | 0.11% |
| | 5 | 5.24 % | 2.02% | 0.06 % | 1.44% |
| | 10 | 12.85 % | 3.15% | 0.66 % | 0.24% |
| | 25 | 48.58 % | 3.22% | 0.11 % | 5.66% |
| | 55 | 182.01 % | 9.31% | 0.96 % | 3.45% |
| | 75 | 320.52 % | 25.17% | 0.03 % | 3.89% |
| *50%* | 0.001 | 0.14 % | 0.80% | 0.00 % | 0.34% |
| | 5 | 4.09 % | 1.51% | 0.00 % | 0.05% |
| | 10 | 9.93 % | 1.75% | 1.45 % | 2.15% |
| | 25 | 37.57 % | 0.01% | 0.04 % | 0.70% |
| | 55 | 141.99 % | 12.54% | 0.05 % | 4.71% |
| | 75 | 251.39 % | 26.00% | 0.60 % | 4.71% |
| 75% | 0.001 | 0.21 % | 1.50% | 0.00 % | 0.80% |
| | 5 | 4.93 % | 1.88% | 0.02 % | 7.01% |
| | 10 | 11.56 % | 1.74% | 0.08 % | 3.86% |
| | 25 | 43.46 % | 1.46% | 7.58 % | 7.80% |
| | 55 | 166.87 % | 17.34% | 8.52 % | 14.21% |
| | 75 | 298.07 % | 32.74% | 0.53 % | 13.09% |
| 100% | 0.001 | 1.10 % | 2.67% | 0.01 % | 2.48% |
| | 5 | 8.23 % | 3.09% | 0.00 % | 5.90% |
| | 10 | 18.54 % | 2.63% | 0.00 % | 3.25% |
| | 25 | 69.92 % | 2.99% | 1.26 % | 6.92% |
| | 55 | 276.61 % | 27.00% | 9.25 % | 11.87% |
| | 75 | 500.13 % | 48.36% | 1.90 % | 10.88% |
| *125%* | 0.001 | 4.96 % | 6.63% | 0.04 % | 4.05% |
| | 5 | 22.01 % | 7.44% | 0.09 % | 0.84% |
| | 10 | 48.59 % | 5.83% | 0.03 % | 2.43% |
| | 25 | 192.15 % | 8.95% | 0.38 % | 1.94% |
| | 55 | 801.57 % | 59.59% | 5.76 % | 6.98% |
| | 75 | 1430.1 % | 97.56% | 2.19 % | 6.28% |

Varying the protected line $Xl/Rl_1$ ratio to 1.7171, keeping the remote line $Xl/Rl_1$ ratio in 1.1390 and incrementing the THDV to 7% is obtained the performance shown in Table II for the proposed adaptive scheme. From Fig. 10, coefficients A and B are the following

-Importing power prefault condition:

$$X/R_F = 4.0790 \cdot e^{-2.6001 \cdot \Delta\phi} \quad (24)$$

-Exporting power prefault condition:

$$X/R_F = 1.2062\ \mathrm{E5} \cdot e^{-2.7012 \cdot \Delta\phi} \quad (25)$$

As noticed for faults at *m*=125%, the error in fault point location has increased because of the difference of *X/R* rates between protected and remote lines. However, because of the exponential shape of current phase jump and $X/R_F$ ratio, the improvement in fault point location implementing the *JCF* scheme is still at least 49.77% in comparison with the DFFT algorithm.

TABLE II
ERROR IN FAULT POINT LOCATION USING FFT DISTANCE ALGORITHM WITH THE PROPOSED ADAPTIVE SCHEME FOR 1. 7171XL/RL1 LINE RATIO

| Fault location (*m*) | Fault resistance [Ω] | Error in fault location, ε% | | | |
|---|---|---|---|---|---|
| | | DFFT distance algorithm | | DFFT distance algorithm+*JCF* | |
| | | Importing power | Exporting power | Importing power | Exporting power |
| 25% | 0.001 | 0.29% | 0.29% | 0.00% | 0.05% |
| | 5 | 5.16% | 1.99% | 0.01% | 0.17% |
| | 10 | 12.66% | 3.11% | 0.36% | 0.13% |
| | 25 | 47.88% | 3.17% | 0.07% | 3.79% |
| | 55 | 179.39% | 9.17% | 1.06% | 3.80% |
| | 75 | 315.92% | 24.81% | 0.03% | 11.44% |
| *50%* | 0.001 | 0.14% | 0.79% | 0.00% | 0.30% |
| | 5 | 4.03% | 1.48% | 0.00% | 0.02% |
| | 10 | 9.79% | 1.73% | 0.21% | 0.31% |
| | 25 | 37.03% | 0.01% | 0.02% | 0.30% |
| | 55 | 139.95% | 12.36% | 0.01% | 0.56% |
| | 75 | 247.78% | 25.62% | 0.33% | 2.59% |
| 75% | 0.001 | 0.21% | 1.47% | 0.00% | 0.54% |
| | 5 | 4.86% | 1.86% | 0.02% | 7.71% |
| | 10 | 11.39% | 1.71% | 0.09% | 4.06% |
| | 25 | 42.84% | 1.44% | 6.67% | 6.86% |
| | 55 | 164.47% | 17.09% | 3.75% | 6.25% |
| | 75 | 293.79% | 32.27% | 0.08% | 1.90% |
| 100% | 0.001 | 1.09% | 2.63% | 0.00% | 1.04% |
| | 5 | 8.12% | 3.04% | 0.00% | 0.71% |
| | 10 | 18.27% | 2.59% | 0.00% | 1.79% |
| | 25 | 68.92% | 2.94% | 0.84% | 4.64% |
| | 55 | 272.63% | 26.62% | 10.17% | 13.06% |
| | 75 | 492.95% | 47.67% | 2.00% | 11.43% |
| *125%* | 0.001 | 7.34% | 9.81% | 5.50% | 10.69% |
| | 5 | 32.54% | 11.00% | 7.60% | 18.50% |
| | 10 | 71.84% | 8.62% | 11.30% | 26.78% |
| | 25 | 284.10% | 13.23% | 17.89% | 31.57% |
| | 55 | 1185.09% | 88.11% | 34.67% | 47.68% |
| | 75 | 2114.36% | 144.23% | 67.89% | 75.77% |

The comparison of the proposed *JCF* scheme with algorithms based on neural network has been performed with the radial basis function neural network RBFNN [11]. The testing patterns applied to the RBFNN are within the range of active and reactive power of the power system considered.

According to [11], the errors obtained with RBFNN are found to be lower than 2.25% for remote end faults (*m*=100%) and lower than 20.99% for close faults (*m*=25%). This indicates that the proposed *JCF* scheme provides a more accurate performance against close faults, but for remote end faults RBFNN offers best estimated impedance.

From these results, it can be noticed that implementing the proposed *JCF* scheme for distance protection is very promising as compared to RFBNN, taking into account that this latter technique requires to be trained by extensive patterns for each range of active and reactive power.

## VII. Conclusion

The algorithm presented is an adaptive distance relaying based on the modification of apparent impedance seen by the relay. From the current phase jump with fault inception a jump correction factor is estimated and applied to the apparent impedance.

This corrective factor is found to be an exponential function of the X/R line ratio which compensates the error of overreaching and underreaching of distance relay due to the adverse effect of prefault load condition on the apparent impedance locus.

Nonetheless, for faults in remote lines having an *X/R* line ratio considerably different from the protected line, the accuracy of the algorithm in locating the fault point is lower. Likewise, as the line length increases, the estimation of the fault location becomes less accurate, but still with minor error margin than those estimated by the conventional DFFT algorithm.

## Appendix A

Referring to Fig. 1, the interconnection of sequence networks for the SLG fault is shown in Fig. 12. Positive and negative sequence impedances are assumed to be equal and all variables subscripts *1, 2* and *0* represent positive, negative and zero sequence components, respectively.

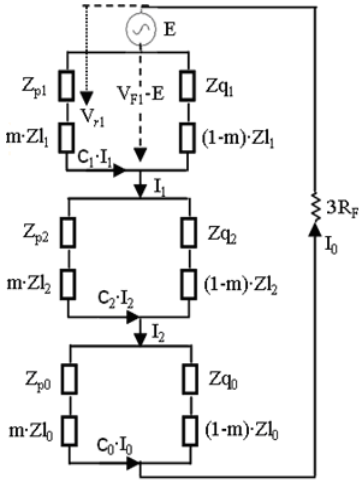


Fig. 12. Interconnection of sequence network for a SLG fault.

When the system is on load, the prefault voltage at the relay location, where for simplicity is assumed that the electromagnetic force sources in the positive sequence network of terminal $p$ and $q$ are equal ($E_P$=$E_q$=$E$), is determine as follows

$$V_L = E + I_L \cdot m \cdot Zl_1 \tag{26}$$

The total current at the fault point is

$$I_F = \frac{E}{C_1 \cdot (m \cdot Zl_1 + Z_{p1}) + C_2 \cdot (m \cdot Zl_2 + Z_{p2}) + C_0 \cdot (m \cdot Zl_0 + Z_{p0}) + 3 \cdot R_F} = I_1 = I_2 = I_0 \tag{27}$$

$C_1$, $C_2$ and $C_0$ are the distribution factors for positive, negative and zero sequence, respectively, and are defined as

$$C_1 = \left( \frac{Z_{q1} + (1-m) \cdot Zl_1}{Z_{q1} + Z_{p1} + Zl_1} \right) \tag{28}$$

$$C_0 = \left( \frac{Z_{q0} + (1-m) \cdot Zl_0}{Z_{q0} + Z_{p0} + Zl_0} \right) \tag{29}$$

where $Z_{p1}$ and $Z_{p0}$ are the positive and zero sequence equivalent source impedance of bus $p$, respectively, $Z_{q1}$ and $Z_{q0}$ the positive and zero sequence equivalent source impedance of bus $q$, respectively, $Zl_1$ and $Zl_0$ the positive and zero sequence impedance of the line, respectively, and $m$ is the distance to fault. The distribution factor $C_2$ is equivalent to $C_1$.

Using these relations and after algebraic manipulation, the total current $I_F$ can be written as

$$I_F = \frac{E}{m \cdot Zl_1 \cdot \left( 2 \cdot C_1 + C_0 \cdot \frac{Zl_0}{Zl_1} \right) + 2 \cdot C_1 \cdot Z_{p1} + C_0 \cdot Z_{p0} + 3 \cdot R_F} \tag{30}$$

Re-arranging (30) it is obtained the following expression

$$I_F = \frac{E}{\psi \cdot \left( m \cdot Zl_1 + \frac{3 \cdot R_F}{\psi} \right) + 2 \cdot C_1 \cdot Z_{p1} + C_0 \cdot Z_{p0}} \tag{31}$$

where $\psi$ is given by

$$\psi = 2 \cdot C_1 + C_0 \cdot \frac{Zl_0}{Zl_1}$$

Substituting $E$ in (31) from (26) generates the following expression for the total fault current $I_F$

$$I_F = \frac{V_L - I_L \cdot m \cdot Zl_1}{\psi \cdot \left( m \cdot Zl_1 + \frac{3 \cdot R_F}{\psi} \right) + 2 \cdot C_2 \cdot Z_{p1} + C_0 \cdot Z_{p0}} \tag{32}$$

where defining the apparent impedance of the fault path $Z_F$ as in (3)

$$Z_F = m \cdot Zl_1 + \frac{3 \cdot R_F}{\psi}$$

and substituting it in (32) generates $I_F$ as shown in (5)

$$I_F = \frac{V_L - I_L \cdot m \cdot Zl_1}{\psi \cdot Z_F + 2 \cdot C_1 \cdot Z_{p1} + C_0 \cdot Z_{p0}}$$

Finally, substituting the total fault current $I_F$ from (32) in (1) generates the following expression for the fault current at the relay location

$$I_r = \frac{V_L \cdot Zl_1 \cdot \psi + Z_L \cdot \left( 3 \cdot R_F \cdot I_L + 2 \cdot C_1 \cdot Z_{p1} + C_0 \cdot Z_{p0} \right)}{2 \cdot C_1 \cdot \left( m \cdot Zl_1 + Z_{p1} \right) + C_0 \cdot \left( m \cdot Zl_0 + Z_{p0} \right) + 3 \cdot R_F} \tag{33}$$

## Appendix B

In *Section IV-C* it has been studied the performance of the proposed *JCF* scheme varying the line $Xl/Rl_1$ ratio. The coefficients $A$ and $B$ of the $X/R_F$ ratio vs. $\Delta\phi$ curves during importing and exporting power prefault condition have been obtained varying the operation voltage, line length and $Xl/Rl_1$ ratio of the line in the power system simulated.

The variation in the voltage operation and the line length in the power system have a negligible effect over the final result of the phase jump and the coefficients *A* and *B*, as shown in Table III. The standard deviation of coefficients *A* and *B* resulting from varying both parameters voltage operation and line length is within a 0.4028% from the value derivate of (17) to (20) for each coefficient and which is considered negligible.

TABLE III
PARAMETERS A AND B VARYING THE OPERATION VOLTAGE AND LINE LENGTH IN THE POWER SYSTEM

| Coefficient | Varying X/R source | | Varying voltage operation | Standard Deviation |
|---|---|---|---|---|
| | 45 kV, Length=20 km | 45 kV, Length=75 km | 132 kV, Length= 75 km | |
| $A_{imp}$ | 4.0142 | 4.1538 | 4.0139 | 0.0807 |
| $A_{exp}$ | 1.2063E5 | 1.2063E5 | 1.2063E5 | 0.0001 |
| $B_{imp}$ | -2.9790 | -2.9996 | -2.9786 | 0.01201 |
| $B_{exp}$ | -2.6994 | -2.7152 | -2.6988 | 0.0093 |

Otherwise, the *X/R* line ratio has a significant effect over the current phase jump once fault occurs. Coefficients *A* and *B* differs for different *X/R* line ratios to improve the estimated apparent impedance by the relay. These variations are shown in Table IV, where coefficients *A* and *B* have been determined varying *X/R* line ratio of most common used overhead conductors. From these simulation results it has been determined the experimental equations (17) to (20) for coefficients *A* and *B*.

TABLE IV
PARAMETERS A AND B VARYING THE X/R LINE RATIO

| Varying X/R line length | Coefficient | | | |
|---|---|---|---|---|
| | $A_{imp}$ | $B_{imp}$ | $A_{exp}$ | $B_{exp}$ |
| 3.0000 | 4.2231 | -2.0101 | 1.2100E5 | -2.7012 |
| 2.8000 | 4.1800 | 2.4000 | 1.2063E5 | -2.7015 |
| 2.2000 | 4.1400 | 2.3670 | 1.2063E5 | -2.7000 |
| 1.900 | 4.1200 | 2.6118 | 1.2063E5 | -2.6998 |
| 1.7170 | 4.0789 | 2.7001 | 1.2063E5 | -2.7003 |
| 1.1390 | 4.0139 | 2.9790 | 1.2063E5 | -2.6990 |
| 1.0000 | 4.0100 | 3.0461 | 1.2063E5 | -2.6993 |
| 0.8000 | 3.9550 | 3.0426 | 1.2063E5 | -2.6995 |

The coefficients *A* and *B* from varying the $Xl/Rl_1$ are shown in Fig. 13 for both importing and exporting conditions, with the respective straight line resulting from (17) to (20). It is noticed that the mean error when considering linear proportionality between coefficients (*A* and *B)* and $Xl/Rl_1$ is within 0.0163%.

In Fig. 14 the location of $X/R_F$ vs. $\Delta\phi$ curves the for correction factor of a 72 km line length at 45 kV are shown. As it can be observed, the error margin becomes wider as line length increases. However, results achieved still have better error margin than those estimated by DFFT algorithm.

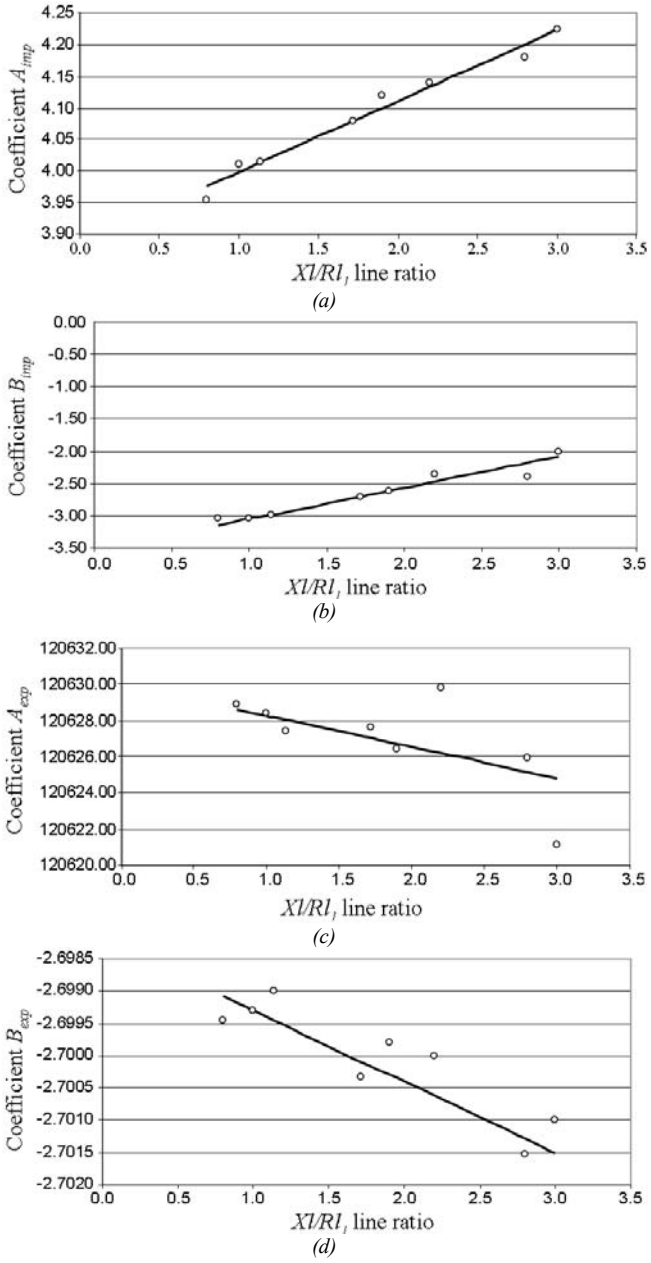


Fig. 13. Linear proportionality between coefficients: (a) $A_{imp}$, (b) $B_{imp}$, (c) $A_{exp}$ and (d) $B_{exp}$ and $Xl/Rl_1$ line ratio.

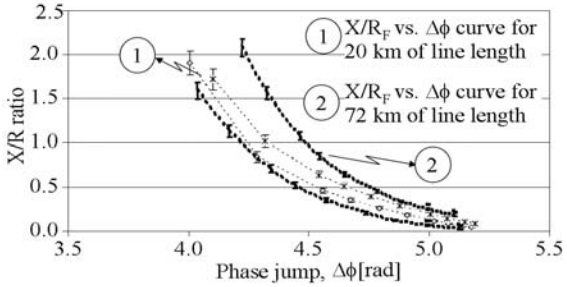


Fig. 14. Location of $X/R_F$ vs. $\Delta\phi$ curve for correction factor determination for 20 km and 72 km of line length.

## REFERENCES


[1] Rosas Ortiz G, Sidhu T.S, "High-speed backup scheme for zone 2 of non-pilot distance relays," *IET Generation, Transmission & Distribution*, vol. 1, no. 6, pp. 938-947, 2007.

[2] Izykowski J., Rosolowski E, Saha M.M, "Postfault analysis of operation of distance protective relays of power transmission lines," *IEEE Trans. Power Delivery*, vol. 22, no. 1, pp. 74 – 81, 2007.

[3] V. Cook, *Analysis of Distance Protection*, Studies Press: England, 1985, vol. I, pp. 63-169.

[4] *IEEE Recommended Practice for Protection and Coordination of Industrial and Commercial Power Systems*, IEEE Standard 242, 2001.

[5] S. H. Horowitz, A. G. Phadke, J. S. Thorp, "Adaptive Transmission System Relaying," *IEEE Trans. Power Delivery,* vol. 3, no. 4, pp. 1436 – 1445, 1988

[6] Radojevic, Z.M, "New one terminal digital algorithm for adaptive reclosing and fault distance calculation on transmission lines," *IEEE Trans. Power Delivery,* vol. 21, no. 3, pp. 1231 – 1237, 2006.

[7] Ching-Shan Chen, Chih-Wen Liu and Joe-Air Jiang , "Application of combined adaptive fourier filtering technique and fault detector to fast distance protection," *IEEE Trans. Power Delivery*. vol. 21, no. 2, 2006, pp. 619-626.

[8] Chi-Shan Yu, "A discrete Fourier transform-based adaptive mimic phasor estimator for distance relaying applications," *IEEE Trans. Power Delivery,* vol. 21, no. 4, pp. 1836 - 1846, 2006.

[9] Tai Nengling, Chen Chen, "A New Weak Fault Component Reactance Distance Relay Based on Voltage Amplitude Comparison," *IEEE Trans. Power Delivery*, vol. 23, no. 1, pp. 87 – 93, 2008.

[10] M. G. Adamiak, G. E. Alexander and W. Premerlani, "Advancements in Adaptive Algorithms for Secure High Speed Distance Protection," GE technical publication GER-3962, Available: http://pm.geindustrial.com/faq/Documents/Alps/GER-3962.pdf.

[11] Bhavesh R. Bhalja and Rudra Prakash Maheshwari, "High-Resistance Faults on Two Terminal Parallel Transmission Line: Analysis, Simulation Studies, and an Adaptive Distance Relaying Scheme," *IEEE Trans. Power Delivery*, vol. 22, no. 2, pp. 801 - 812, 2007.

[12] Denis V. Coury, Jim S. Thorp, Kenneth M. Hopkinson and P. Birman Kenneth (2000, March 27), "Agent Technology Applied to Adaptive Relay Setting for Multi-Terminal Lines," Computer Science technical report, Cornell University [Online], Available: http://hdl.handle.net/1813/5785.

[13] Ming-yu Yang, Yong-li Zhu, "Study on adaptive distance protection using multi-agent technology," *in Proc. 7th Inter. Power Engineering Conf*., Nov. 29 -Dec. 2, 2005, pp. 618 – 622.

[14] S. Skok and A. Marusic, "Comparison of various neural network models applied to adaptive distance protection," in *Proc. Inter. Conf. Electric Utility Deregulation and Restructuring and Power Technologies*, 4-7 April, 2000, pp. 244 – 250.

[15] PSCAD v4.2, Manitoba HVDC Research Centre, 2006.

[16] *IEEE Recommend Practices and Requirements for Harmonic Control in Electrical Power Systems*, IEEE Standard 519, 1992.

[17] Li Zhongshen, "Design and Analysis of Improved Butterworth Low Pass Filter," in *Proc. 8th International Conference on Measurement and Instruments*, China, Aug. 16-18, 2007, pp. 1-729 - 1-732.

[18] S.R. Samantaray, P.K. Dashb, "Transmission line distance relaying using a variable window short-time Fourier transform," *Electric Power Systems Research*, vol. 78, pp. 595-604, 2008.


**Miguel García-Gracia** was born in Saint-Brieuc, France on April 23, 1963. He received his B.S. (1986), M.Sc. (1989), and Ph.D. (1996) degrees from the University of Zaragoza. He is presently Lecturer of Electrical Engineering and Area Director of Electric Power System at CIRCE. His main research interests are in the field of power system, power system protection, electrical energy system, renewable energy integration, lightning protections and dielectrics.

**N. El Halabi** was born in Anaco, Venezuela on September 21, 1985. He received the Electrical Engineering degree in 2006 from Universidad Simón Bolívar, Venezuela. He is currently performing the Ph.D. in Renewable Energy at Universidad de Zaragoza, Spain. His research interests are Power System Protection and Integration and Planning of Hybrid Power Systems.

**S. Martín Arroyo** was born in Zaragoza (Spain). She received B.Sc. degree in Electrical Engineering from the University of Zaragoza at 2004. She is currently pursuing the Ph.D. in Renewable Energy at University of Zaragoza. She is project manager of renewable energy at CIRCE. Her research interests are analysis of integration, production and regulation of renewable energy, power quality in electrical networks, analysis and simulation of wind farms.

**H.M. Khodr** (M'99) received the M.Sc., Eng., and Ph.D. degrees in electrical engineering from the José Antonio Echeverría Higher Polytechnic Institute (ISPJAE), Havana, Cuba, in 1993 and 1997, respectively.
He is a former Associate Professor of Electrical Engineering at Universidad Simón Bolívar, Caracas, Venezuela. He was a Researcher with INESC Porto, Porto, Portugal. Currently, he is a Researcher with the GECAD-Knowledge Engineering and Decision-Support Research Center of the Electrical Engineering-Polytechnic Institute of Porto (ISEP/IPP), Porto. He has participated in a number of projects performed for the local industries. His current research activities concentrate on planning, operation, and economics of electrical distribution and industrial power systems, power quality, grounding systems, and optimization.

# Phase Jump Correction Factor Applied to the Differential Equation Algorithm by an Adaptive Scheme

M. García-Gracia [a], N. El Halabi [a], S. Borroy [a], L. Giménez de Urtasun [a]

[a] CIRCE, Research Center of Consumption and Energy Resource, C/ Maria de Luna 3, 50018, Zaragoza, Spain.

**Abstract**

The measured impedance of distance protections is affected by an error due to the combined effects of fault resistance and prefault load. This paper proposes the implementation of an adaptive scheme which applies a correction factor based on the phase jump of the current waveform once fault occurs to improve the apparent impedance estimated by relays based on Differential Equation Algorithms (DEA). Relation between current phase jump, prefault power conditions and fault resistance has been deduced with an experimental curve that relates the error introduced into the estimated apparent impedance with the registered phase jump. Through this experimental curve a correction factor has been obtained as an exponential function of the phase jump that, applied to the apparent impedance measured by the relay, allows to mitigate the adverse effect of prefault power. The proposed adaptive scheme improves significantly the accuracy of the estimated fault location without delaying the response time of the DEA algorithm. The application of this scheme does not require communication links with the remote end of line and is extended to all types of fault.

***Keywords:*** Distance protection algorithm, differential equation algorithm, adaptive scheme, impedance locus, current phase jump

## 1. Introduction

Recent advances on distance relaying systems are mainly focused to address two important issues: fast tripping decision and accurate impedance estimation. This leads to enhance distance algorithms by mitigating sources of error and reducing sampling time to achieve a fast and accurate convergence of the estimated impedance, taking into account the compatibility of these improvements with ongoing technologies of distance relays.

Distance protections based on Differential Equation Algorithm (DEA) present a major advantage because are not sensitive to the decaying DC component of the current waveform achieving response time within 0.32 cycles [1]. In most cases, tripping decision may occur before CT saturation whereas Fourier algorithms [2], [3] have an operating time of at least one cycle [4] that leads to misoperation of distance relays during CT saturation. Traveling wave algorithms are theoretically the fastest, but unlike DEA algorithms, put too high demands on current and voltage sampling time for accurate operation (240 kHz) and particularly for nonpilot schemes, the minimal distance resolution is highly dependent on frequency sampling [5]. Thus, a relay based on the DEA is suitable since high speed operation is achieved along with fault detection, estimation of fault location, fault classification and tripping decision within the operation time.

Improvement of DEA algorithm presented at [6] is based on considering the effect of mutual couplings over the differential equations that describes an electric circuit with parallel lines. In [9] a post median filtering is proposed to improve soundness, but with higher time delay. Likewise, [1] presents a filtering technique that mitigates the adverse effect of harmonic distortion over the estimated apparent impedance, delaying slightly the operation time of DEA

algorithm. These improvements increase accuracy of estimated apparent impedance by compensating the errors raised from mutual couplings and harmonic distortion, however the effect of fault resistance in conjunction with prefault power condition is still an important source of error on this final estimation.

Fault resistance and prefault power exert an important influence on the distance measurement process that has been acknowledged for a long time [7], [8] and leads the traditional distance relaying approach to experience underreach and overreach problems. Due to the continuously changing power conditions in networks, adaptive schemes may represent an appropriate way to modify the preferred protective response in order to make them more attuned to prevailing power system conditions.

Several adaptive schemes have been applied to distance relaying systems. In [9] an adaptive concept based on processing harmonic data from voltage waveform is presented to improve fault distance location, while [2] and [3] present an adaptive Fourier filtering technique to remove the decaying dc offset component from fault signals for accelerating the response of the relay. Other adaptive concepts are oriented to use a compensating factor that modifies the characteristic of the distance protection based on neural and agent technologies to improve the estimated apparent impedance and to increment security in high speed distance protection [10]-[12]. These adaptive techniques achieve significant improvement in the accuracy, security and dependability of the distance protection algorithm based on phasor methods as Fourier algorithm and not for time domain methods as DEA algorithm.

This paper presents an adaptive distance relaying scheme based on the current phase jump data, during fault conditions, to determine a correction factor that is applied to the apparent impedance seen by relays based on DEA algorithm. The correction factor used is found to be an exponential function of the current phase jump once fault inception and is applied to the apparent impedance in order to increase the accuracy in the estimation of the apparent impedance measured by the relay.

To verify the proposed adaptive scheme, detailed analyses of the apparent impedance seen by the relay have been performed, taking into account mutual coupling, prefault condition, fault resistance, fault angle inception and *X/R* line ratio.

The proposed algorithm modifies the apparent impedance seen by the relay according to the current phase jump once fault occurs. Then, by means of the jump corrective factor *JCF* which is determined by an exponential relation reactance error vs. current phase jump, the algorithm mitigates the adverse effect of fault resistance over the apparent impedance locus and calculates an improved fault location within the protected line. The application of this scheme does not require communication links with the remote terminal of the protected line.

Simulations have been performed for single line to ground faults (SLG) and evaluated with both adaptive schemes based on Discrete Fast Fourier Transform (DFFT) algorithm [3] and conventional DEA algorithm [6] to highlight the effectiveness and accuracy achieved by the new proposed adaptive scheme.

## 2. The Differential Equation Algorithm

### 2.1 Basic assumptions and derivation of DEA algorithm

A summarized derivation of the DEA algorithm is presented subsequently. Suitable references for detailed derivation of this algorithm are [1], [6]. The derivation of the equations for this algorithm requires the following assumptions:

- the voltage and current transformers are ideal in the frequency range from 50 to 500 Hz
- the line is perfectly transposed
- shunt capacitances are neglected

The DEA algorithm is based on the differential equation that describes an electric circuit. Therefore, under fault conditions, the protected line is modeled as follows

$$\begin{bmatrix} u_a \\ u_b \\ u_c \end{bmatrix} = k_r \mathbf{R}_1 \begin{bmatrix} i_a \\ i_b \\ i_c \end{bmatrix} + k_l \mathbf{L}_1 \frac{d}{dt} \begin{bmatrix} i_a \\ i_b \\ i_c \end{bmatrix} \tag{1}$$

where, $u_a$, $u_b$, $u_c$ and $i_a$, $i_b$, $i_c$ are the phase quantities of voltages and currents, respectively. The parameters $k_r$ and $k_l$ are the relative line length for the resistive part and the inductive part, respectively. For a fault on the protected line, both should be bounded between 0 and 1. In an ideal case, $k_r$ and $k_l$ should be similar. The arrays $\mathbf{R}_1$ and $\mathbf{L}_1$ are the positive sequence resistance and inductance matrix for the protected line, respectively. Through the assumption of perfectly transposition mentioned above, the following relation between both self and mutual with positive and zero sequence parameters can be expressed

$$\begin{aligned} \mathbf{L}_1 &= \mathbf{L}_s - \mathbf{L}_{mt} \quad , \quad \mathbf{L}_0 = \mathbf{L}_s + 2\mathbf{L}_{mt} \\ \mathbf{R}_1 &= \mathbf{R}_s - \mathbf{R}_{mt} \quad , \quad \mathbf{R}_0 = \mathbf{R}_s + 2\mathbf{R}_{mt} \end{aligned} \tag{2}$$

being the subscripts *0* and *1* the zero and positive sequence, respectively, and the subscripts *s* and *mt* the self and mutual parameters, respectively. Taking into account that the zero sequence current is

$$i_0 = (i_a + i_b + i_c)/3 \tag{3}$$

Eq. (1) can be rewritten as follows

$$\begin{bmatrix} u_a \\ u_b \\ u_c \end{bmatrix} = k_r \mathbf{R}_1 \begin{bmatrix} i_a \\ i_b \\ i_c \end{bmatrix} + k_l \mathbf{L}_1 \frac{d}{dt} \begin{bmatrix} i_a \\ i_b \\ i_c \end{bmatrix} + k_r \left(\mathbf{R}_0 - \mathbf{R}_1\right) \begin{bmatrix} i_0 \\ i_0 \\ i_0 \end{bmatrix} + k_l \left(\mathbf{L}_0 - \mathbf{L}_1\right) \frac{d}{dt} \begin{bmatrix} i_0 \\ i_0 \\ i_0 \end{bmatrix} \tag{4}$$

Considering a SLG fault on phase *a* at a distance *k* of the protected line length, the voltage of the faulty phase is given by

$$u_a = k_r \left[\mathbf{R}_1 i_a + (\mathbf{R}_0 - \mathbf{R}_1) i_0\right] + k_l \left[\mathbf{L}_1 \frac{di_a}{dt} + (\mathbf{L}_0 - \mathbf{L}_1) \frac{di_0}{dt}\right] \tag{5}$$

Then, for this type of faults, (4) can be expressed in a general form as follows

$$u = k_r i_r + k_l \mathbf{L}_1 \frac{di_l}{dt} \tag{6}$$

being

$$\begin{aligned} u &= u_a \\ i_r &= \mathbf{R}_1 \cdot i_a + (\mathbf{R}_0 - \mathbf{R}_1) \cdot i_0 \\ i_l &= \mathbf{L}_1 \cdot i_a + (\mathbf{L}_0 - \mathbf{L}_1) \cdot i_0 \end{aligned} \tag{7}$$

The derivation of variables $u$, $i_r$ and $i_l$ of the general form (6) are different for each type of fault (three phase, double phase to ground and SLG) and are detailed at [1].

2.2 Solution of the continuous-time equations in discrete-time

The two unknown parameters $k_r$ and $k_l$ can be estimated by differentiating (6) in discrete-time domain as follows [6]

$$\begin{bmatrix} u \\ \dfrac{du}{dt} \end{bmatrix} = \begin{bmatrix} i_r & \mathbf{L}_1 \dfrac{di_l}{dt} \\ \dfrac{di_r}{dt} & \mathbf{L}_1 \dfrac{d^2 i_l}{dt^2} \end{bmatrix} \cdot \begin{bmatrix} k_r \\ k_l \end{bmatrix} \tag{8}$$

Subsequently, by using three continuous samples of $i_r$, $i_l$ and $u$, fault distance can be deduced by

$$k_{rn} = \frac{\left(i_{ln} - i_{l(n-1)}\right)\left(u_{(n-1)} + u_{(n-2)}\right) - \left(i_{l(n-1)} - i_{l(n-2)}\right)\left(u_n + u_{(n-1)}\right)}{\Delta T} \tag{9}$$

$$k_{ln} = \left(\frac{f_s}{2}\right)\frac{-\left(i_{rn} - i_{r(n-1)}\right)\left(u_{(n-1)} + u_{(n-2)}\right) + \left(i_{r(n-1)} - i_{r(n-2)}\right)\left(u_n + u_{(n-1)}\right)}{\Delta T} \tag{10}$$

where $f_s$ is the frequency sampling of the protective device, $n$ the index of time and $\Delta T$ the determinant of the inverse of the matrix in (8) expressed as follows

$$\Delta T = \left(i_{r(n-1)} + i_{r(n-2)}\right)\left(i_{\ln} - i_{l(n-1)}\right) - \left(i_{rn} + i_{r(n-1)}\right)\left(i_{l(n-1)} + i_{l(n-2)}\right) \tag{11}$$

## 3. Influence of prefault power condition on the apparent impedance seen by the relay

In order to obtain a brief understanding of the influence of system load on fault currents and voltages, it is helpful to perform a fault study on the system shown at Fig. 1 for a single line to ground (SLG) fault. The effective voltage and current phasors at a relay location during healthy system load conditions are denoted by $V_{PF}$, $I_{PF}$ respectively. The ratio of these two signals gives the corresponding load apparent impedance seen from the relay location in stable conditions and is denoted as $Z_{PF}=V_{PF}/I_{PF}$.

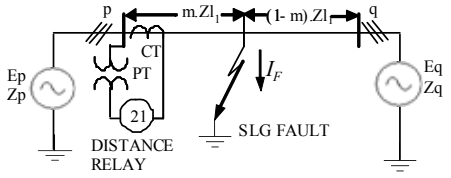


Fig. 1. System arrangement for a SLG fault study case.

Following a SLG fault inception at phase *a* and solving the equivalent sequence networks circuit leads to an evaluation of the fault current $I^F_{relay}$ seen by the relay at phase *a*. As detailed at [13], the influence of prefault load current $I_{PF}$ is taken into account using the superposition theorem. Therefore, the fault current $I^F_{relay}$ is represented by two terms as follows

$$I^F_{relay} = \psi \cdot I_F + I_{PF} \tag{12}$$

being $I_F$ the total current at the fault point, and is determined as follows

$$I_F = \frac{V_{PF} - I_{PF} \cdot m \cdot Zl_1}{\psi \cdot Z_F + 2 \cdot C_1 \cdot Z_{p1} + C_0 \cdot Z_{p0}} \tag{13}$$

where the factors $C_1$ and $C_0$ are constants for a given system arrangement and denote the distribution factor expressions as follows

$$C_1 = \left(\frac{Z_{q1} + (1-m) \cdot Zl_1}{Z_{q1} + Z_{p1} + Zl_1}\right) \text{ and } C_0 = \left(\frac{Z_{q0} + (1-m) \cdot Zl_0}{Z_{q0} + Z_{p0} + Zl_0}\right)$$

being $Z_{p1}$ and $Z_{p0}$ the positive and zero sequence equivalent source impedance of bus *p*, respectively; $Z_{q1}$ and $Z_{q0}$ the positive and zero sequence equivalent source impedance of bus *q*, respectively; $Zl_1$ the positive sequence impedance of the line and *m* the distance to fault. $Z_F$ is the apparent impedance of the fault path and is equivalent to

$$Z_F = m \cdot Zl_1 + \frac{3 \cdot R_F}{\psi} \tag{14}$$

being $R_F$ the fault resistance. The factor $\psi$ denotes the following distribution factor expression

$$\psi = 2 \cdot C_1 + C_0 \cdot \frac{Zl_0}{Zl_1} \tag{15}$$

Then, the voltage equation at the relay location for faults in phase *a* is

$$V^F_{relay} = m \cdot Zl_1 \cdot \left(\psi \cdot I_F + I_{PF}\right) + 3 \cdot R_F \cdot I_F \tag{16}$$

Thus, using voltage and current signals ($V^F_{relay}$ and $I^F_{relay}$, respectively), the apparent impedance seen by the relay is $Z^F_{relay}$. The latter impedance can be expressed as a function of $Z_{PF}$ and $R_F$ [13] as follows

$$Z^F_{relay} = \frac{V^F_{relay}}{I^F_{relay}} = Z_{PF} \cdot \frac{3 \cdot R_F + m \cdot Zl_1 \cdot \left(2 \cdot C_1 + \xi / Z_{PF}\right)}{3 \cdot R_F + 2 \cdot C_1 \cdot Z_{PF} + \xi} \tag{17}$$

where $\xi$ is constant for a given system arrangement and represents the following simplified impedance

$$\xi = 2 \cdot C_1 \cdot Z_{p1} + C_0 \cdot \left(\frac{Zl_0}{Zl_1} + Z_{p0}\right) \tag{18}$$

For a better comprehension of the effect of prefault load in the performance of $Z^F_{relay}$ it results suitable to represent the locus of a complex variable in an R-X diagram for different prefault load conditions. At [13] a detailed procedure for the construction of this diagram is presented, where prefault load current is considered and the corresponding fault location (as viewed by the relay) is represented by the radius of the circular locus obtained from the argument of (17) denoted as $\theta_F$.

In the R-X diagram shown in Fig. 2, $\varphi_l$ corresponds to the apparent impedance angle of the line. The locus of the apparent impedance $Z^F_{relay}$ for varying $R_F$ represents a straight line when there is no power exchange between *bus p* and *bus q* ($\theta_F = 0$). However, under power exchange conditions, the locus of $Z^F_{relay}$ denotes a concave upwards arc that links fault location points for varying fault resistance ($R_F \neq 0$) when importing power condition ($\theta_F < 0$) and concave downwards arc when exporting power condition ($\theta_F > 0$). Note that under importing condition of *bus p*, the link path between different fault point locations is represented by P1 and under exporting power condition by P2.

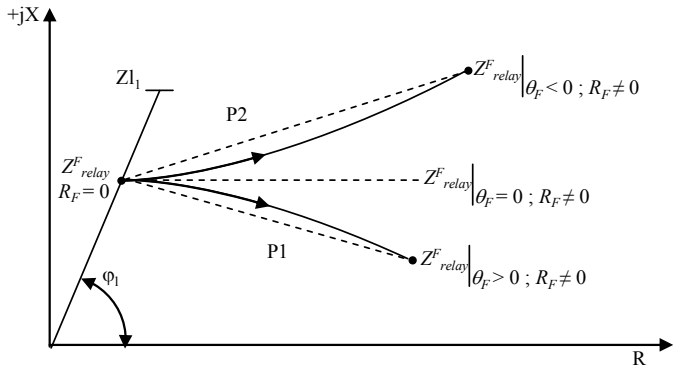


Fig. 2. Locus of measured impedance $Z^F_{relay}$ for varying $R_F$. P1 represents the path for $\theta_F$ inductive and P2 the pat for $\theta_F$ capacitive.

Thus, the effect of importing power at the relay location is to cause an increase in the apparent impedance estimated by the relay, and results in further underreaching of the protection. An export power condition causes an overreaching tendency which results in a miscoordination between distance protection zones [11], [13].

## 4. Relation of current phase jump with fault location

One of the sources of error in measured impedance is the fault resistance and prefault power condition and is represented in the second term of (14). This error can be only compensated if both system arrangement and fault path impedance are known parameters. However, when considering the operation of distance relays, the current and voltage magnitudes of the receiving terminals are unknown parameters for nonpilot protection schemes.

Therefore, the magnitude and phase of the total current at fault path $I_F$, shown in Fig. 1, are unknown and the potential rise due to the fault resistance is not considered by the measurement units of distance relays for a correct estimation of the apparent impedance. This leads to an error in distance measurement whenever fault resistance is present.

Nonetheless, the current phase jump introduced with fault inception is related to the error introduced in the reactance $Xl_1$ seen by the distance protection during fault condition. This study proposes a correction factor based on the current phase jump behavior during fault conditions to mitigate the error component of (14).

The scheme is applicable for all types of fault, and the degree of compensation remains constant for all fault locations within the protected circuit since $Xl_1$ is a constant for a particular line length.

The voltage $v^F_{relay}(t)$ at the relay location, once fault occurs, is of the form

$$v^F_{relay}(t) = \sqrt{2}\cdot \mathrm{V}^{\mathrm{F}}_{\mathrm{relay}}\cdot \sin(\omega t) \tag{19}$$

where the phase jump expected is within 0.2º ~ 0.5º and is considered negligible (Fig. 3). However, the phase jump is significant for the fault current waveform seen by the relay $i^F_{relay}(t)$ which is given by

$$i^F_{relay}(t) = \sqrt{2}\cdot \mathrm{I}^{\mathrm{F}}_{\mathrm{relay}}\cdot \sin(\omega t - \phi) \tag{20}$$

being $\phi$ the arc tangent of $Xl_1/Rl_1$ seen by the relay during fault condition.

Under prefault conditions, the current waveform $i_{PF}(t)$ is represented by

$$i_{PF}(t) = \sqrt{2}\cdot \mathrm{I}_{\mathrm{PF}}\cdot \sin(\omega t - \phi_{PF}) \tag{21}$$

where $\phi_{PF}$ is the arc tangent of $Xl_1/Rl_1$ seen by the relay during prefault condition. Then, the phase jump in the current waveform $\Delta\phi$, shown in Fig. 3, is given by

$$\Delta\phi = \arg\left(i^F_{relay}(t) - i_{PF}(t)\right) = \phi - \phi_{PF} \tag{22}$$

and it is proportional to the argument of the difference between $Z^F_{relay}$ and $Z_{PF}$, as follows

$$\Delta\phi = \arg\left(Z^F_{relay} - Z_{PF}\right) \tag{23}$$

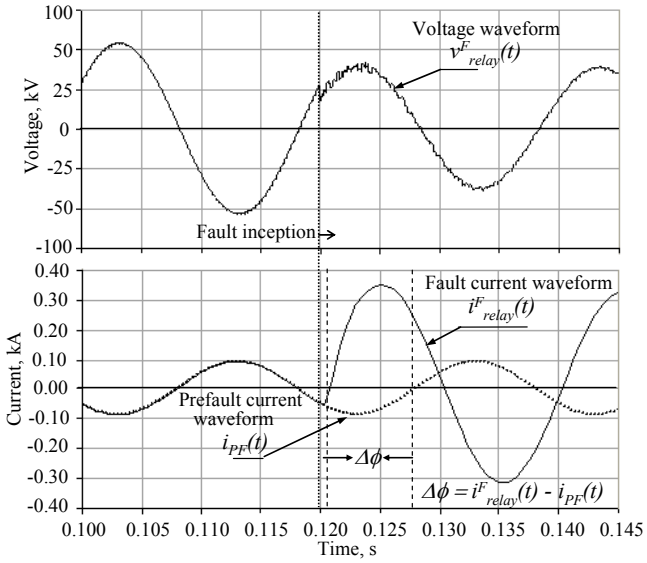


Fig. 3. Phase jump in the current waveform (solid line) with fault inception in comparison with the prefault current waveform (pointed line) and voltage waveform.

Substituting (17) in (23) results

$$\Delta\phi = \arg\left(\frac{Z_{PF}\cdot\left(2\cdot C_1\cdot\left(m\cdot Zl_1 - Z_{PF}\right) + \xi\cdot\left(\frac{m\cdot Zl_1}{Z_{PF}} - 1\right)\right)}{3\cdot R_F + 2\cdot C_1\cdot Z_{PF} + \xi}\right) \tag{24}$$

and simplifying this latter expression the following relation is obtained

$$\Delta\phi = \arg\left(Z_{PF}\cdot\frac{\left(2\cdot C_1\cdot Z_{PF} + \xi\right)\cdot\left(\frac{m\cdot Zl_1}{Z_{PF}} - 1\right)}{3\cdot R_F + 2\cdot C_1\cdot Z_{PF} + \xi}\right) \tag{25}$$

As load impedance is much greater than line impedance, i.e. $Z_{PF} >> m\cdot Zl_1$, the ratio $m\cdot Zl_1 / Z_{PF}$ tends to zero and expression (25) becomes

$$\Delta\phi = 180^\circ + \arg\left(Z_{PF}\right) + \arg\left(\frac{\left(2\cdot C_1\cdot Z_{PF} + \xi\right)}{3\cdot R_F + 2\cdot C_1\cdot Z_{PF} + \xi}\right) \tag{26}$$

which shows that $\Delta\phi$ contains data of both the effect of prefault conditions $Z_{PF}$ and fault resistance $R_F$.

## 5. Power system simulation

The power system considered for this study is shown in Fig. 4. The simulation has been done using PSCAD/EMTDC package [14], with a sampling time of 10 kHz.

The nominal voltage of this power network is 45 kV with two loads of 3.93+j2.58 MVA and 1.5+j0.5 MVA connected through two double circuits; lines L1, L2 of 20 km and L3, L4 with 30 km.

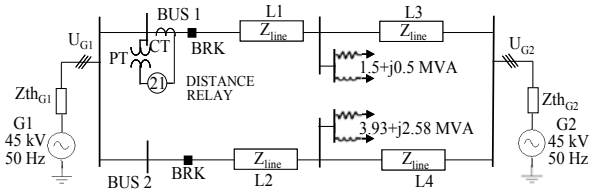


Fig. 4. Power system considered for the study.

Lines L1 and L2 are identical with mutual coupling, both modeled by a PI circuit section. Likewise, lines L3 and L4 are also identical and with mutual coupling between both. The electrical networks connected to G1 and G2 are represented by their Thévenin equivalents, which are given by

$Zth_{G1}$= 2.1850+j8.9498 Ω $Zth_{G2}$ = 1.8414+j7.9761 Ω

where $Zth_{G1}$ and $Zth_{G2}$ represent the equivalent source positive sequence impedance of G1 and G2, respectively. Parameters variations considered to simulate different states of power condition at the distance relay in bus 1 are: Thévenin voltage magnitude of G1 varies between 0.9 and 1.1 p.u. respect to the nominal voltage of G2 and voltage phase of G1 varies ±5º respect to G2.

The sequence data of the lines L1, L2, L3 and L4 are the following

$Zl_1$ = 0.2604+j0.3986 Ω/km $Bl_1$ = 0.2878E-08 S/km

$Zl_0$ = 0.49105+j1.4325 Ω/km $Bl_0$ = 0.1698E-08 S/km

$Z_{M0}$=0.2308+j0.9268 $B_{M0}$ = 0.5574E-09 S/km

being $Bl_1$ and $Bl_0$ the positive and zero sequence susceptance of line, respectively, and $Z_{M0}$ and $B_{M0}$ the mutual coupling zero sequence impedance and susceptance, respectively, of the double circuit shown in Fig. 4.

The equivalent network G1 has been modeled with harmonic distortion. The total harmonic distortion in voltage waveform (THDV) is generated according to [15] with a maximum value of 5.5% in steady-state.

## 6. Development and implementation of the proposed phase jump correction factor

The proposed phase jump correction factor has been implemented to a distance algorithm based on DEA using an adaptive scheme. As shown in Fig. 5, the measured values of voltage and current are passed through an anti-aliasing filter represented by a 2nd order Butterworth filter [16]. Then, the filtered signals are introduced to the DEA algorithm to determine the apparent impedance. A fault detector is implemented to select the prefault value of the current $i_{PF}(t)$. This data is refreshed every half-cycle.

Once the fault detector operates, the phase jump is calculated by using (22) and taking into account both signals $i^F_{relay}(t)$ and $i_{PF}(t)$.

The *JCF* represents the relative error on the $Z^F_{relay}$ and results in an exponential function of the current phase jump $\Delta\phi$ ratio seen by the relay during fault condition. Therefore the correction factor curve is represented by the following general form

$$JCF(\Delta\phi) = A \cdot e^{B \cdot \Delta\phi} \tag{27}$$

where A and B are constants for a given *X/R* ratio of the protected line that varies according to the power condition of the relay location (importing or exporting power).

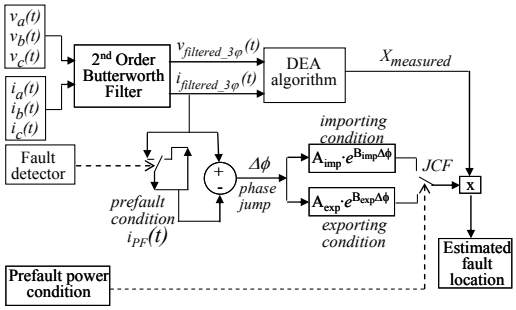


Fig. 5. Adaptive protection scheme using current phase jump correction factor implemented in a DEA distance algorithm.

Finally, the *JCF* is applied to the $X_{measured}$ to improve the accuracy of the fault point location estimated by DEA algorithm as follows

$$\text{Fault distance [km]} = \frac{X_{measured} \cdot \left(1 - JFC(\Delta\phi)\right)}{Xl_1} \tag{28}$$

As shown at Fig. 6.*(a)*, the *JCF* vs. current phase jump $\Delta\phi$ represents an exponential curve that fits the amount of errors on estimated apparent impedance varying fault location *m* from 10% to 100% of protected line length and fault resistance $R_F$ from 0.001 to 75 Ω. Fig. 6.*(b)* shows the improvement introduced by the proposed *JCF* scheme to mitigate the adverse effect of importing power condition and fault resistance over the apparent impedance seen by the relay.

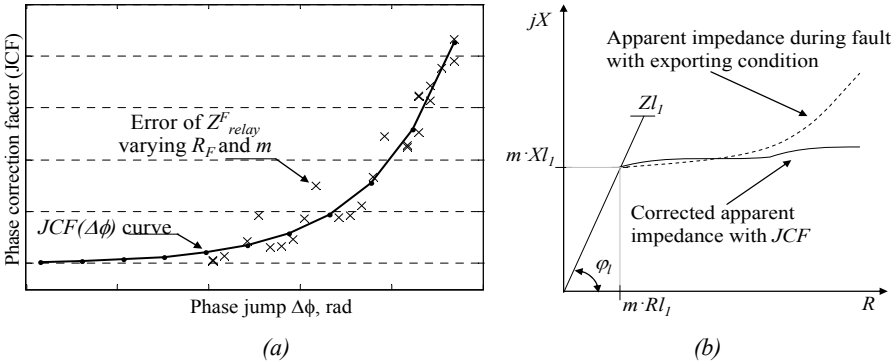


Fig. 6. Improvement of the proposed *JCF* scheme over the apparent impedance seen by the relay; (a) *JCF* vs. $\Delta\phi$ curve (b) corrected apparent impedance seen by the relay during faults with importing power condition.

The coefficients $A_{imp}$, $A_{exp}$ and $B_{imp}$, $B_{exp}$ (subscript *imp* and *exp* denote importing and exporting power condition, respectively) save a linear proportionality with the *X/R* ratio of the protected line as follows

$$A_{imp} = 1.0667 \cdot {}^{X}\!/_{R} + 6.652 \tag{29}$$

$$B_{imp} = 6.1139 \cdot {}^{X}\!/_{R} - 3.9533 \tag{30}$$

$$A_{\exp} = -0.4439 \cdot {}^{X}\!/_{R} - 0.4820 \tag{31}$$

$$B_{\exp} = 1.8722 \cdot {}^{X}\!/_{R} + 4.0095 \tag{32}$$

Coefficients $A_{imp}$ and $A_{exp}$ given in (29) and (31) are normalized with $1x10^{-06}$ and $1x10^{-18}$, respectively. In Fig. 7, the linear proportionality between these coefficients and the *X/R* line ratio is shown.

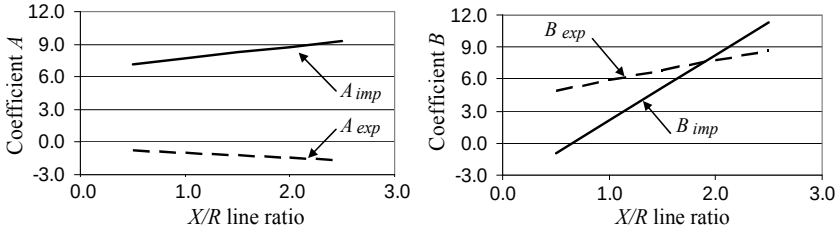


*(a)* *(b)*

Fig. 7. Determination of (*a*) coefficient A and (*b*) coefficient B through the line *X/R* ratio for importing power condition (solid line) and exporting power condition (dashed line).

## 7. Performance of DEA algorithm using the proposed adaptive scheme

### 7.1 Performance of the proposed *JCF* adaptive scheme

For the power system described in Fig. 4, the *X/R* ratio of line L1 is 1.53. Therefore, the *JCF* is given by:

- Importing power prefault condition:

$$JCF = 8.2841x10^{-06} \cdot e^{5.401 \cdot \Delta\phi} \tag{33}$$

- Exporting power prefault condition:

$$JCF = -1.162x10^{-18} \cdot e^{6.874 \cdot \Delta\phi} \tag{34}$$

The curves of *JCF* for importing and exporting power prefault condition are illustrated in Figs. 8.*(a)* and 8.*(b)*, respectively. These curves of *JCF* obtained from the phase jump $\Delta\phi$ have an average relative error of ±8.8% respect to the error on the apparent impedance seen by the relay for faults, varying fault resistance, up to 75 Ω, and position *m* from 10% to 100% of line length.

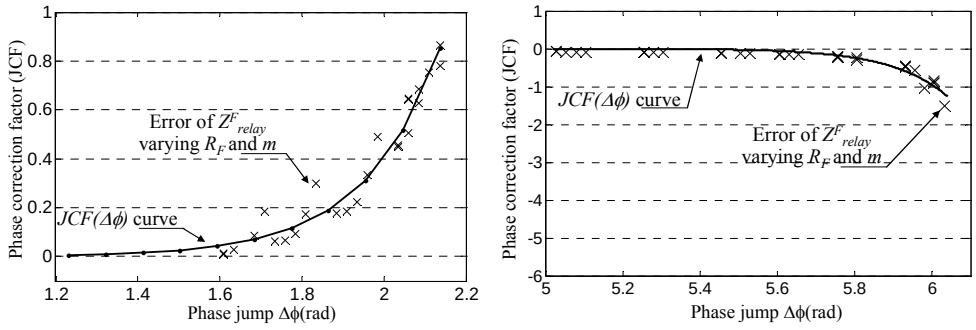


*(a)* *(b)*

Fig. 8. *JCF* vs. phase jump $\Delta\phi$ for: a) bus 1 importing power, and b) bus 1 exporting power.

The performance of DEA using the proposed adaptive scheme is analyzed by comparing the simulation results with DFFT and DEA algorithm values. The lowest accurate performance of DEA algorithm is appreciated in SLG faults. Thus, the behavior of this algorithm implementing the *JCF* is presented by analyzing the accuracy of estimated apparent impedance against SLG faults on the power system shown in Fig. 4.

The apparent impedance locus obtained from implementing this adaptive scheme in DEA algorithm are shown in Figs. 9.*(a)* and 9.*(b)* for importing and exporting power, respectively, and results showing the relative error on the estimated fault location ε% are tabulated in Table 1.

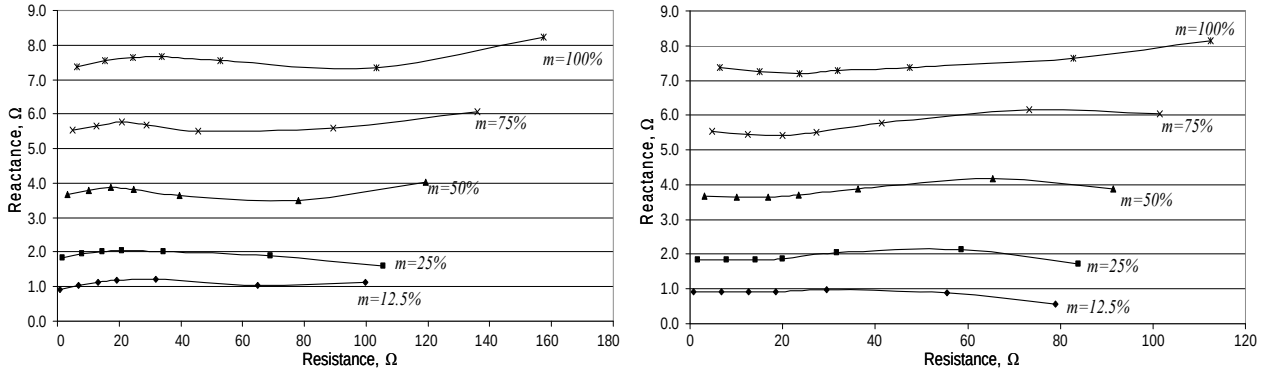


Fig. 9. Apparent impedance seen by the distance relay for SLG faults at different *m*, of line *L1* and varying $R_F$ from 0.001 to 75Ω with prefault condition of: *a) bus 1* importing power, and *b) bus 1 e*xporting power.

**Table 1.** Error in estimated fault location using DEA distance algorithm with the proposed *JCF* adaptive scheme for 1.53 X/R line ratio

| Fault location (*m*) | Fault resistance [Ω] | Error in fault location, ε% | | | | | |
|---|---|---|---|---|---|---|---|
| | | DFFT algorithm | | DEA algorithm | | Proposed DEA algorithm+*JCF* | |
| | | Importing power | Exporting power | Importing power | Exporting power | Importing power | Exporting power |
| 12.5% | 0.001 | -6.56% | -6.14% | -8.09% | -8.52% | -4.15% | -4.31% |
| | 5 | -0.04% | -7.15% | 5.57% | -9.66% | 3.16% | -8.80% |
| | 10 | 8.39% | -8.65% | 18.36% | -12.65% | 10.82% | -8.60% |
| | 25 | 45.49% | -15.87% | 49.15% | -28.49% | 18.48% | -2.83% |
| | 50 | 148.74% | -36.04% | 75.49% | -104.05% | 5.12% | -11.13% |
| | 75 | 307.64% | -64.89% | 86.50% | -934.75% | 10.32% | -24.95% |
| *25%* | 0.001 | -6.55% | -6.05% | -7.97% | -8.45% | -4.88% | -4.26% |
| | 5 | -2.91% | -6.88% | 0.04% | -9.81% | -2.51% | -9.09% |
| | 10 | 1.79% | -7.97% | 8.48% | -12.17% | 1.19% | -8.75% |
| | 25 | 22.42% | -12.73% | 33.52% | -22.73% | 1.00% | 1.77% |
| | 50 | 79.80% | -25.04% | 62.64% | -58.22% | -5.98% | 7.12% |
| | 75 | 168.18% | -41.99% | 77.92% | -152.55% | -24.56% | -15.78% |
| 50% | 0.001 | -6.50% | -5.87% | -7.77% | -8.35% | -4.57% | -4.20% |
| | 5 | -4.23% | -6.67% | -2.77% | -10.05% | -5.05% | -9.44% |
| | 10 | -1.30% | -7.62% | 2.91% | -12.28% | -2.87% | -9.84% |
| | 25 | 11.56% | -11.38% | 22.16% | -21.11% | -9.13% | -2.93% |
| | 50 | 47.44% | -20.21% | 50.37% | -45.23% | -14.19% | 4.18% |
| | 75 | 102.95% | -31.71% | 68.50% | -90.79% | 1.09% | -2.47% |
| 75% | 0.001 | -6.43% | -5.66% | -7.59% | -8.28% | -4.29% | -5.16% |
| | 5 | -4.53% | -6.53% | -3.51% | -10.30% | -5.52% | -9.69% |
| | 10 | -2.07% | -7.52% | 1.30% | -12.72% | -3.80% | -10.27% |
| | 25 | 8.80% | -11.21% | 18.43% | -21.80% | -8.82% | -3.52% |
| | 50 | 39.38% | -19.42% | 45.75% | -44.79% | -7.13% | 2.78% |
| | 75 | 87.03% | -29.69% | 64.73% | -84.39% | 1.66% | 0.85% |
| *100%* | 0.001 | -6.32% | -5.42% | -7.40% | -8.20% | -5.09% | -5.07% |
| | 5 | -4.51% | -6.40% | -3.66% | -10.62% | -5.67% | -10.01% |
| | 10 | -2.14% | -7.50% | 0.88% | -13.39% | -4.24% | -10.93% |
| | 25 | 8.45% | -11.47% | 17.53% | -23.53% | -5.54% | -8.17% |
| | 50 | 38.64% | -19.97% | 44.93% | -48.46% | -8.74% | -4.21% |
| | 75 | 86.26% | -30.27% | 64.30% | -90.43% | 3.13% | 1.94% |

7.2 Accuracy of the proposed adaptive scheme estimating fault point location

As it can be appreciate in Table 1, for fault resistances greater than 50 Ω the improvement achieved in the fault location are at least 89.10 % and 90.63% (for importing power condition) in comparison with DFFT and DEA algorithm,

respectively. The error in estimating fault location ε% for SLG faults at remote terminal with 75 Ω of fault resistance using DFFT, DEA and proposed *JCF* adaptive scheme algorithm, with importing power condition, are shown in Fig. 10.

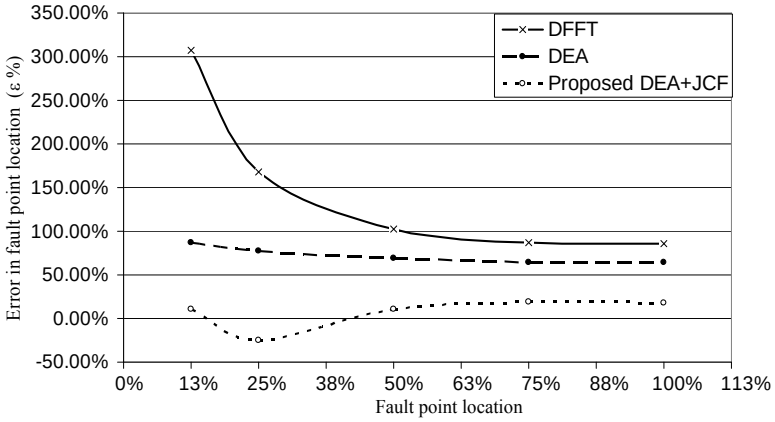


Fig. 10. Error in fault point location ε% for SLG faults at remote terminals with $R_F$ 75Ω and importing power prefault condition using DFFT, DEA and proposed *JCF* adaptive scheme algorithm.

The DEA algorithm using the proposed adaptive scheme improves considerably the estimated fault location. Nonetheless, the behavior for faults at 25% seems to be less accurate in comparison with the rest of fault locations. This is because the exponential curve of the *JCF* used to fit the apparent impedance error shown in Fig.8 presents slightly more dispersion in the zone corresponding to faults at 25% of line length, however is more effective for faults at remote end terminal where an accurate estimated impedance is highly appreciated for avoiding misoperation of distance relays.

In this paper, the exponential curve is preferred because of its effectiveness for remote end faults and parameters simplicity, however the flexibility of the method allows its application through other curves.

7.3 Response time of the algorithm

Fig. 11 shows the convergence time of the DEA algorithm with the proposed *JCF* adaptive scheme in comparison with the DFFT algorithm for SLG fault at 12.5% of the protected line with 75 Ω of fault resistance and exporting prefault power condition. As it can be observed, the convergence time of DEA algorithm is 6.4 ms while DFFT algorithm convergence time is 20 ms (1 cycle). Fault occurs at 0.12 s.

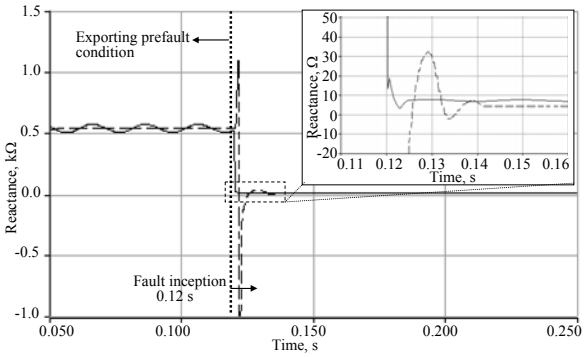


Fig. 11. Response time of DEA algorithm with proposed *JFC* adaptive scheme (solid line) and DFFT algorithm (dashed line) for a SLG fault at 12.5% of protected line with $R_F$ 75 Ω and exporting power condition. Fault occurs at 0.12 s.

## 8. Conclusion

The proposed adaptive scheme applies a correction factor to the apparent impedance estimated by DEA distance algorithm, which is determined through the phase jump registered on the current waveform once fault occurs.

This corrective factor is found to be an exponential function of the X/R line ratio which compensates the error of overreaching and underreaching of distance relay due to the adverse effect of prefault load condition on the apparent impedance locus.

The implementation of the proposed adaptive scheme does not delay the response time of DEA distance algorithm allowing an accurate and fast tripping decision against high resistive faults in comparison with Fourier distance algorithms.

**References**


[1] García-Gracia, M., El Halabi, N., Montañés, A., Khodr, H.M. and Villén M.: 'Improvement of DEA performance against harmonic distortion', Electric Power Systems Research, 2010, 80, (5), pp. 582-591

[2] Chi-Shan Yu: 'A discrete Fourier transform-based adaptive mimic phasor estimator for distance relaying applications', IEEE Trans. Power Delivery, 2006, 21, (4), pp. 3387-3395

[3] Ching-Shan Chen, Chih-Wen Liu and Joe-Air Jiang:' Application of combined adaptive Fourier filtering technique and fault detector to fast distance protection', IEEE Trans. Power Delivery, 2006, 21, (2), pp. 619-626

[4] Grčar, B., Ritonja, J., Polajžer, B., Stanković A.M: 'Estimation methods using dynamic phasors for numerical distance protection', IET Gener. Transm. Distrib., 2008, 2, (3), pp. 433–443

[5] Da Silva, M., Coury, D.V., Oleskovicz , M. and Segatto, Ê.C.: 'Combined solution for fault location in three terminal lines based on wavelet transforms', IET Gener. Transm. Distrib., 2010, 4, (1), pp. 94-103

[6] García-Gracia, M., Osal, W., Comech, M.P.: 'Line protection based on the differential equation algorithm using mutual coupling', Electric Power Systems Research, 2007, 77, (5-6), pp. 566-573

[7] M. Akke, J.S. Thorp: 'Some improvements in the three-phase differential equation algorithm for fast transmission line protection', IEEE Trans. Power Delivery, 1998, 13, (1), pp. 66-72

[8] Filomena, A.D., Hartstein, R., Resener, M., and Bretas, A.S.: 'Ground distance relaying with fault-resistance compensation for unbalanced systems', IEEE Trans. Power Delivery, 2008, 23, (3), pp. 1319-1326

[9] Radojevic, Z.M: 'New one terminal digital algorithm for adaptive reclosing and fault distance calculation on transmission lines', IEEE Trans. Power Delivery, 2006, 21, (3), pp. 1231–1237

[10] Tai Nengling, Chen Chen: 'A new weak fault component reactance distance relay based on voltage amplitude comparison', IEEE Trans. Power Delivery, 2008, 23, (1), pp. 87-93

[11] Bhavesh R., B. and Prakash Maheshwari R.: 'High-resistance faults on two terminal parallel transmission line: analysis, simulation studies, and an adaptive distance relaying scheme', IEEE Trans. Power Delivery, 2007, 22, (2), pp. 801 - 812

[12] Ming-yu Yang, Yong-li Zhu: 'Study on adaptive distance protection using multi-agent technology'. Proc. 7th Int. Conf. Power Engineering, Singapure, Nov. 2005, pp. 618 – 622

[13] Cook V.: 'Analysis of Distance Protection' (Studies Press, 1985, 1st edn.)

[14] Manitoba HVDC Research Centre: PSCAD v4.2, (2006)

[15] Std. 519-1992: 'IEEE Recommend Practices and Requirements for Harmonic Control in Electrical Power Systems', 1992

[16] Zhongshen Li: 'Design and Analysis of Improved Butterworth Low Pass Filter', Proc. 8th International Conference on Measurement and Instruments, China, Aug. 2007, pp. 1-729 - 1-732

# Anexo C. Otros trabajos desarrollados

Applied Energy 87 (2010) 3467–3474

Contents lists available at ScienceDirect

Applied Energy

journal homepage: www.elsevier.com/locate/apenergy

# Improvement of large scale solar installation model for ground current analysis

M. García-Gracia [a], N. El Halabi [a,*], H.M. Khodr [b], Jose Fco Sanz [a]

[a] CIRCE, Center of Research for Energy Resources and Consumption, C/Maria de Luna 3, 50018 Zaragoza, Spain
[b] GECAD – Knowledge Engineering and Decision-Support Research Center of the Polytechnic Institute of Porto, Portugal

ARTICLE INFO

*Article history:*
Received 27 January 2010
Received in revised form 26 April 2010
Accepted 29 April 2010
Available online 31 May 2010

*Keywords:*
PV installation modeling
Ground currents
Grounding couplings
Large-scale solar installation
Current distortion
Leakage impedance

ABSTRACT

Application of a simplified PV model to large-scale PV installations neglects the current distortion, potential rise and losses in the system as consequence of the capacitive coupling inside the dc electric circuit. These capacitive couplings represent a leakage impedance loop for the capacitive currents imposed by the high frequency switching performance of power converters. This paper proposes a suitable method to reproduce these harmonic currents injected not only into the grid, but also into the dc circuit of the PV installation. The capacitive coupling proposed of PV modules with ground is modeled as a parallel resistance and capacitor arrangement which leads to an accurate approximation to the real operation response of the PV installation. Results obtained are compared with those of simplified models of PV installations used in literature. An experimental validation of the proposed model was performed with field measurements obtained from an existing 1 MW PV installation. Simulation results are presented together with solutions based on the proposed model to minimize the capacitive ground current in this PV installation for meeting typical power quality regulations concerning to the harmonic distortion and safety conditions and to optimize the efficiency of the installation.



## 1. Introduction

Renewable energy systems are being considered as promising generation sources to cover the continuously increasing demand of energy and to improve reliability of electric power systems [1,2]. In particular, photovoltaic (PV) solar energy has become significant and attractive due to their availability and compatibility with typical demand curves of distribution networks. However, the extensive dimension required for PV installations leads to develop optimum sizing methods to guarantee the lowest investment with full use of PV arrays, so that the installation can work at the optimum conditions in terms of investment and power system reliability [3]. In small scale PV installations, the performance of the installation strongly depends on manufactured modules [4]. Otherwise, for large-scale PV installations, electrical parameters, such as the capacitive coupling with grounding systems, become significant because of the high frequency current imposed by the power converters and can affect considerably the behavior of the plant.

Based on field measurements, it has been noticed the importance of modeling the PV array with capacitive coupling with the grounding system, to accurately simulate the dc and ac components of the current waveform measured in the installation. This capacitive coupling is part of the electric circuit consisting of the PV arrays, cables capacitive couplings, ac filter elements and the grid impedance, and its effect is being appreciated in most large-scale PV plants. Due to this capacitive coupling between PV modules and earth, potential differences imposed by switching actions of the converter inject a capacitive ground current [5,6] which can cause significant electromagnetic interferences, grid current distortion, losses in the system, high noise level in the installation and unsafe conditions for work [7,8].

Several PV installation analysis are presented in literature [4,9–11], where most theoretical analysis and experimental verifications have been performed for small scale PV installations without considering ground coupling. Converter models and topologies also have been studied [2,12], but without considering the amount of losses produced by the capacitive circuit that appears due to the switching actions.

Simplified PV installation models, presented in [13–15], have been evaluated for small scale installations, however the application of these models to large scale installations neglects the current distortion and losses as consequence of capacitive coupling. In [16], the total conversion losses of a 3 MW PV installation have been studied considering reflection losses, low radiation and shadow losses, temperature losses, auxiliary losses, array losses and converters losses. The latter two factors sum a total of 10% of the rated power where part of these losses is due to the capacitive coupling that was neglected in [11].

The paper proposes an improved model for large-scale PV installations that details the capacitive coupling of the electric

* Corresponding author. Tel.: +34 976761923 ; fax: +34 976762226.
*E-mail address:* nabileh@unizar.es (N. El Halabi).

0306-2619/$ - see front matter © 2010 Elsevier Ltd. All rights reserved.
doi:10.1016/j.apenergy.2010.04.031

circuit with the grounding system. The developed model for PV installations allows to analyze the current distortion, electromagnetic interference, ground losses and Ground Potential Rise (GPR) [17] due to the capacitive coupling. In the paper, after the detailed description of the proposed model, different simulation results are pointed out. Finally an experimental validation of the model applied to an existing 1 MW PV installation is presented together with solutions based on the proposed model to minimize the capacitive ground current in this PV installation for meeting typical power quality regulations concerning to the harmonic distortion and safety conditions, as well as to optimize the design by increasing the PV installation efficiency.

## 2. Ground capacitance coupling in PV installation

PV installations with a rated power greater than 500 kW are considered as large scale systems [8]. In Fig. 1 a typical arrangement of a large-scale PV installation is represented. In most large-scale PV installations it may be outlined that are systems with long cables (over 8 km) and a detailed modeling of the network to take full advantage of the actual system capacity is needed [7].

The region between PV modules and PV structure essentially acts as an insulator between layers of PV charge and ground. Most parallel capacitive effects that may be ignored at very low frequencies can not be neglected at very high frequencies, because the reactance $X_c$ will become quite small due to the inverse proportionality with frequency $f$ and will introduce a low reactance path between power elements and ground.

This effect is present in PV installations because of the high frequency switching carried out by the converters stage, which arises different capacitive coupling between modules and ground and must be represented as a leakage loop between PV arrays, cables and electronic devices with the grounding system. By means of this leakage loop, capacitive currents are injected to the grounding system creating a GPR along the PV installation which introduces current distortion, electromagnetic interference, noise and unsafe conditions for work.

As PV installations have low inductance [5], they draw ripple in the voltage waveform which produce significant ripple currents in the dc current waveform [8]. These harmonics are related to the pulse number of the converter circuit. The natural frequency of a resonant circuit is a parameter that determines the vulnerability of the installation against harmonics and it is determined as follows [8]:

$$\textit{Natural frequency} = \frac{1}{2\cdot\pi}\cdot\sqrt{\frac{1}{L\cdot C}} \tag{1}$$

where $C$ and $L$ are the capacitance and inductance of the resonant circuit, respectively.

Depending on the commutation frequency, the harmonics produced may be significant according to the capacitive coupling and the resonant frequency inside the PV installation. Moreover, every PV array is considered as an independent current source with a dc current ripple independent of the converter ripple. These ripple currents are not in synchronism with the converter and produce subharmonics in the dc circuit which increase the Total Harmonic Distortion in current waveform (THDI) [18,15].

The typical maximum harmonic order $h = 40$, defined in the power quality standards, corresponds to a maximum frequency of 2 kHz (with 50 Hz as fundamental frequency). However, the typical commutation frequency of DC/DC and DC/AC converters, usually operated with the Pulse Width Modulation (PWM) technique, is higher than 3 kHz. Hence, the commutation frequencies are not represented in the harmonic indicators. Nevertheless, in practice there are substantial contributions at low order harmonics (mainly for $h = 3$, 5 and 7) in the harmonic currents injected into the grid [5]. Moreover, higher order harmonics up to the 100th order, can be an important concern in large-scale PV installations where converters with voltage notching, high pulse numbers, or PWM controls result in induced noise interference, current distortion, and local GPR at PV arrays.

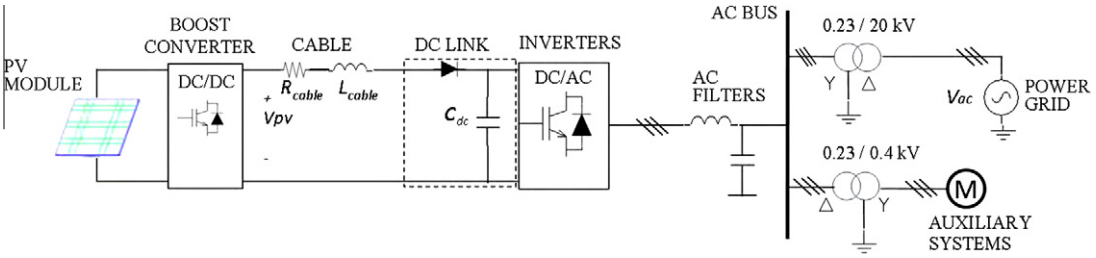


**Fig. 1.** Typical topology of a large-scale PV installation.

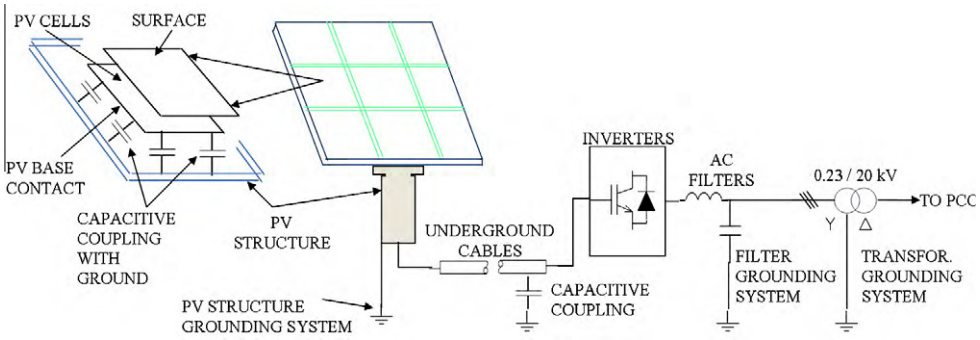


**Fig. 2.** Modeling of capacitive coupling between the electric circuit and the grounding system of the installation.

The proposed method is suitable to reproduce these harmonic currents injected not only into the grid, but also into the dc circuit of the PV installation that would lead to internal resonant, current distortion and unsafe work conditions where capacitive discharge currents could exceed the threshold of safety values of work [19]. The capacitive coupling is part of the electric circuit consisting of the PV cells, cables capacitive couplings, ac filter elements and the grid impedance, as shown in Fig. 2, and its effect is being appreciated in most large scale PV plants.

## 3. Equivalent circuit of PV installation for ground current analysis

Normally, numerous PV modules are connected in series on a panel to form a PV array as it is shown in Fig. 3. The circuit model of the PV module [20] is composed of an ideal current source, a diode connected in parallel with the current source and a series resistor. The output current of each PV module is determined as follows:

$$I = I_{sc} - I_d = I_{sc} - I_o \cdot \left[\exp\left(\frac{V + I \cdot R_s}{n \cdot V_T}\right)\right] \quad (2)$$

where $I_o$ is the diode saturation current, $V$ the terminal voltage of a module, $n$ the ideal constant of diode, $V_T$ is the thermal potential of a module and it is given by $m(kT/q)$, where $k$ the Boltzmann's constant (1.38E−23 [J/K]), $T$ the cell temperature [K]; $q$ the coulomb constant (1.6E−19 [C]) and $m$ the number of cells in series in a module. $I_{sc}$ is the short circuit current of a module under a given solar irradiance. $I_d$ is the diode current, which can be given by the classical diode current expression. The series resistance $R_s$ represents the intrinsic resistance to the current flow.

The capacitive coupling proposed of PV modules with ground is modeled as a parallel resistance $R_{pv}$ and capacitor $C_{pv}$ arrangement which simulates the frequency dependency of the insulator between PV modules and the grounding system. The PV structure is connected to the grounding systems represented by the grounding resistance $R_g$ of the installation.

Taking into account that the converter represents a current source for both dc circuit and ac circuit of the PV installation, an equivalent circuit is deduced to analyze the capacitive coupling effect over the current and voltage waveforms, as seen at inverters terminals. In Fig. 4, the equivalent circuit of both dc circuit of the PV installation and ac circuit for connection to the grid as seen at terminals of the inverters and ground is illustrated. In the ac circuit $R_{ac\_cable}$, $L_{ac\_cable}$ and $C_{ac\_cable}$ are the resistance, inductance and capacitance of the distribution line through the power grid, $R_{g\_es}$ is the ground resistance at substation and $L_{filter}$ and $C_{filter}$ are the parameters of the LC filter connected at ac terminals of the converter.

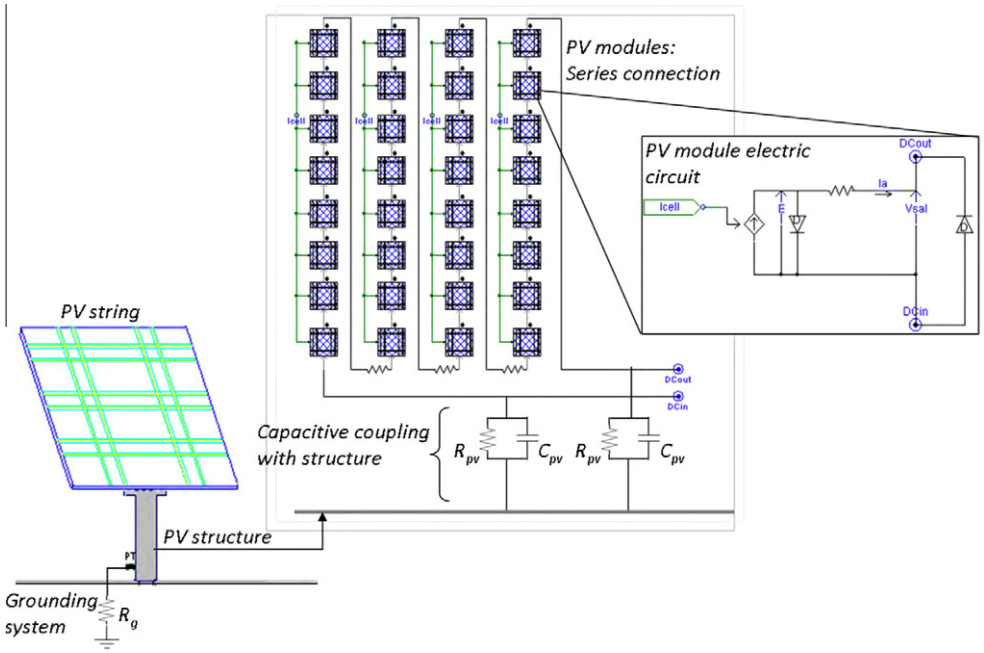


**Fig. 3.** Model of PV module, PV array and capacitive coupling with PV structure.

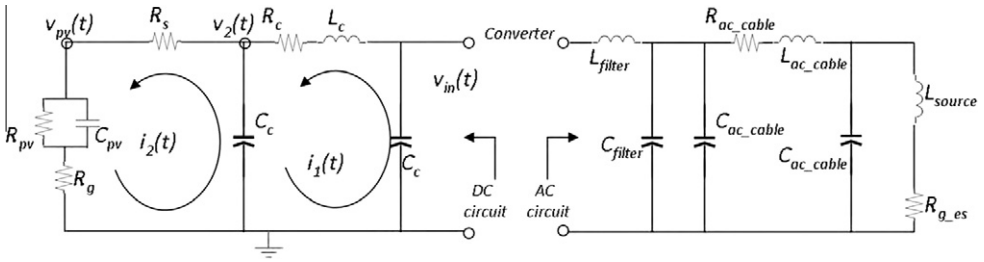


**Fig. 4.** Proposed model for the dc and ac electric circuit of a PV installation.

## 4. Improvement of the equivalent electric circuit of PV installation

The inclusion of $R_{pv}$ and $C_{pv}$ on the PV equivalent circuit allows representing the leakage path for high frequency components between PV modules and ground. The proposed DC equivalent circuit, as seen at converters terminals and at nominal operating condition of the installation, is represented by the following continuous-time equations

$$\frac{di_1(t)}{dt} = \frac{1}{L_c}\cdot v_{in}(t) - \frac{R_c}{L_c}\cdot i_1(t) - \frac{1}{L_c}\cdot v_2(t) \tag{3}$$

$$\frac{di_2(t)}{dt} = \frac{1}{C_c\cdot(R_s+R_g)}\cdot i_1(t) - \left[\frac{1}{C_c\cdot(R_s+R_g)} + \frac{\psi}{C_{pv}\cdot R_{pv}}\right]\cdot i_2(t) + \frac{1}{C_{pv}\cdot R_{pv}\cdot(R_s+R_g)}\cdot v_2(t) \tag{4}$$

$$\frac{dv_2(t)}{dt} = \frac{1}{C_c}\cdot i_1(t) - \frac{1}{C_c}\cdot i_2(t) \tag{5}$$

$$\frac{dv_{pv}(t)}{dt} = \frac{R_g}{C_c\cdot(R_s+R_g)}\cdot i_1(t) + \left(\frac{R_{pv}+R_g}{C_{pv}\cdot R_{pv}} - \frac{R_g}{C_c\cdot(R_s+R_g)} - \frac{R_g\cdot\psi}{C_{pv}\cdot R_{pv}}\right)\cdot i_2(t) + \frac{R_g}{C_{pv}\cdot R_{pv}\cdot(R_s+R_g)}\cdot v_2(t) - \frac{1}{C_{pv}\cdot R_{pv}}\cdot v_{pv}(t) \tag{6}$$

where $i_1(t)$ and $i_2(t)$ are the current of *mesh 1* and *mesh 2*, respectively, of the equivalent DC circuit shown at Fig. 4, $v_{in}(t)$ is the injected voltage by the converter, $v_2(t)$ the voltage at node 2 and $v_{pv}(t)$ is the voltage between PV module and ground and represents the parameter under study. Parameter $C_c$ represents the capacitive coupling between cables and ground and $R_c$ and $L_c$ are the resistance and inductance of the cable, respectively. Defining the following variables states, $\bar{x}_{pro}(t) = \begin{pmatrix} x_1(t)\\ x_2(t)\\ x_3(t)\\ x_4(t)\end{pmatrix} = \begin{pmatrix} i_1(t)\\ i_2(t)\\ v_2(t)\\ v_{pv}(t)\end{pmatrix}$ a state-space model of the dc circuit is represented as follows:

$$\frac{d\bar{x}_{pro}(t)}{dt} = \begin{bmatrix} \frac{-R_c}{L_c} & 0 & \frac{-1}{L_c} & 0\\ \frac{1}{C_c\cdot(R_s+R_g)} & -\left(\frac{1}{C_s\cdot(R_s+R_g)} + \frac{\psi}{C_{pv}\cdot R_{pv}}\right) & \frac{1}{C_{pv}\cdot R_{pv}\cdot(R_s+R_g)} & 0\\ \frac{1}{C_c} & \frac{-1}{C_c} & 0 & 0\\ \frac{R_g}{C_c\cdot(R_s+R_g)} & \varphi & \frac{R_g}{C_{pv}\cdot R_{pv}\cdot(R_s+R_g)} & -\frac{1}{C_{pv}\cdot R_{pv}}\end{bmatrix}\cdot\begin{bmatrix} x_1(t)\\ x_2(t)\\ x_3(t)\\ x_4(t)\end{bmatrix} + \begin{bmatrix}\frac{1}{L_c}\\ 0\\ 0\\ 0\end{bmatrix}\cdot v_{in}(t) \tag{7}$$

$$y_{pro}(t) = [0\quad 0\quad 0\quad 1]\cdot\begin{bmatrix} x_1(t)\\ x_2(t)\\ x_3(t)\\ x_4(t)\end{bmatrix} + [0]\cdot v_{in}(t)$$

being $y_{pro}(t)$ the output signal of the parameter under study of the proposed state-space model and $\psi$ and $\varphi$ are given by the following expressions, respectively;

$$\psi = \frac{R_s + R_{pv} + R_g}{R_s + R_g} \tag{8}$$

$$\varphi = \frac{R_{pv}+R_g}{C_{pv}\cdot R_{pv}} - \frac{R_g}{C_c\cdot(R_s+R_g)} - \frac{\psi\cdot R_g}{C_{pv}\cdot R_{pv}} \tag{9}$$

In the simplified model of PV installation defined at literature [13–15], the capacitance $C_{pv}$ and resistance $R_{pv}$ are considered as infinite and zero, respectively. Then, the capacitive coupling with the grounding system is totally neglected. Even ground resistance of the PV installation is not considered ($R_g = 0$).

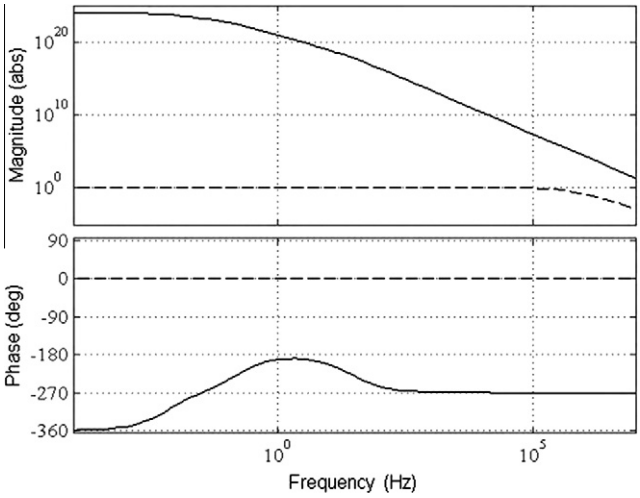


**Fig. 5.** Bode diagram for both proposed model (solid line) and simplified model (dashed line) for the dc circuit of a PV installation.

**Table 1**
Operation parameters used for simulation of the proposed model.

| Parameter | Value |
|---|---|
| $R_c$ | 0.25 (Ω/km) |
| $L_c$ | 0.00015 (H/km) |
| $R_s$ | 0.30 (Ω) |
| $R_{pv}$ | 1.0E7 (Ω) |
| $C_{pv}$ | 1.0E−9 (F) |
| $C_c$ | 1.0E−4 (F/km) |
| $R_g$ | 1.2 (Ω) |

The frequency response of both proposed and simplified model for the dc circuit of a PV installation operating at nominal operating condition are shown in the Bode diagram of Fig. 5. The proposed model presents a considerable gain for waveforms under $10^8$ Hz in comparison with the simplified model which has a limited gain for this range of frequencies. Then, the proposed model is able to show accurately the leakage loop between PV module and grounding system for high frequencies unlike the simplified model. The parameters under study and used for simulations are determined according to the measurement performed on a 1 MW PV installation and are shown in Table 1.

## 5. Power system simulation

### 5.1. Power system modeled

The PV installation to be modeled consists of two circuit with 92 PV arrays and 500 kW each one and are connected in parallel to generate a total of 1 MW. Each circuit is modeled with an equivalent PV array that represents 90 PV arrays and two individuals PV arrays, as shown in Fig. 6. The two circuits have been modeled to analyze the mutual effect arised from the capacitive couplings between both circuits and the grounding system, at nominal operating conditions. Each PV array has 32 modules connected in series and a nominal voltage of 700 V. The parameters of these PV modules are shown in Table 2. The simulation has been performed using PSCAD/EMTDC [21] with a sampling time of at least 50 kHz.

In each circuit of 500 kW, the PV arrays are connected to a DC system of 700 V and the power is delivered to an inverter stage which consists of four inverters of 125 kW in full bridge topology and operation frequency of 3.70 kHz. The ac side of the inverters

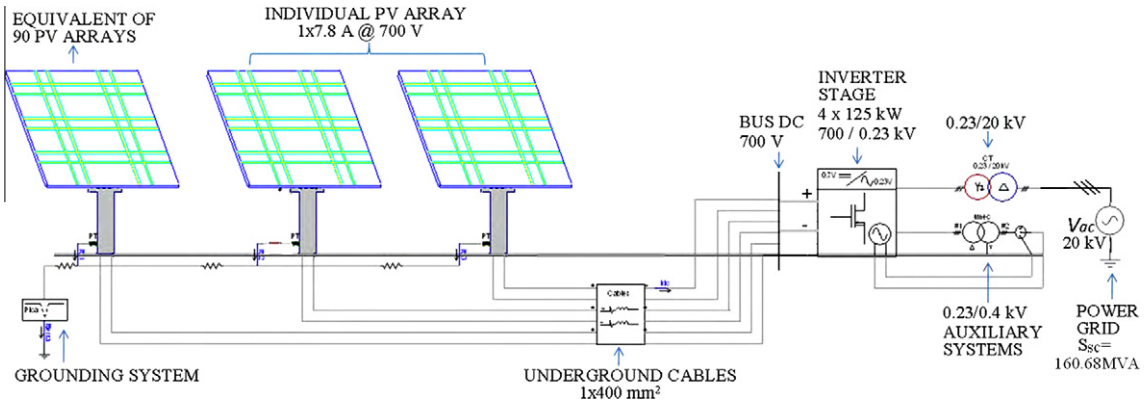


**Fig. 6.** Power system of 500 kW modeled according to the real operating parameters of the 1 MW PV installation.

**Table 2**
PV module parameters at STC (1000 W/m$^2$, 25 °C, AM 1.5).

| Parameter | Value |
|---|---|
| Power output | 170.625 W |
| Power output tolerances | ±3% |
| Module efficiency | 13.9% |
| Current at $P_{max}$, $I_{mpp}$ | 7.8 A |
| Voltage at $P_{max}$, $V_{mpp}$ | 21.875 V |
| Open circuit voltage, $V_{oc}$ | 35 V |
| Short circuit current, $I_{sc}$ | 8.614 A |
| Nominal Operating Cell Temperature (NOCT) | 46 ± 2 °C |
| Temperature coefficient $\beta$ of $I_{sc}$ | +0.0006 1/K |
| Temperature coefficient $\alpha$ of $V_{oc}$ | −0.0037 1/K |
| Temperature coefficient $\gamma$ of $P_{mpp}$ | −0.0045 1/K |

are connected to a power transformer of 700/230 V. The connection to the power grid is done by a power transformer of 0.23/20 kV of 1500 kVA connected in wye-delta. The auxiliary services are simulated with a power transformer of 0.23/0.4 kV which fed a load of 150 kVA. The equivalent impedance of the installation cable is the following:

$$Z_{cable} = 0.6941 + j0.0031\ \Omega$$

The power grid is represented by the following Thévenin equivalent:

Short circuit power $S_{sc}$ = 160.68 MVA

$$Z_{th1} = 2.4894\ \Omega\ \angle 76.01^\circ$$
$$U_{th1} = 20\ \text{kV}\ \angle 80^\circ$$

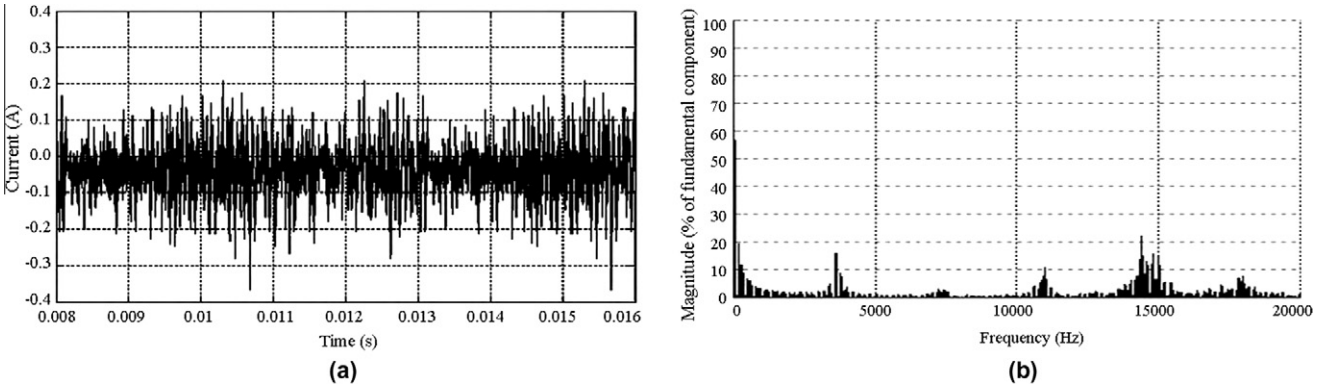


**Fig. 7.** Current measurement at PV array, (a) current waveform measured and (b) FFT analysis of the current waveform.

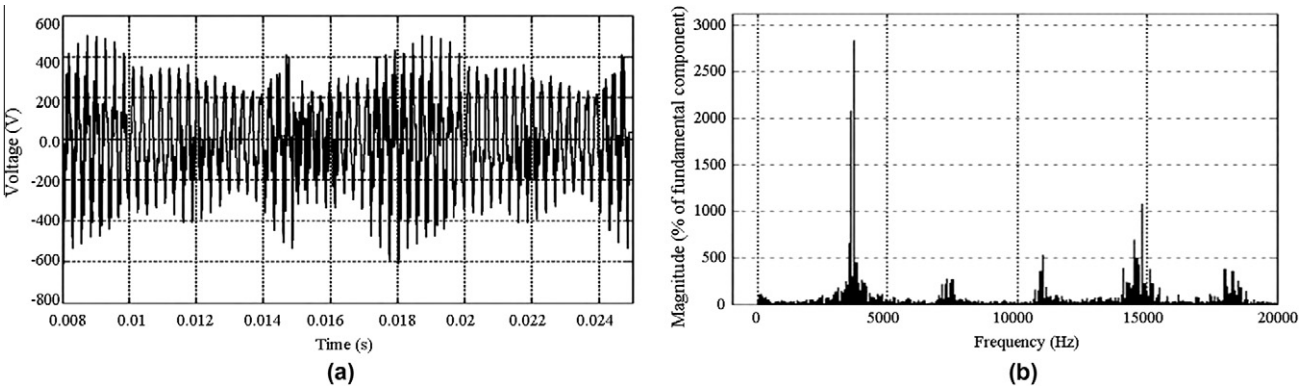


**Fig. 8.** Voltage measurement at PV array, (a) voltage waveform measured and (b) FFT analysis of the voltage waveform.

where $Z_{th1}$ and $U_{th1}$ make reference to the positive sequence Thévenin equivalent.

### 5.2. Field measurement

The current and voltage waveforms measured between the PV module and the grounding system are shown in Figs. 7 and 8, respectively, together with the Fast Fourier Transform (FFT) analysis of each waveform. These measurements were performed at nominal operating condition of the PV installation where more severe is the ground current.

The current registered has a dc fundamental component of magnitude 69.5011 mA and an ac component with a THDI of 31.35% dc fundamental component where the most considerable r.m.s. magnitudes are detected at 3.70 kHz, 11.10 kHz and 14.80 kHz with 11.8212 mA, 6.9550 mA and 15.2973 mA, respectively.

Otherwise, the voltage waveform is mainly compound by an ac component. The FFT analysis performed for this waveform is based on a fundamental frequency of 50 Hz. The result obtained shows a total voltage harmonic distortion (THDV) of 4287.04% where the r.m.s. magnitude of the fundamental component at 50 Hz is

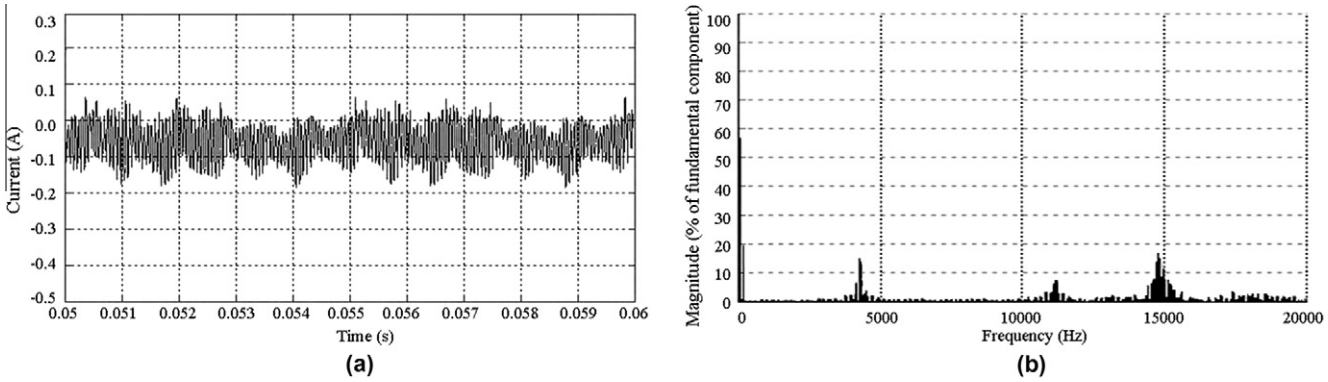


**Fig. 9.** Simulation result of the proposed modeled, (a) current waveform between PV array and grounding system and (b) FFT analysis of the current waveform obtained.

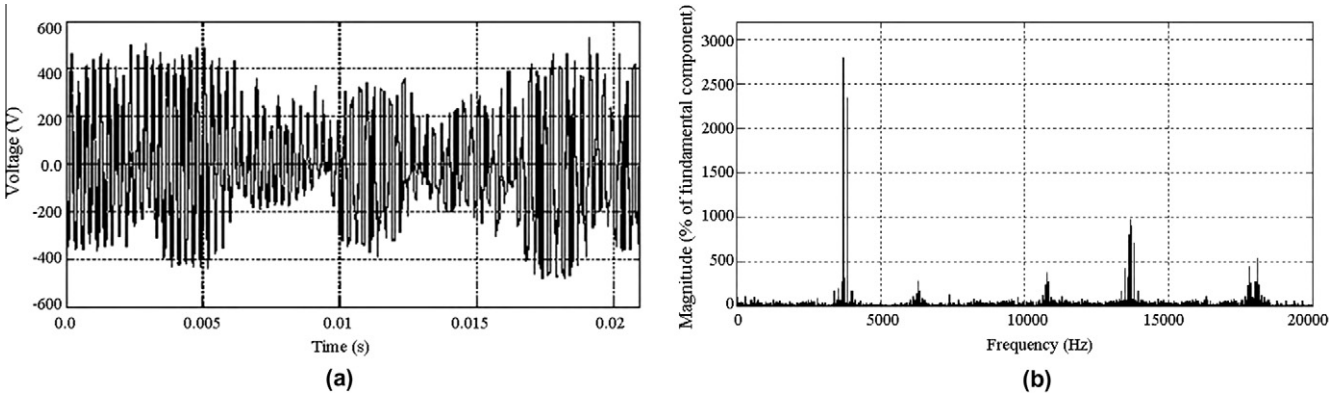


**Fig. 10.** Simulation result of the proposed modeled, (a) voltage waveform between PV array and grounding system and (b) FFT analysis of the voltage waveform obtained.

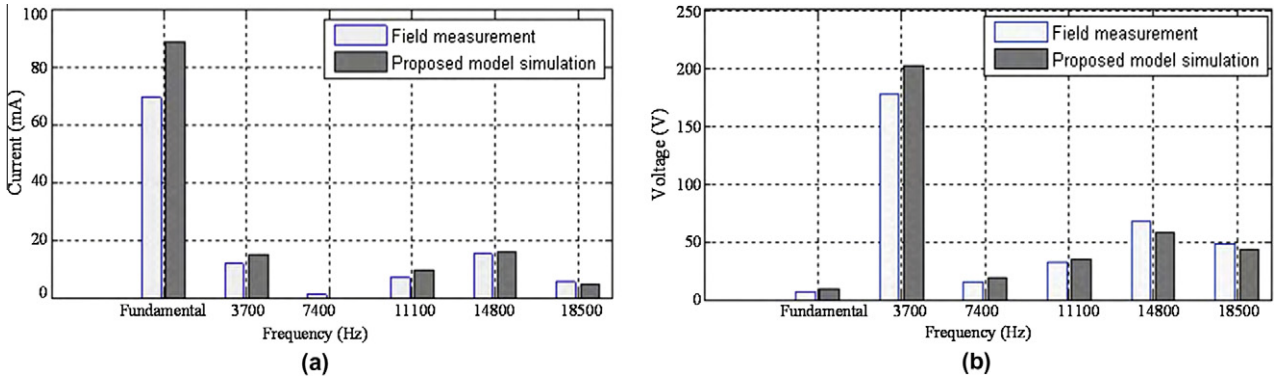


**Fig. 11.** Comparison of the harmonic magnitudes between the field measurements and the proposed model simulation results for (a) current waveform and (b) voltage waveform.

6.4110 V and the most considerable magnitudes appear at 3.70 kHz with 177.5847 V, 7.40 kHz with 15.707 V, 11.10 kHz with 32.055 V, 14.80 kHz with 67.3155 V and 18.50 kHz with 48.0825 V. It is useful to notice that the most important magnitudes of current and voltage appear at frequencies that are multiple of the operation frequency of the inverter (3.70 kHz).

### 5.3. Simulations results of the power system modeled

The electrical parameters of the capacitive coupling between PV array and grounding system have been adjusted according to the field measurement in order to simulate, accurately, the response of the proposed model against the harmonics injected by the operation of the converters. The current and voltage waveforms obtained from the proposed model together with the FFT analysis are shown at Figs. 9 and 10 respectively.

The THDI and THDV obtained from simulations are 26.99% and 3725.17%, respectively, where the DC fundamental component of current is 88.56 mA and the fundamental voltage component at 50 Hz is 8.59 V. The frequencies where most considerable harmonic magnitudes appear are the same of those obtained at field measurement; 3.70 kHz, 11.10 kHz, 14.80 kHz and 18.50 kHz within a percentage error of ±27.42% for fundamental component and ±15.35% for the rest of harmonic components. In Fig. 11, the harmonic magnitudes for current and voltage waveform obtained from simulations were compared with those obtained from field measurements.

## 6. Advantage of the proposed model for designing large-scale PV installations

The proposed model considering capacitive coupling between PV modules and grounding system of the installation leads to an accurate approximation to the response of the PV installation against the frequency spectrum imposed by the switching action of the converters at PV installations. This approximation is not feasible using simplified models because of the bandwidth limitation shown at Fig. 5 for high frequencies.

Both field measurements and simulation results indicate that ground current in large-scale PV installations can be considerable according to the values expressed in [19]. In the 9–25 mA range, currents may be painful at 50–60 Hz, but at 3–10 kHz are negligible [22]. Thus, the proposed model allows the detection of capacitive discharge currents that exceeds the threshold of safety values for work.

Because large scale installations are systems with long cables, the resonant frequency becomes an important factor to consider when designing the ac filters and converters operation frequency.

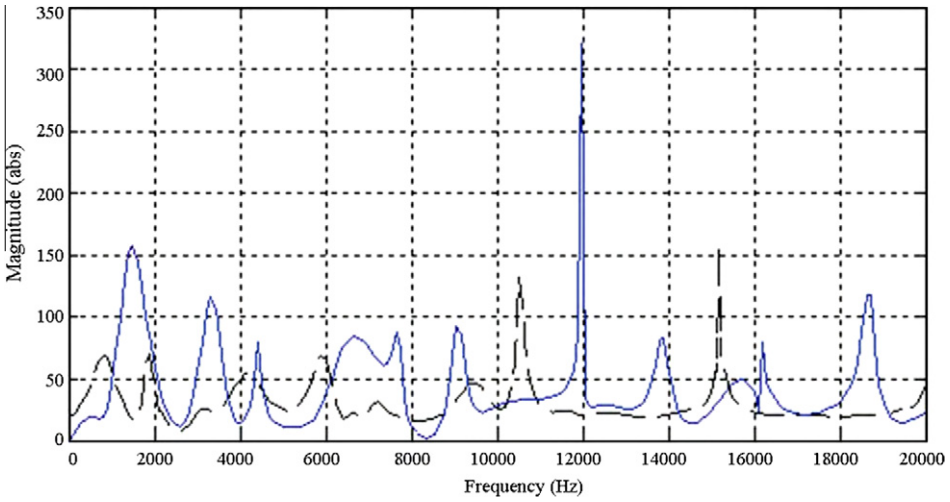


**Fig. 12.** Resonance frequency of the PV installation without capacitive coupling (dashed line) and considering capacitive couplings as in the proposed model (solid line).

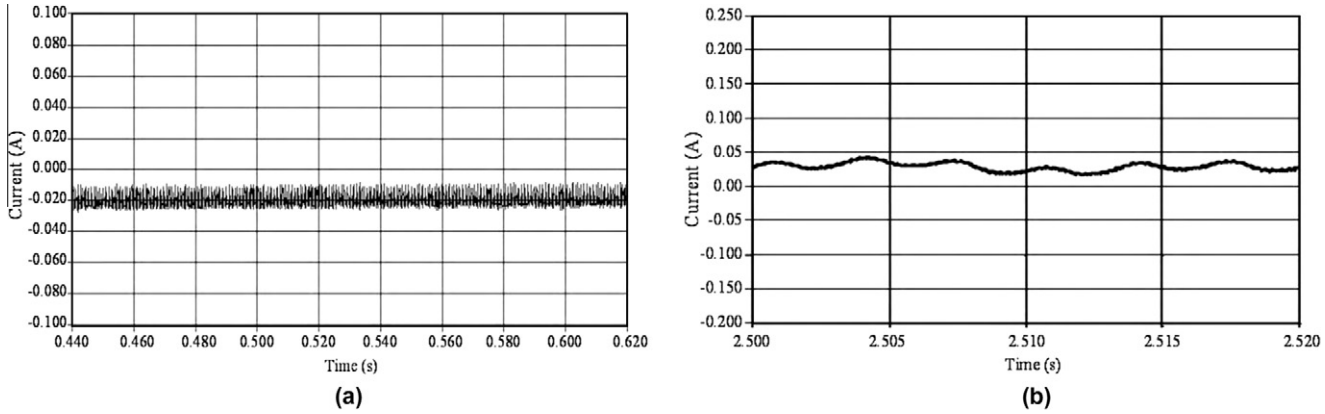


**Fig. 13.** Solution based on the proposed model to minimize the capacitive ground current in PV installation by (a) connecting an inductor between PV array and ground and (b) insertion of capacitors between dc terminals and ground.

The proposed model detects accurately the expected resonant frequency of the PV installations at 12.00 kHz with an impedance magnitude $Z_{res}$ of 323.33 Ω, while simplified models determine a less severe resonant at a frequency value of 15.50 kHz with an $Z_{res}$ of 150.45 Ω, as shown in Fig. 12. This latter resonant frequency is misleading and pointless for the real operating parameters of the installation. The total DC/AC conversion losses obtained from simulations is 5.6% when operating at nominal power, which is equivalent to 56.00 kW. Through the proposed model it has been detected that a 22.32% of the losses due to the DC/AC conversion is because of the capacitive coupling modeled. Thus, a 1 MW PV installation as modeled in Fig. 6 presents 12.50 kW of losses due to the capacitive couplings or leakage loop between PV modules and ground.

According to the PV installation under study, a high ground current has been detected. Then, some preventive actions can be applied to solve this problem such as:

- Connection of the PV array to the grounding systems by means of an inductor. The latter element represents a high impedance for harmonics current and subsequently reduces the capacitive ground current in the installation, as shown in Fig. 13a.
- Insertion of capacitors between the dc terminals and ground avoids the injection of harmonic current to the PV array, as shown in Fig. 13b, hence, the noise level and GPR between PV modules and ground is minimized.
- Adjustment of the firing pulses frequencies and controls strategies to reduce or avoid resonance and capacitive currents by analyzing the ground current with the proposed model.

## 7. Conclusions

The proposed model considering capacitive coupling between the PV modules and the grounding system of the installation leads to an accurate approximation of the real response of PV installation against the high frequency switching action performed by the converters. This approximation is not feasible using the simplified model because of its bandwidth limitation for high frequency waveforms.

Simulations performed with the proposed model allow meeting typical power quality regulations concerning to the harmonic distortion, power losses and noise level, and to optimize the design by increasing the efficiency of the PV installation.

## References

[1] Mahmoud MM. Transient analysis of a PV power generator charging a capacitor for measurement of the *I–V* characteristics. Renew Energy 2006;31(13):2198–206.
[2] Kim J-Y, Jeon G-Y, Hong W-H. The performance and economical analysis of grid-connected photovoltaic systems in Daegu, Korea. Appl Energy 2009;86(2):265–72.
[3] Zhou W, Lou C, Li Z, Lu L, Yang H. Current status of research on optimum sizing of stand-alone hybrid solar-wind power generation systems. Appl Energy 2010;87(2):380–9.
[4] Bakos G. Distributed power generation: a case study of small scale PV power plant in Greece. Appl Energy 2009;86(9):1757–66.
[5] Chicco G, Schlabbach J, Spertino F. Experimental assessment of the waveform distortion in grid-connected photovoltaic installations. Solar Energy 2009;83(1):1026–39.
[6] Lopez O, Teodorescu R, Freijedo F, Doval-Gandoy J. Eliminating ground current in a transformerless photovoltaic application. In: Power engineering society general meeting; 2007. p. 1–5.
[7] IEC 61000-3-6: harmonic emission limits for customers connected to MV and EHV. The International Electrotechnical Commission; 2002.
[8] Std 519-1992: IEEE recommended practices and requirements for harmonic control in electrical power systems. IEEE Power Engineering Society; 1992.
[9] Ahmad GE, Hussein H, El-Ghetany HH. Theoretical analysis and experimental verification of PV modules. Renew Energy 2003;28(13):2198–206.
[10] Park M, Yu I. A novel real-time simulation technique of photovoltaic generation systems using RTDS. IEEE Trans Energy Convers 2004;19(1):299–306.
[11] Djarallah M, Azoui B. Grid connected interactive photovoltaic power flow analysis: a technique for system operation comprehension and sizing. In: Proceedings of the 41st international universities power engineering conference, UPEC '06 1; 2006. p. 69–73.
[12] Chayawatto N, Kirtikara K, Monyakul V, Jivacate, Chenvidhya D. DCAC switching converter modelings of a PV grid-connected system under islanding phenomena. Renew Energy 2009;34(12):2536–44.
[13] Kim S-K, Jeon J-H, Cho C-H, Kim E-S, Ahn J-B. Modeling and simulation of a grid-connected PV generation system for electromagnetic transient analysis. Solar Energy 2009;83:664–78.
[14] Bellini A, Bifaretti S, Iacovone V, Cornaro C. Simplified model of a photovoltaic module. Appl Electron AE 2009;2009:47–51.
[15] Villalva M, Gazoli J, Filho E. Comprehensive approach to modeling and simulation of photovoltaic arrays. IEEE Trans Power Electron 2009;24(5):1198–208.
[16] Iliceto A, Vigotti R. The largest PV installation in Europe: perspectives of multimegawatt PV. Renew Energy 1998;15(1–4):48–53.
[17] IEEE Std. 367-1987: IEEE recommended practice for determining the electric power station ground potential rise and induced voltage from a power fault. IEEE Power Engineering Society; 1987.
[18] Sukamongkol SCY, Ongsakul W. A simulation model for predicting the performance of a solar photovoltaic system with alternating current loads. Renew Energy 2002;27:237–58.
[19] IEEE Std. 80-2000: IEEE guide for safety in AC substation grounding. IEEE Power Engineering Society; 2000.
[20] Joyce A, Rodrigues C, Manso R. Modelling a PV system. Renew Energy 2001;22(1–3):545–8.
[21] Manitoba and HVDC and Research and Centre, PSCAD v4.2; 2006.
[22] IEC 60479-2: effect of current passing through human body. Part II: special aspects. The International Electrotechnical Commission; 1987.

**Miguel García-Gracia** was born in Saint-Brieuc, France on April 23, 1963. He received his B.S. (1986), M.Sc. (1989), and Ph.D. (1996) degrees from the University of Zaragoza. He is presently Lecturer of Electrical Engineering and Area Director of Electric Power System at Circe. His main research interests are in the field of power system, power system protection, electrical energy system, renewable energy integration, lightning protections and dielectrics.

**N. El Halabi** was born in Anaco, Venezuela, in 1985. He received the Electrical Engineering degree in 2006 from Universidad Simón Bolívar, Venezuela. He is currently performing the Ph.D. in Renewable Energy at Universidad de Zaragoza, Spain. His research interests are Power system protection, integration and planning of hybrid power systems.

**H.M. Khodr** received the Ph.D., M.Sc., and Engineer degrees in electrical engineering from the Jos Antonio Echeverra Higher Polytechnic Institute (ISPJAE), Havana, Cuba, in 1997 and 1993, respectively. He is a former Associate Professor of electrical engineering at Universidad Simón Bolívar, Caracas, Venezuela. He was a Researcher at INESC Porto, Porto, Portugal. Presently, he is a Researcher at GECAD, Porto. He has participated in a number of projects performed for the local industries. His current research activities are concentrated on planning, operation, and economics of electrical distribution and industrial power systems; electricity market; grounding systems; and optimization.

**Jose Fco Sanz** was born in Tarrasa, Spain, in 1967. He received the B.E. and M.E. degrees in industrial engineering and the Ph.D. degree in electrical engineering from the University of Zaragoza, Zaragoza, Spain, in 1992, 1995, and 2007, respectively. He is currently the Deputy Director of the Electrical Division, Center of Research for Energy Resources and Consumption and a Lecturer with the Department of Electrical Engineering, University of Zaragoza. His research interests are renewable energy integration, power electronic control for renewable energy sources, high-efficiency energy storage systems, and grid connection systems (FACTS and FAPS).